Investigation of oligomerization of amyloid-β and prion protein

Inaugural dissertation

for the attainment of the title of doctor
in the Faculty of Mathematics and Natural Sciences
at the Heinrich-Heine-Universität Düsseldorf

presented by

Thomas Pauly

from Mönchengladbach, Germany

Düsseldorf, September 2022

From the Institut für Physikalische Biologie at the Heinrich-Heine-Universität Düsseldorf

Published by permission of the Faculty of Mathematics and Natural Sciences at Heinrich-Heine-Universität Düsseldorf

Supervisor:

1. Prof. Dr. Dieter Willbold
2. Junior Prof. Dr. Wolfgang Hoyer

Date of the oral examination: 7th of December, 2022

Declaration

I declare under oath that I have compiled this dissertation independently and without any undue assistance by third parties under consideration of the "Fundamental principles for safeguarding good scientific practice at Heinrich-Heine-Universität Düsseldorf". Furthermore, neither this dissertation, nor a similar work, has been submitted to another faculty. I have not made any unsuccessful attempt to obtain a doctorate.

Düsseldorf, December 9, 2022

Thomas Pauly

Acknowledgement

The work presented in this thesis was carried out at the Institut für Physikalische Biologie of the Heinrich-Heine-Universität Düsseldorf and at the Institut für Biologische Informationsprozesse - Strukturbiochemie at the Forschungszentrum Jülich. I received great support from the staff of both institutes, which contributed to the completion of this work.

First of all, I would like to thank Prof. Dr. Dieter Willbold for the opportunity to work on this project and to complete this thesis. I appreciate the opportunity to start at the institute as an undergraduate student and continue all the way to this doctoral study. His ambitious attitude and extensive contribution to improve manuscripts helped me a lot to develop in areas where I was not comfortable.

I have to give credit to Dr. Luitgard Nagel-Steger for an immense amount of skills that I was able to gather during my doctoral studies, but also before that as a bachelor and master student. She had once told me that she preferred people with edges. I feel that we both had to live with the disadvantages of not being too smooth. We discussed many scientific questions and I always felt that I gained new insights afterwards. Besides the scientific part, we were also able to spend many restful moments together.

Junior Prof. Dr. Wolfgang Hoyer is a great support for me in his role as mentor and second supervisor. I appreciate his efforts to arrange many things in the institute according to everyone's wishes.

I would like to thank Dr. Tao Zhang for never stopping to supervise me. I was able to learn a lot during his stay in Germany and continue to do so in online meetings. His support has helped me a lot to work on different parts of this thesis. I would like to thank the rest of the team Nagel-Steger, including Florian Tucholski, Nazanin Fazelnia, Verena Stehl, and Sergiy Gan for their support during the group meetings. At least some of the time, Rebecca Sternke-Hoffmann was also part of our group, and I always like to think back to the time when we shared an office. After the movement, I shared an office with Robin Backer, who has been a great support not only to me but to the whole institute. Outside the office, I remember having a good time with many people, especially Bianca Axinte and Lora Denson, the best beach buddies.

The collaboration with Jesko Kaiser and Prof. Dr. Holger Gohlke was crucial to build a more complete picture of our biophysical studies. I thank them, together with Dr. Lothar Gremer, for their contribution to the work presented in this thesis and for their profound comments during the meetings.

Even though the doctoral studies involved a lot of time at the institute, Lara Nickenig contributed significantly to this work. She has spared no effort in backing me up. The same is true for my family, without whom I would not have gotten to this point.

Actually (or recently?), this thesis rests on a unique team play with Najoua Bolakhrif. Starting from fundamental support in the lab, including introduction to protein expression and purification, to a substantial contribution to this work. Najoua complemented me in many aspects and for that I am grateful.

Know your circle of competence. The size of that circle is not very important; knowing its boundaries, however, is vital.
Warren E. Buffett, 1997

LIST OF PUBLICATIONS AND MANUSCRIPTS

Publications and manuscripts related to this thesis:

Pauly T, Zhang T, Sternke-Hoffmann R, Nagel-Steger L, and Willbold D, *Differentiation of sub-nucleus sized oligomers and nucleation competent assemblies of the Aβ peptide*, Biophysical Journal, under revision 2022

Pauly T, Bolakhrif N, Kaiser J, Gremer L, Nagel-Steger L, Gohlke H, and Willbold D, *Met/Val129 polymorphism of the full-length human prion protein dictates distinct pathways of amyloid formation*, J. Biol. Chem., Published 2022

Publications and manuscripts not included in this thesis:

Sindram J, et al., *Versatile Route toward Hydrophobically Polymer-Grafted Gold Nanoparticles from Aqueous Dispersions*, J. Phys. Chem., Published 2021

Gopalswamy M, et al., *Biophysical and pharmacokinetic characterization of a small-molecule inhibitor of RUNX1/ETO tetramerization with anti-leukemic effects*, Scientific Reports, Published 2022

Sternke-Hoffmann R, et al., *Universal amyloidogenicity of patient-derived immunoglobulin light chains*, BMC Biology, Submitted 2022

Sevenich M, et al., *Direct disassembly of α-syn preformed fibrils into native α-syn monomers by an all-D-peptide*, manuscript in preparation 2022

Macha A, et al., *Gephyrin E-domain dimerization dependent receptor binding*, manuscript in preparation 2022

CONTENTS

LIST OF FIGURES

LIST OF TABLES

LIST OF ABBREVIATIONS

ssNMR	Solid-state magnetic resonance spectroscopy
cryo-EM	cryogenic-electron microscopy
E. coli	*Escherichia coli*
UV	Ultraviolet radiation
AD	Alzheimer's disease
EM	Electron microscopy
AFM	Atomic force microscopy
FTIR	Fourier transform infrared spectroscopy
CD	Circular dichroism
ThT	Thioflavin T
CR	Congo red
t-AD	Typical Alzheimer's disease
r-AD	Rapid Alzheimer's disease
PCA-AD	Posterior cortical atrophy Alzheimer's disease
Aβ	Amyloid-β
APP	Amyloid precursor protein
IDP	Intrinsically disordered protein
PrP	Prion protein
PrP^C	Cellular prion protein
PrP^{Sc}	Scrapie prion protein
huPrP	Human prion protein
ADAM	A disintegrin-and-metalloproteinase
CJD	Creutzfeldt-Jakob disease
ROS	Reactive oxygen species
TSEs	transmissible spongiform encephalopathies
BSE	bovine spongiform encephalopathy
vCJD	Variant Creutzfeldt-Jakob disease
sCJD	Sporadic Creutzfeldt-Jakob disease
DCVJ	4-(dicyanovinyl)-julolidine

SO	SYPRO orange
YOYO	YOYO-1 iodide
LCPs	luminescent conjugated polythiophenes
LCOs	luminescent conjugated oligothiophenes
hFTAA	Hepta-formylthiophene acetic acid
pFTAA	penta-formylthiophene acetic acid
qFTAA	uadro-formylthiophene acetic acid
BTDSB	5,5'-((1E,1'E)-benzo[c][1,2,5]thiadiazole-4,7-diylbis (ethene-2,1-diyl))bis(2-hydroxy benzoicacid)
AUC	Analytical ultracentrifugation
SV	Sedimentation velocity
SE	Sedimentation equilibrium
F_s	Sedimentation force
F_b	Buoyancy force
$\bar{v}$	Partial specific volume
ρ	Density
F_f	Frictional force
u	Sedimentation velocity
f	Friction coefficient
s	Sedimentation coefficient
S	Svedberg
m	Mass
ν	Viscosity
R_S	Stokes radius
D	Diffusion coefficient
k_b	Boltzmann constant
T	Temperature
R	Gas constant
M	Molar mass
AβO	Amyloid-β oligomers
ADDLs	Aβ derived diffusible ligands
LMWOs	Low molecular weight oligomers
HMWOs	High molecular weight oligomers
FDS	Fluorescence detection system
BOLTS	Biological on-line tracer sedimentation

FFI	Fatal familiar insomnia
GdnHCl	Guanidine hydrochloride
MD	Molecular dynamics

SUMMARY

Neurodegenerative diseases like Alzheimer's Disease and prion diseases involve abnormal accumulation of misfolded proteins in the brain, like the Amyloid-β (Aβ) peptide or the prion protein (PrP). These proteins adopt typical cross-β-sheet conformation to assemble into highly ordered amyloid fibrils. Oligomeric intermediates are central to the study of disease-related aggregation mechanisms, so their detailed characterization may offer new therapeutic targets. However, the dynamic nature and overall low concentration of oligomeric intermediates impede their proper characterization.

For the Aβ peptide, three different oligomeric species were identified in the course of amyloid formation using sedimentation velocity analysis. The comparison of three natural variants of the Aβ peptide, Aβ42, Aβ40, and Aβ42 M35^{ox}, allowed to infer different contributions of these oligomers to the mechanism of amyloid formation. Small oligomeric species, with sizes corresponding to trimers to hexamers, were identified with constant sedimentation coefficient in all three Aβ variants throughout the entire aggregation process. Larger oligomeric species represent a heterogeneous population with sizes of approximately 35 to 47 monomeric units per assembly. This group of oligomers increases in weighted average s-value during the lag phase of amyloid formation, indicating an increasing number of monomeric units to approximately 78 to 89 per assembly before amyloid growth was observed. These larger oligomers present high local monomer concentrations, lowering the energetic barrier for the formation of a nucleus capable of forming amyloid. For the three variants of the Aβ peptide, the concentration of larger oligomers inversely correlates with the time required for amyloid formation, indicating an aggregation mechanism at least partially mediated by oligomeric intermediates.

Human PrP has a naturally occurring polymorphism at position 129, which relates to different pathologies and susceptibility to prion diseases. This polymorphism results in two variants, either 129M or 129V. Here, differences in the tendency to form oligomers and corresponding differences in the mechanism of amyloid formation were demonstrated. The 129M variant is more prone to oligomerization and amyloid formation includes multiphasic behavior with interim plateaus. In contrast, the 129V variant is predominantly monomeric and amyloid formation directly proceeds to the final plateau. In contrast to unstructured Aβ, the secondary structure of huPrP must be destabilized to enable conversion into amyloid structure. Therefore, the amyloid

formation of the 129V variant presumably starts from a destabilized monomer, while the 129M variant involves oligomeric intermediates that undergo structural conversion to reach the final amyloid structure. It was concluded that the polymorphism at position 129 dictates distinct pathways of amyloid formation, which is associated with different disease pathologies.

In this work, different mechanisms of amyloid formation were studied, focusing on the role of oligomerization. The successful characterization of distinct oligomeric species of natural Aβ and huPrP variants will improve the understanding of disease-related aggregation mechanisms. Specific oligomeric species were shown to be on-pathway to amyloid formation by revealing their impact on the aggregation pathway. The influence of oligomers on amyloid formation can be linked to differences in disease pathology. The identified oligomers thus provide valuable insights into the aggregation mechanisms underlying the diseases and represent potential targets to interfere with the amyloid formation process.

1

INTRODUCTION

1.1. Amyloid

Misfolding of proteins can lead to aggregate formation of fibrillar structure with stabilized cross-β-sheet conformation of the monomeric subunits, which is called amyloid [1]. Historically, the term ’amyloid’ was introduced with the discovery of deposits exhibiting positive staining with iodine [2]. The term *amylon*, the Greek word for starch, was the origin of the description of the amyloid structure. The chemical nature initially remained unclear until proteins were identified as the source of amyloid fibrils [3]. Amyloid fibrils are composed of small individual subunits that are generally copies of the same protein [4, 5, 6]. Advances in high-resolution structure resolving techniques such as X-ray crystallography [7, 8], solid-state magnetic resonance spectroscopy (ssNMR) [9, 10], and (cryogenic) electron microscopy ((cryo-)EM) [11, 10] contribute significantly to detailed structural insights into amyloid fibrils revealing the typical cross-β sheet structure, as shown in Figure 1.1.

Amyloid structure is widely associated with a pathological state of a protein that impairs its native function [13]. The role of amyloid fibrils in disease-related processes is presented in detail in subsequent chapters. In addition to the importance of amyloid in various human diseases, this stable protein structure has also been identified with specific functional roles. The protein Curlin from *Escherichia coli* (*E. coli*) is known to form amyloid fibrils with an extended β-sheet structure that mediates binding to host proteins and colonization of inert surfaces [14]. The assembly of amyloid structures with a functional role is a highly regulated process that has also been observed in mammalian systems [13]. The ability to transfer structural identity has been observed as a functional role of the human protein Pmel17, which is involved in the polymerization of small reactive molecules into melanin [15]. The formation of melanin is an

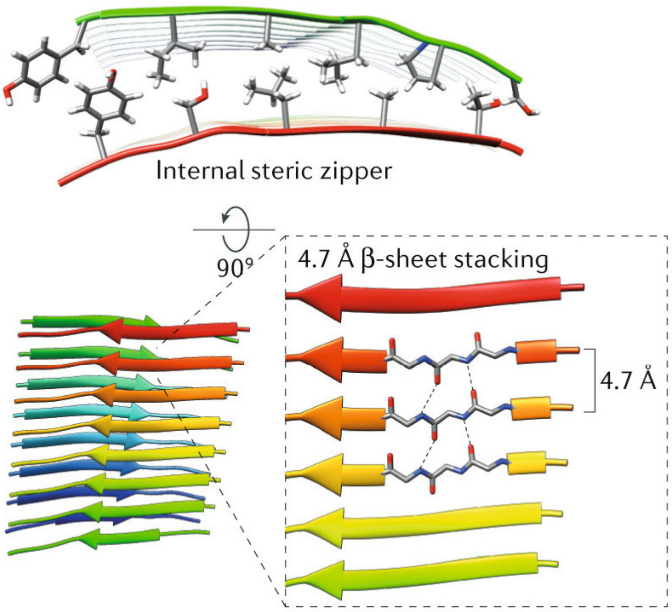

Figure 1.1: Typical cross-β-fold of amyloid fibrils Advances in high-resolution structure techniques have revealed the cross-β-fold typical of amyloid fibrils, as exemplified by transthyretin. Monomeric units in β-sheet conformation stack on each other and are stabilized by hydrogen bonds (black dotted lines) between the polypeptide backbones of the precursors. Peptide backbones are separated by the canonical 4.7-4.8 Å repeat of the cross-β-amyloid fold [12]. The lattice-like face-to-face alignment of the residues further stabilizes the structure as a steric zipper. Adapted from Iadanza et al., 2018 [1].

important process for protection against cytotoxic effects such as oxidative damage or ultraviolet (UV) radiation.

Many human diseases are associated with the formation of extracellular amyloid fibrils or intracellular amyloid-like deposits [13]. The broad spectrum of diseases can be divided into three categories. Neurodegenerative diseases such as Alzheimer's disease (AD), Parkinson's disease, spongiform encephalopathies, and Huntington's disease are associated with amyloid formation in the brain. Non-neuropathic localized diseases such as type II diabetes are characterized by amyloid structures found in specific tissue types other than the brain. In non-neuropathic systemic amyloidosis such as AL and AA amyloidosis, amyloid deposits can be found in multiple tissues. These amyloid-associated diseases may be predominantly sporadic, e.g., Alzheimer's and Parkinson's disease, but may also be hereditary or even transmissible, e.g., spongiform encephalopathies. An environment enriched with preformed amyloid fibrils has been classified as a risk factor for amyloid diseases due to the ability of the amyloid structure to transmit structural information [16, 17].

Amyloid fibrils share features that help identify protein aggregates as amyloid structures [18]. Elongated morphology is commonly studied using electron microscopy (EM) or atomic force microscopy (AFM). Typical diameters of 2 nm to 5 nm are found for individual protofilaments, of which there are usually two to six units in a mature fibril [19]. A high content of β-sheet structure as predominant secondary structural elements is often detected by Fourier transform infrared spectroscopy (FTIR) [20] or circular dichroism (CD) spectroscopy [21]. Another important and regularly exploited ability of amyloid is binding to specific dyes such as thioflavin T (ThT) and Congo red (CR) [13]. Staining of amyloid structure with CR is a commonly used technique not only for *in vitro* studies but also for tissue sections [18, 22]. Binding of CR to amyloid fibrils results in green birefringence under cross-polarized light, but the specificity of this method has been questioned [23, 24]. Although not defined as a criterion for amyloid, binding to ThT is a commonly exploited feature, and the binding mechanism, leading to a strong increase in fluorescence accompanied by a shift of the emission peak wavelength, is well studied [25, 26, 27, 28].

1.2. Alzheimer's disease

Dementia is a global threat to about 50 million people worldwide and this number is expected to increase to about 150 million by 2050 due to the increasing age of population [29]. About two third of people with Dementia have AD. In the United States, AD is the sixth leading cause of death and ranks as high as fifth among people over 64 years of age [30]. The first case of AD was documented in 1906 by Alois Alzheimer, who already reported CR-positive staining of brain tissue [31]. Patients suffer progressive deterioration of cognitive functions, beginning with mild memory loss and behavioral changes [32]. Disease progression is characterized by loss of basic functions such as speech or language comprehension and control over bowel movements. Affected individuals require assistance with personal care and are often institutionalized in nursing homes. The major epidemiologic risk factors for AD are age and genetic predisposition, such that the incidence of AD is about 14 times higher in people aged 85 years or older than in people between 65 to 69 years of age [33]. The increased risk for the elderly population is reflected in a 4.5-fold higher chance of dying from AD when comparing the age group of those above 83 years of age to those between 74 and 84 years of age in the United States [30].

Pathological hallmarks of Alzheimer's disease are extracellular amyloid plaques of the peptide amyloid-β (Aβ) and neurofibrillar tangles of the protein tau [34]. Aβ is involved in triggering synaptic dysfunction leading to neuronal death and the pathological phenomena described above. The amyloid precursor protein (APP) is a membrane protein that is cleaved sequentially by two

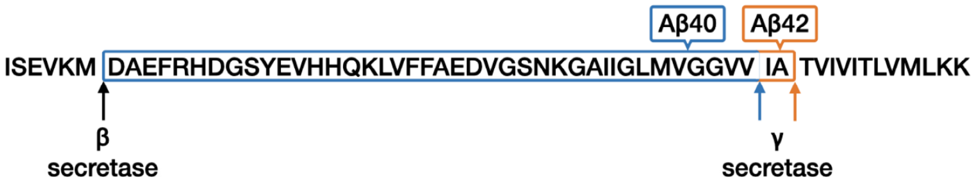

Figure 1.2: Amino acid sequence of APP and cleavage products APP is cleaved by β- and γ-secretase, yielding two variants of the Aβ peptide: Aβ40 or Aβ42 peptide. Adapted from Hamley, 2012 [43].

secretases, β-secretase and γ-secretase (see Figure 1.2). After the first cleavage by β-secretase, a 99 amino acid fragment remains membrane-bound until the second cleavage by γ-secretase releases Aβ peptides of different lengths [35]. The most abundant variant of the Aβ peptide is Aβ40, followed by Aβ42. Aβ42 is more hydrophobic and more prone to form amyloid fibrils than Aβ40, as found in the brains of Alzheimer's patients [36]. There are several other variants of the Aβ peptide, including an oxidized variant of the Aβ42 peptide, converting methionine 35 (M35) to a sulfoxide. M35 is the most easily oxidized amino acid and it was found that amyloid plaques in human brains postmortem include oxidized Aβ peptide [37]. Both, Aβ40 and the oxidized Aβ42 are known to show delayed amyloid formation as well as reduced toxicity [38, 36, 39]. The Aβ peptide is an intrinsically disordered protein (IDPs), which allows for structural plasticity [40, 41]. High-resolution structure methods helped resolve a series of amyloid fibril structures revealing parallel, in register cross-β-sheet conformation [42]. Amyloid fibrils consisting of two protofilaments with an LS-shape of each monomeric unit and a β-sheet conformation stacking on each other perpendicular to the fibril axis were shown for Aβ42 [11].

As with many amyloid diseases, it still remains unclear which species are the most neurotoxic in AD. Studies have shown that toxicity is related to the extracellular deposits composed of amyloid fibrils [44, 45]. In addition to the end products, intermediates of the transition from monomer to amyloid fibrils termed oligomers are also the focus of toxicity studies [46, 44]. These oligomers have been reported to cause direct cellular dysfunction, with size and hydrophobicity, rather than β-sheet structure, being associated with neuronal damage [47, 48]. For oligomers of the Aβ peptide, it has been shown that these intermediates can disrupt membranes [49].

1.3. Prion diseases

Prions were named by Stanley B . Prusiner, who described these pathogens as small proteinaceous infectious particles that are resistant to procedures that modify nucleic acids [50]. Unlike other pathogens, prions lack any nucleic acid and consist of only one component, the prion protein (PrP), which is encoded by the gene *Prnp* [51]. Prion diseases are characterized by the ability of the amyloid structure to catalyze itself and spread between cells or even partially between organisms [52]. It should be noted that the property of transmissibility does not appear to be exclusive to prion diseases, as it has been shown that Aβ exhibits similar properties [53]. Prion pathogenesis involves the conversion of cellular PrP (PrP^C) to the pathogenic scrapie form of PrP (PrP^{Sc}), which forms the actual prion as insoluble, partially protease-resistant aggregates with the ability to recruit additional PrP^C [52]. PrP^C is a glycoprotein bound to the cell membrane *via* a C-terminal glycolipid anchor [54].

The structure of recombinant human PrP (huPrP) expressed in *E. coli* was resolved by solution NMR, identifying an unstructured N-terminal region that spans nearly half of the protein and includes an octameric repeat region (see Figure 1.3) [55]. The unstructured N-terminal region includes residues 23 to 127; note that the first 22 residues function as a signal sequence for protein transport from the endoplasmatic reticulum [56]. The globular C-terminal domain contains three α-helices (residues 144-154, 173-194, and 200-228) and a short anti-parallel β-sheet (residues 128-131 and 161-164) that includes residues upstream and downstream of the first α-helix [55]. In addition, the conformational state of segments within helix 2 and helix 3 was shown to be affected by the length of the flexible N-terminal region, suggesting a transient intramolecular interaction between the unstructured N-terminal and globular C-terminal domains of huPrP. Further, cellular huPrP undergoes posttranslational modifications in mammals leading to two N-glycosylations at asparagine 181 and 197 [57].

After *in vitro* conversion of recombinant $huPrP^C$ to $huPrP^{Sc}$, the structure was recently observed as homogeneous and unbranched amyloid fibrils [58]. The fibril structure included residues 170 to 229 stabilized by an intramolecular disulfide bond between C179 and C214, a hydrophobic core, and a compact fold consisting of six β-strands. The cellular conformation of huPrP undergoes proteolytic processing that leads to various physiological functions and generates biologically active fragments [57]. The α-cleavage roughly separates the globular domain from the unstructured region (cleavage site between H111 and M112) and generates an approximately 18 kDa membrane-bound C-terminal C1 fragment and an approximately 11 kDa N-terminal N1 fragment. The C1 fragment has been found in considerable amounts in normal human brains [59]. The enzymes responsible for the α-cleavage were found in the membrane-bound and

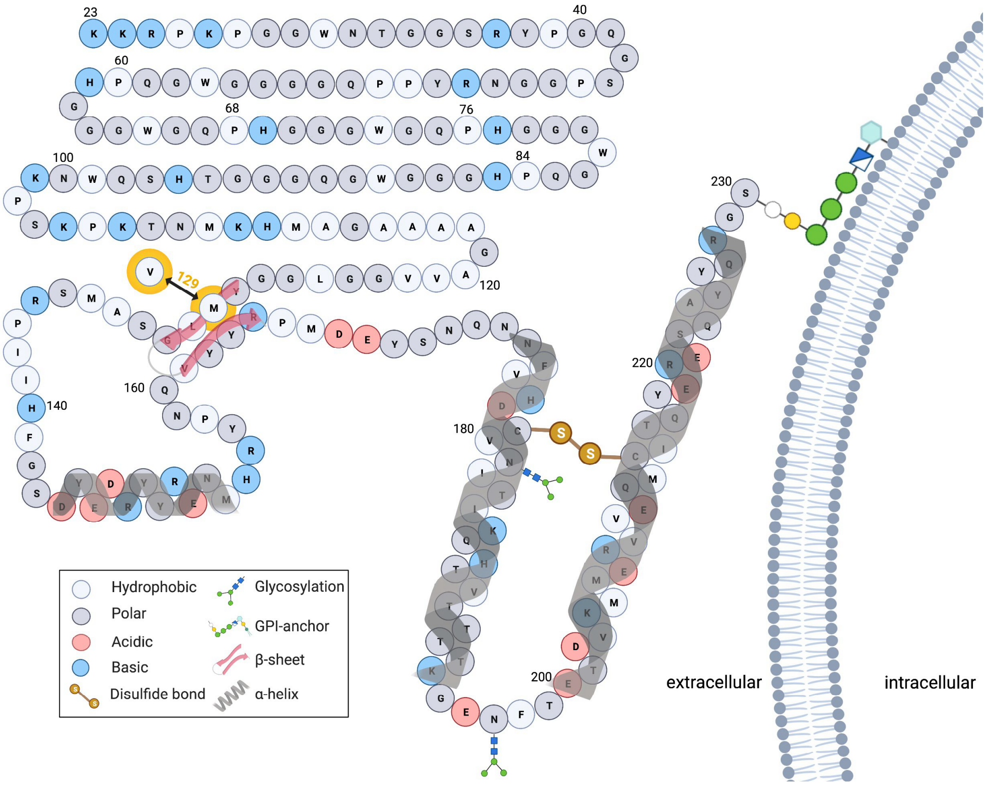

Figure 1.3: Positions of secondary structural elements of full-length huPrP Schematic representation of elements of full-length huPrP(23-230). An unstructured, flexible N-terminal region spans nearly half of the protein (residues 23-127). The globular C-terminal region includes three α-helices (residues 144-154, 173-194, and 200-228) and a short antiparallel β-sheet (residues 128-131 and 161-164). Structural elements taken from Zahn et al., 1999 [55]

zinc-dependent a disintegrin-and-metalloproteinase (ADAM) family, more specifically ADAM10 and ADAM17 [60]. The N1 fragment has been shown to interact with a variety of ligands [61] and interestingly, its production impairs the neurotoxicity of Aβ oligomers [62, 63, 64]. The α-cleavage may have a dual protective function, first by releasing the neuroprotective N1 fragment and second by reducing the amount of full-length PrP^C involved in neurotoxic signaling [65]. Another cleavage occurs at the end of the octarepeat region, termed β-cleavage [57]. The cleavage products are a soluble N2 fragment and a membrane-bound C2 fragment with sizes of about 9 kDa and 20 kDa, respectively. In the brains of patients suffering from Creutzfeldt-Jakob disease (CJD), the C2 fragment was found to be the major cleavage product [59]. The formation of C2 and N2 fragments is governed by cleavage through calpains and Ca^{2+}-regulated cysteine proteases in disease pathogenesis [66] or by reactive oxygen species (ROS) through oxidative stress [67]. However, the cleavage products of β-cleavage have not yet been assigned a physiological function, in contrast to the products of α-cleavage [68, 69].

CJD is one of many human prion diseases, namely transmissible spongiform encephalopathies (TSEs), in which PrP aggregates to form amyloid structures [70]. In addition to CJD, there are other prion diseases in humans such as familial fatal insomnia, Gerstmann-Sträussler-Scheinker disease, and Kuru that differ in terms of disease onset and dependence on mutations or genetic polymorphism [71, 72, 73]. TSEs occur not only in humans but also in various animals, such as chronic wasting disease in deer and elk, scrapie in sheep and goats, and bovine spongiform encephalopathy (BSE) in cattle [74]. BSE has been found to be transmissible to humans, crossing the species barrier and causing variant CJD (vCJD) [52]. The most common prion disease in humans is sporadic CJD (sCJD), the definite cause of which is still unknown [75, 76]. The pathogenesis of sCJD could not be fully explained by infection, but rather a spontaneous conversion of PrP^{C} to PrP^{Sc} is thought to play an important role in the development of the disease.

1.4. Mechanism of amyloid formation

The protein-only hypothesis provides a theoretical model for the mechanism of self-replication by which the prion protein can act as an infectious particle in the absence of nucleic acid [77]. The key element of this hypothesis is the ability of the misfolded state to replicate in a self-catalyzing process by recruiting native monomers. The concept of a misfolded state facilitating its own assembly and growth could be applied to other amyloidogenic proteins. The Aβ peptide proved to be competent in seeding, such that the addition of preformed fibrils leads to immediate polymerization of soluble monomeric units [36].

Amyloid structure shares some common features with protein crystals, in particular, a single monomeric protein conformation in a well-defined intermolecular packing [78]. In contrast to amyloid fibrils, amorphous aggregates, in general, lack a single distinct monomer conformation, so that the formation of these aggregates is usually fast in a supersaturated solution. Protein crystal formation as well as amyloid fibril formation is a time-dependent process in which the formation of a growth competent nucleus constitutes the rate-determining step. Protein polymerization which requires the formation of a seed competent of recruiting monomeric units to form aggregates with well-defined structure can be described by the mechanism of nucleation-dependent polymerization. This mechanism typically describes a sigmoidal curve consisting of three different phases: lag phase, during which nucleation occurs; growth or elongation phase, during which existing seeds recruit monomeric units to extend the fibril mass; final plateau or saturation phase with low and approximately constant monomer concentration (see Figure 1.4) [79]. During the lag phase, primary nucleation occurs, in which the formation of a growth

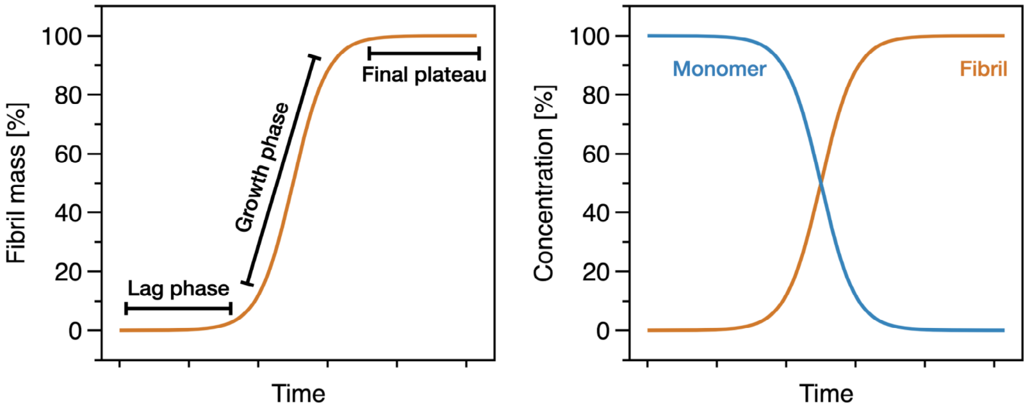

Figure 1.4: Kinetic phases of amyloid formation The characteristic sigmoidal curve for amyloid formation follows the nucleation-dependent polymerization mechanism, which consists of three phases: Lag phase, elongation or growth phase, and final plateau or saturation phase. The soluble monomer is consumed and incorporated into the well-defined packing of amyloid fibrils. Recreated from Arosio et al., 2015 [83].

competent nucleus is the decisive event for the transition into the elongation phase. Nucleus formation involves a number of steps that are thermodynamically unfavorable due to the entropic costs that cannot be prevailed by the intermolecular interactions during association [80]. A nucleus is typically defined as the smallest assembly for which addition of monomer is faster than dissociation back to monomer [81]. The high activation energy of primary nucleation makes it a rare event, even though the formation of a growth competent nucleus constitutes the essential reaction for amyloid fibril formation [42]. A crucial determinant of the duration of the lag phase is the total concentration of monomeric units [78]. The effect of seeding mentioned above can essentially skip the lag phase by introducing growth competent species which lead to immediate elongation and depletion of monomers [82].

Seed growth occurs during the elongation phase, which is characterized by a steep increase in fibril mass because the conversion of native protein to its amyloid conformation is maximal during this phase [83]. The growth of the amyloid structure is thermodynamically favorable, hence monomer is rapidly consumed [78]. The maturation of protofibrils and equilibrium between remaining monomers in solution and amyloid fibrils is reached in the final plateau region or saturation phase [83, 79]. The length and steepness of the transition depends on the interplay of underlying processes [84]. However, all three phases of amyloid formation should not be attributed to single molecular events, but rather to a combination of all described processes

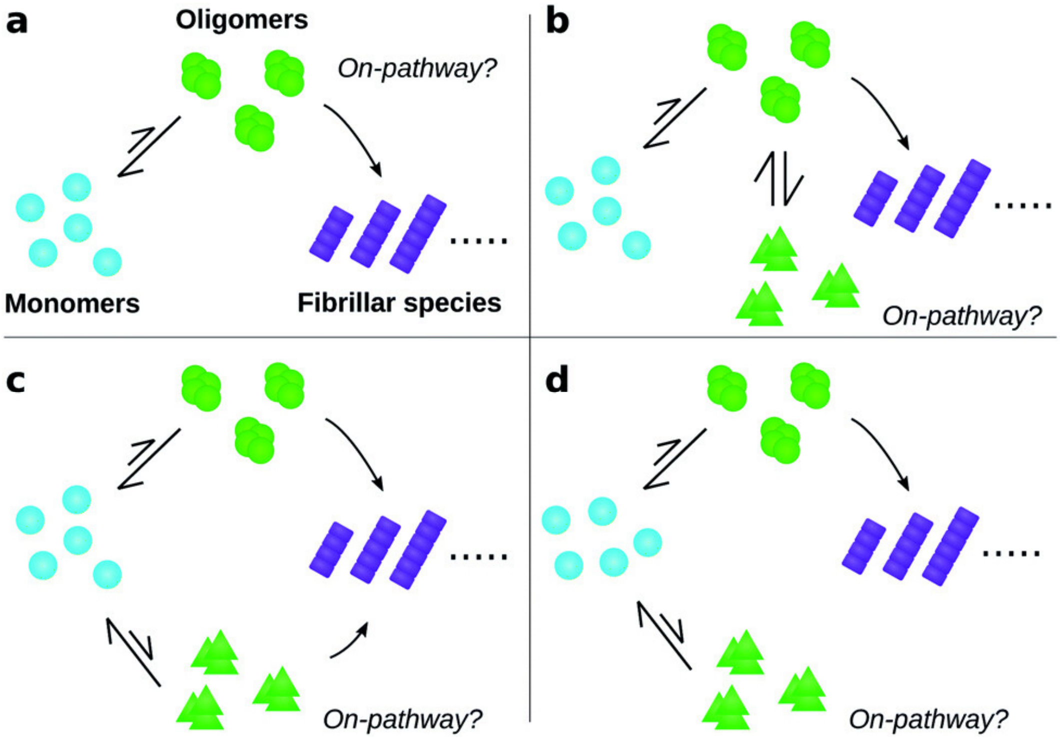

Figure 1.5: Challenges in the classification of oligomers as on- or off-pathway species The classification of oligomers into on- or off-pathway species can be challenging. Uncertainty can arise from several situations: (a) most but not all oligomers dissociate back into monomers instead of growing into amyloid fibrils, even though a small number converts into amyloid fibrils; (b) one oligomeric species converts into amyloid fibrils but also forms another oligomeric species as a side reaction, which does not convert into amyloid fibrils; (c) different oligomeric species are formed by monomers and both convert to amyloid fibrils but at different rates; (d) different oligomeric species are formed by monomers and only one of them converts to amyloid fibrils. Taken from Dear et al., 2020 [85].

with substantial differences in their fluxes and activities of reactive species at specific time points during the aggregation process [83, 42].

The majority of species in solution during amyloid formation at any time are monomers or fibrils [83]. The overall concentration of all intermediates, small oligomers or aggregates, on- or off-pathway to amyloid fibrils, is low. This aspect of intermediates makes their investigation challenging. Kinetic intermediates are oligomers that cover a broad range of assemblies consisting of more than one monomeric unit [81]. Oligomers can be grouped according to various aspects, such as their growth rate, which is generally slower than for amyloid fibrils, their structure, size, or toxicity. The nature, formation, and kinetics of oligomers are of great interest for understanding disease pathogenesis, as they are thought to be primarily responsible for toxicity in various amyloid diseases [86, 87, 88, 89, 90, 91]. Because oligomeric species are central for understanding disease pathogenesis, their contribution to the amyloid formation process is important for revealing the underlying molecular mechanisms [85]. A commonly used classification of oligomeric species is their contribution to the amyloid formation process, with those oligomers that react onward to amyloid fibrils referred to as on-pathway oligomers and those oligomers that result from side reactions referred to as off-pathway oligomers [92, 93, 94]. However, classification as on-pathway or off-pathway species can be difficult with a binary definition, as shown in Figure 1.5. Even if an oligomeric species can convert into amyloid fibrils, which may classify this species as on-pathway, the majority of this species would also dissociate back into monomers, which may classify this species as off-pathway [85]. Oligomer-mediated pathways to amyloid formation often involve the formation of multiple oligomeric species, which may occur as a side reaction of one oligomeric species or from monomers with different potential to convert into amyloid fibrils or again dissociate back into monomer. The on- or off-pathway character of an oligomeric species should not be judged by the proportion of that species that converts into amyloid fibrils, but rather by the proportion of amyloid fibrils which are derived from that oligomeric species. This aspect would classify oligomers as on-pathway if some of them contribute to fibrils formation by converting into a growth-competent nucleus, although their majority dissociates back to monomers as soon as amyloid growth is the favorable process. Therefore, an oligomeric species is on-pathway if it directly converts to amyloid fibrils or contributes to the formation of a species capable of converting to amyloid fibrils.

Such kinetically unstable oligomers were studied for Aβ42 [95] and PrP [96] to elucidate their role in amyloid fibril formation. If an oligomeric species is, first, capable of forming amyloid and, second, in rapid equilibrium with another oligomeric species that is unable to convert into amyloid structure, it is questionable to consider these two species as two distinct species, but rather as one on-pathway population [85]. Moreover, the role of an oligomeric species in amyloid formation may change during the aggregation process and should be evaluated in a time-dependent manner.

Despite the classification of oligomers into on-pathway and off-pathway species, the oligomeric intermediates formed during the lag phase of amyloid fibril formation have heterogeneous conformation [42]. Some of these oligomers already have β-sheet content, but amyloid fibril formation usually still takes considerably long time. From this, it can be seen that oligomers early in the lag phase are not yet competent to form amyloid fibrils despite their β-sheet conformation.

The classical nucleation mechanism for the formation of amyloid fibrils must be extended to include unstable oligomeric intermediates with a slow rate of conversion into amyloid, which results in most, but not all, of them dissociating back into monomers [95]. An aggregation mechanism mediated by oligomers is similar to the two-step nucleation theory, which also holds for the process of crystallization in which nuclei form inside meta-stable clusters [97]. An overview of the species found during the process of amyloid fibril formation leading to conformation-true replication is shown in Figure 1.6. Between oligomer formation and elongation of a nucleus capable of growth, consolidation of intermediates occurs [42]. The process of consolidation is the key step in the oligomer-mediated aggregation mechanism, which is the transition between a mixture of monomers with on- and off-pathway oligomers and the polymerization of monomers starting with a growth-competent nucleus with cross-β-sheet conformation to form amyloid. In a supersaturated solution, the intermediates present an increased local concentration of monomeric units, which lowers the kinetic barrier for monomers to convert into β-sheet conformation [98, 42]. Such a conformational change, leading to the formation of a nucleus capable of growth, could also occur in solution by chance. Once such a nucleus is formed by either pathway, amyloid growth leads to the depletion of monomers. The oligomers, starting with the least stable, are dissolved as a consequence of the equilibrium situation with the monomeric fraction, while the growth-competent nucleus initializes the self-replicating process. Oligomers predominantly dissolve because the conversion of oligomers into amyloid is slow. Hence, the system is dominated by elongation of growth-competent nuclei with cross-β-sheet structure and secondary processes involving amyloid fibrils [95].

Elongation is not the only mechanism that dominates the amyloid growth process. It was found that aggregation kinetics *in vitro* cannot be described by primary nucleation and elongation alone, but that amyloid fibrils contribute to the aggregation process *via* secondary pathways [99]. These pathways include fragmentation and secondary nucleation. The proliferation of amyloid fibrils can only be explained by a positive feedback loop based on the interaction between existing amyloid fibrils and monomers, i.e., secondary nucleation. Secondary nucleation is a monomer-dependent process that catalyzes the nucleation process to form new amyloid structure on the surface of already existing fibrils [100]. This process is dependent on both monomer and amyloid fibril concentration. Another secondary pathway that is independent of the monomer concentration is fragmentation of amyloid fibrils [101]. Both secondary pathways need to be considered to explain the exponential growth of amyloid fibril mass, resulting in conformation-true protein polymerization.

The described aggregation mechanism focused mainly on intrinsically disordered proteins such as Aβ peptide. For globular proteins, at least partial unfolding is required for the conversion into amyloid [102]. Since all amyloid structures share the cross-β-sheet conformation, considerable rearrangement of the protein conformation is required, as globular proteins usually comprise a variety of different secondary structural elements. A reduction in structural constraints supports intermolecular interactions such as hydrogen bonding, electrostatic interactions, and hydrophobic

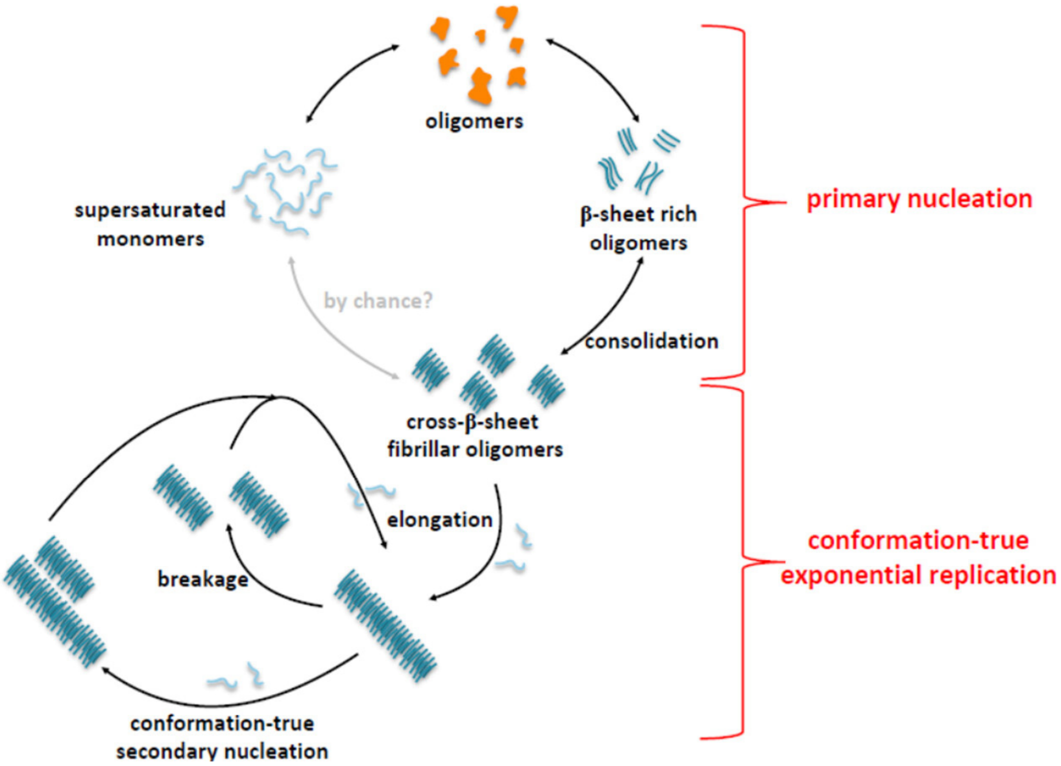

Figure 1.6: Intermediate species during the amyloid formation process Overview of the species involved in amyloid formation. A supersaturated monomer solution rapidly forms oligomers as intermediates of the amyloid formation process. Oligomers are a heterogeneous population of assemblies with different conformations, including β-sheet-rich species. Oligomers with a cross-β-sheet conformation that are able to pass their conformation to monomeric units are nuclei capable of growth, leading to conformation-true fast formation of amyloid fibrils. Oligomers undergo consolidation, which determines the length of the lag phase for an oligomer-mediated two-step nucleation mechanism. Taken from Willbold et al., 2021 [42].

interactions that lead to oligomerization and fibril formation [103]. It has also been suggested that aggregation of globular proteins can occur *via* aggregation of native-like oligomers, retaining much of the native structure before a conformational change occurs leading to the typical amyloid structure [13]. The variety of conformational states that can be adopted by polypeptide chains and the transformation between these states can lead to distinct aggregation pathways on different time scales. Under physiological conditions, the structure of a globular protein represents a mixture with a large majority of well-folded conformations, but also a variety of partially unfolded conformations [104]. Despite the small number of already existing partially unfolded conformations of a protein, *in vivo* reduced protein stability leading to partial unfolding can result from local pH changes at membranes, oxidative or heat stress, and mutations [102]. In particular, mutations associated with an accelerated formation of amyloid fibrils are involved in the destabilization of the native structure and increased concentration of partially unfolded conformers [105, 103]. The increase in the population of non-native states of a protein is the primary mechanism by which naturally occurring mutations of amyloidogenic proteins mediate their pathology [13]. The species that occupy non-native states are promising targets for therapeutics that aim to prevent disease by stabilizing the native conformation of pathologically relevant proteins [106, 107, 108, 109].

1.5. Fluorescent probes for amyloid detection

The distinct structural properties of amyloid are exploited in spectroscopic techniques using molecular probes [79]. Fluorescent dyes provide fundamental insight into the mechanisms of amyloid formation *in vitro* as well as amyloid present in tissues. The usual approach exploits a change in the spectroscopic properties of the molecular probes upon binding to the amyloid structure. The two most commonly used dyes in studies of amyloid are ThT and CR [18]. CR was one of the first dyes used to detect amyloid structure. It exhibits a characteristic red shift of the absorption maximum (490 to 512 nm) that results in green birefringence under polarized light [110]. However, CR is unfavorable for studying the underlying mechanisms of amyloid formation because it is less sensitive than ThT and affects the aggregation mechanism [18]. ThT is a suitable probe, as fluorescence emission is significantly increased at about 482 nm when bound to amyloid structure, along with an additional excitation peak at about 450 nm [27]. ThT and CR bind mainly to hydrophobic grooves on amyloid fibrils aligned along the fibril axis (see Figure 1.7) [111].

The structure of ThT includes a benzylamine and a benzothiazole group that share a single carbon-carbon bond around which free rotation is possible [112]. Excited states occupied after photon excitation are rapidly quenched by this rotation for the free dye. The complex between ThT and the amyloid structure restricts the freedom of rotation of the single carbon-carbon bond, resulting in the retention of the excited state after photon excitation and an increase in fluorescence emission [25]. Binding of ThT is a general feature of amyloid fibrils, regardless of amino acid sequence, suggesting a characteristic property such as cross-β-sheet conformation as a key element for interaction. Interestingly, the binding of ThT to the β-sheet surface of fibrils is in rapid equilibrium with dissociation and is not uniform, but preferential for channels formed by hydrophobic aromatic amino acids [113]. This is particularly surprising since ThT is positively charged and the preferential binding to hydrophobic amino acids on the β-sheet surface of fibrils rather than to negatively charged amino acids suggests that the hydrophobic interaction with the aromatic ring systems of the residues is the superior effect in stabilizing the complex. The

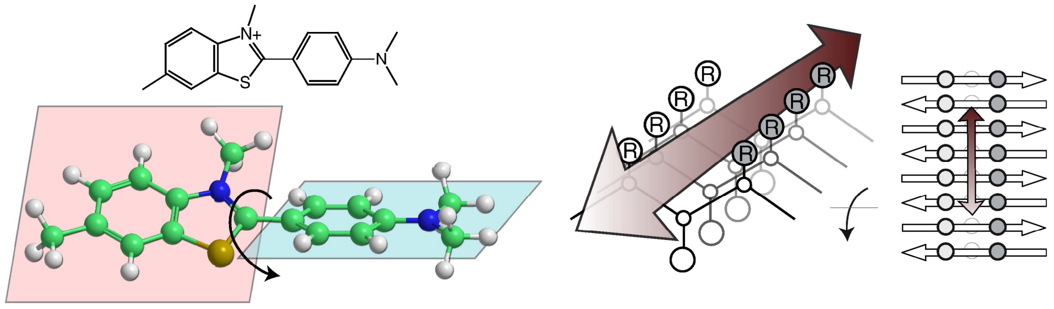

Figure 1.7: ThT binding to amyloid structure The ThT structure is characterized by two planar segments with free rotation about a single carbon-carbon bond. The binding of ThT is thought to occur along the fibril axis, primarily in hydrophobic grooves. Adapted from Biancalana et al., 2010 [25].

presence of a β-sheet structure on the fibril surface is a prerequisite for ThT binding, but amyloid fibrils can vary in length, and therefore the minimum number of monomeric units with β-sheet conformation required for interaction with ThT is an important parameter. At least four β-strands of hydrophobic aromatic amino acids are required to form binding sites for ThT, which also explains the lack of interaction with globular β-sheet-rich proteins, which usually consist of a smaller number of distorted β-sheets [114, 25].

In *in vitro* experiments, ThT fluorescence is a common method to monitor the formation of amyloid fibrils over time and to determine their concentration, since the signal intensity within a certain concentration range correlates linearly with the amyloid concentration [115]. ThT fluorescence intensity is strongly dependent on dye concentration and shows an optimal signal at concentrations between 20 µM and 50 µM. Exceeding the optimal concentration could affect aggregation kinetics depending on the protein under study. The exclusive property of ThT to bind amyloid fibrils has been questioned, and interaction with hydrophobic domains in globular conformations of proteins is a major concern [116]. Besides interaction with non-amyloidogenic proteins, the interaction of ThT with intermediates of the amyloid formation process is of interest. The interaction of ThT with oligomeric species could complicate studies of amyloid fibrils on the one hand, but on the other hand, could allow the study of intermediates, which are potential toxic species. Both ThT and CR are capable of binding oligomers of the synthetic Aβ peptide, as well as oligomers in tissue [117]. The question remains whether the binding of intermediates indicates a common structure with mature fibrils, which may present binding similar sites. Increasing interest in potentially toxic intermediates has led to the development of new molecular probes, as ThT still shows a strong fluorescence increase in the presence of amyloid fibrils and is therefore not a suitable dye for studying oligomeric species in detail [118].

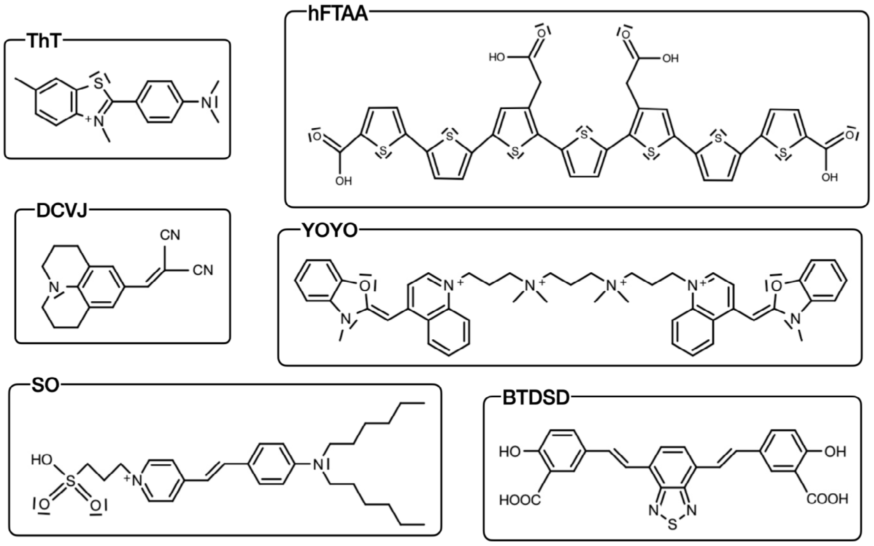

Figure 1.8: Selection of fluorescent dyes for staining amyloid Chemical structure of a selection of dyes with the ability to stain amyloid. ThT as a positively charged dye is most commonly used for amyloid detection [25]. hFTAA as a negatively charged dye belongs to the group of luminescent conjugated thiophenes with spectral properties depending on the number of thiophenes and with the ability to stain both amyloid fibrils and oligomers [121]. DCVJ as a neutral dye is capable of staining both amyloid fibrils and oligomers [119]. YOYO as a positively charged dye, generally used as a DNA stain, monitors amyloid formation [123]. SO is a zwitterionic dye used to stain protein gels but is also suitable for staining amyloid [120]. BTDSB is a negatively charged derivative of CR that binds to amyloid but shows little fluorescence increase [122].

Since the beneficial properties of ThT and CR for amyloid staining were discovered, several attempts have been made to develop new dyes or test existing dyes for improved amyloid or intermediate staining properties. Some of these are 4-(dicyanovinyl)-julolidine (DCVJ) [119], SYPRO Orange (SO) [120], a group of luminescent conjugated thiophenes [121], a group of CR derivatives [122] and YOYO-1 iodide (YOYO) [123] (see Figure 1.8).

DCVJ is a neutrally charged dye that, similar to ThT, has free rotation about a single carbon-carbon bond linking a dicyano group to a julolidine ring system [119]. The restriction of free rotation suppresses the role of the dicyano group as a fluorescence quencher and can be induced by the environment [124]. In a system for amyloid formation of transthyretin, the ability of DCVJ to respond effectively to both fibril structure and smaller assemblies at an early stage of kinetics was demonstrated [119]. In kinetic experiments, DCVJ was shown to reach the plateau of fluorescence signal earlier than ThT, indicating a preferential interaction with oligomers and protofibrils. At higher concentrations, DCVJ exhibits an increased additional emission peak, which may be due to an excimer state involved in binding to certain oligomeric species [125].

SO is a zwitterionic dye primarily used for staining protein gels and western blots [126]. It is known that the binding mechanism between SO and proteins involves the exposure of hydrophobic regions on the protein surface, resulting in increased fluorescence emission upon SO binding [127]. SO has been introduced into amyloid studies, and the binding mode differs from that of ThT and DCVJ. Monitoring of the amyloid formation pathway of amylin revealed no response to intermediate species before amyloid fibrils, similar to ThT signal [120].

The class of luminescent conjugated thiophenes includes a conjugated thiophene backbone of varying lengths whose conformation in the bound state is determined by the protein [121]. Luminescent conjugated thiophenes are divided into two classes that differ by the number of thiophene groups: luminescent conjugated polythiophenes (LCPs) [128, 129, 130] and smaller oligothiophenes (LCOs) [131]. Hepta-formylthiophene acetic acid (hFTAA) belongs to the group of LCOs consisting of seven thiophene groups, resulting in a net charge of $-4\times1.602\times10^{-19}$ C [121]. LCOs have gained interest in the study of intermediate species because a change in the thiophene backbone translates into changes in spectral properties, resulting in sensitivity to small differences in protein structure [132]. The mechanism by which LCOs recognize different species during amyloid formation is based on the conformational constraint of the thiophene backbone [121]. The interaction between LCOs and amyloid fibrils is assumed to share similarities with ThT binding [133]. A minimum number of five thiophene groups is required for LCOs to respond to ThT-negative intermediate species, indicating a strong dependence of the number of thiophene groups on the oligomer probing ability [121]. The pentameric compounds penta-formylthiophene acetic acid (pFTAA) and hFTAA have spectral properties sensitive to the morphology of the interacting aggregate, whereas the tetrameric compounds quadro-formylthiophene acetic acid (qFTAA) can be used to stain mature amyloid fibrils *in vivo* [121].

A group of CR derivatives was developed to optimize the amyloid staining properties of CR for *in vivo* applications [122]. An initial derivative of CR was the less acidic, more lipophilic dye chrysamine-G [134], which provided the starting point for the synthesis of a series of bis-styrylbenes with strong affinity for amyloid detection [122]. The dye 5,5'-((1E,1'E)-benzo[c][1,2,5]thiadiazole-4,7-diylbis(ethene-2,1-diyl))bis(2-hydroxy benzoicacid) (BTDSB) is one of these CR derivatives, consisting of a single central phenyl with an attached benzothiazole group and vinyl groups as linkers to the bounding aromatic rings, resulting in a net charge of $-2\times1.602\times10^{-19}$ C. BTDSB binds to amyloid fibrils of the Aβ42 peptide, but with less fluorescence enhancement than ThT. No response to intermediate species during amyloid formation was detected.

YOYO is a positively charged homodimeric derivative of oxazole yellow that was originally used to stain double-stranded DNA [135]. In addition, YOYO was used to stain amyloid fibrils of the peptide Aβ42 with the oxazole yellow segments arranged parallel to the fibril axis, resulting in a 200-fold increase in fluorescence [123].

1.6. Analytical ultracentrifugation

Analytical ultracentrifugation (AUC) is a technique for real-time monitoring of particle motion in solution [136]. AUC uses an ultracentrifuge with an integrated optical detection system that enables the detection of particle concentration distributions under centrifugal fields [137]. The great advances in AUC were made by Theodor Svedberg in the 1920s. Increasing the rotor speed to 60,000 rpm resulted in centrifugal field strength of up to 300,000 ×g, which allowed the analysis of particles as small as 100 Da. The centrifuge has an evacuated chamber with temperature control, which provides space for the rotor to spin and suppresses temperature-dependent convection. Cells with sector-shaped solution columns and optically transparent glass windows are aligned inside the rotor (see Figure 1.9). The optical system detects the distribution of sample concentration along the sector radius, with light passing through the cell assembly parallel to the rotor axis. A strong advance experimental setup is achieved by the integration of a laser emitting light at 488 nm. This allows for fluorescence detection of a labeled species [138]. The increased sensitivity of fluorescence detection allows for the application of much lower concentrations [139]. A further benefit is the isolation of the signal for a single labeled species within in heterogeneous solution, which allows for new experimental setup and increases the resolution in size and shape information.

Two major experimental setups are performed in AUC, differing mainly in the centrifugal field applied: Sedimentation Velocity (SV) and Sedimentation Equilibrium (SE). SV experiments aim to analyze the time evolution of radial concentration gradients of particles in solution subjected to a strong centrifugal field [136]. The strongest force in SV experiments is the sedimentation force (F_s), which is the gravitational force on the particle mass [137]. Therefore, F_s is proportional to the particle mass (m) and the gravitational force, i.e., the distance to the center of rotation (r) and the square of the angular velocity (ω), which is the rotor speed (see figure 1.10). During the sedimentation process, the buoyancy force (F_b) on the particles is opposing F_s. F_b is the gravitational force on the displaced volume. The mass of the volume displaced by the particles in solution is dependent on the particle mass, the inverse particle density ($\bar{v}$), and the solvent density (ρ). From these two forces, it can be seen that sedimentation can only occur when the particle density is greater than the solvent density. In the opposite case, flotation causes the particles to move away from the rotor axis. While the sum of these two forces determines the motion of the dispersed particles, a third frictional force (F_f) results from hydrodynamic translation. Due to

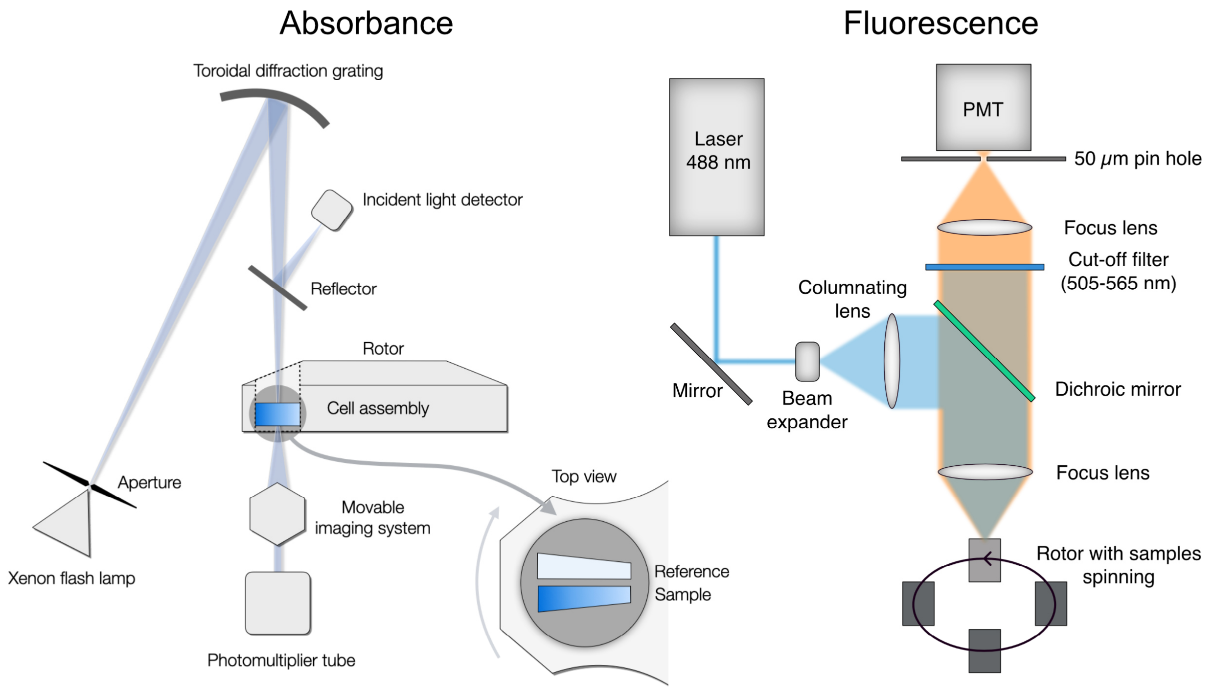

Figure 1.9: Optical systems in analytical ultracentrifugation Schematic representation of the optical systems in the Beckman Optima XL-A Analytical Ultracentrifuge. Absorbance optics (left) can use wavelengths between 190 nm and 800 nm (Recreated from Ralston, 1993 [140]). Fluorescence detection (right) uses 488 nm excitation and collect excitation from 505 nm to 565 nm through a cut-off filter (Recreated from Ralston, 1993 [137]).

particle migration, solvent molecules must be moved in the zone of hydrodynamic drag to create space for sedimenting particles. Therefore, F_f is proportional to the sedimentation velocity (u) of sedimenting particles and a hydrodynamic translational friction coefficient (f). For example, a BSA monomer has a sedimentation coefficient of about 4 S with a sedimentation velocity of about 0.8 μm/sec at 50,000 rpm and exhibits a frictional force of ∼0.05 fN.

$$s = \frac{u}{\omega^2 r} \tag{1.1}$$

By normalizing u relative to $\omega^2 r$, the sedimentation velocity is expressed in a sedimentation coefficient (s) or s-value independent of the applied gravitational force (see Equation 1.1). The s-value is measured in seconds, but for convenience is expressed in Svedberg (S), which equals 10^{-13} sec. Combining all three forces during centrifugation, the s-value can be expressed as proportional to the particle mass (m) with a correction term for buoyancy based on $\bar{v}$ and ρ and

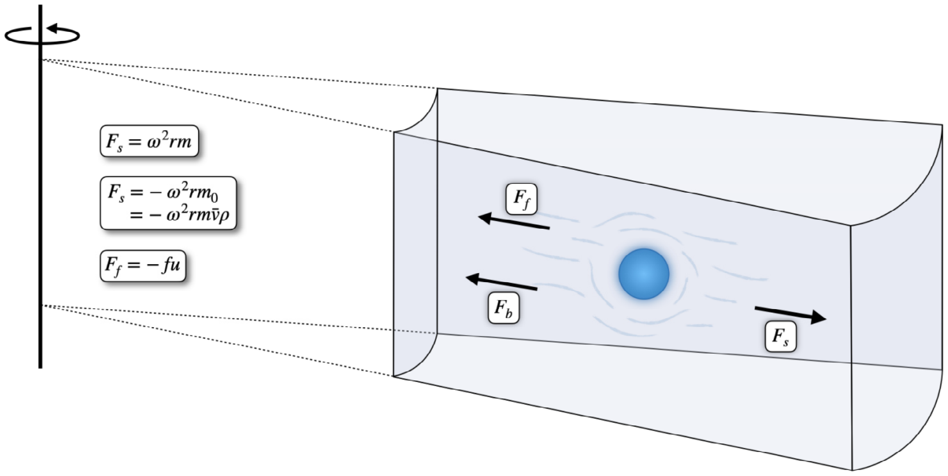

Figure 1.10: Forces acting on particles during centrifugation Forces acting on the particles during centrifugation. The sedimentation force is opposed by a buoyancy force and a frictional force, which results in a constant velocity of the particle migration. Created from Schuck et al., 2016 [137].

inversely proportional to f (see Equation 1.2).

$$s = \frac{m(1-\bar{v}\rho)}{f} \tag{1.2}$$

The frictional coefficient can be expressed according to Stokes' law dependent on the solvent viscosity (η) and Stokes radius (R_S) (see Equation 1.3).

$$f = 6\pi\eta R_S \tag{1.3}$$

R_S represents an equivalent sphere with the same frictional coefficient as the sedimenting particle. Typically, the frictional coefficient of R_S is expressed relative to the frictional coefficient of a theoretical smooth sphere with the radius R_0 (f_0) and the same mass and density as the sedimenting particle, i.e. f/f_0. This frictional ratio describes the excess friction of the sedimenting particle compared to a theoretical particle with the same mass and density but arranged in the most compact form. Therefore, a deviation of f/f_0 from 1 can only be positive and the amplitude describes shape asymmetry. Accordingly, the definition of s can be rewritten (see Equation 1.4). From these information, it can be seen that s provides information about the particle mass, shape, and partial specific volume.

$$s = \frac{m(1-\bar{v}\rho)}{6\pi\eta R_0(f/f_0)} \tag{1.4}$$

Even though the SV experiments focus on fully sedimenting particles, diffusion affects the observed concentration distribution. Assuming that the same translational friction coefficient applies to both sedimentation and diffusion, the Stokes-Einstein relationship (see Equation 1.5 with D the diffusion coefficient, k_b the Boltzmann constant, and T the absolute temperature) together with Equation 1.4 can be used to obtain the Svedberg equation (see Equation 1.6 with R the gas constant and M the molar mass) [141].

$$D = \frac{k_B T}{6\pi\eta R_S} \tag{1.5}$$

$$s = \frac{M(1-\bar{v}\rho)D}{RT} \tag{1.6}$$

An intriguing feature of AUC is that the entire process during centrifugation is concisely captured by a single differential equation, the Lamm equation [137]. This equation describes the evolution of the balance between sedimentation and diffusion fluxes over time (see Equation 1.7) [142].

$$\frac{\delta c}{\delta t} = -\frac{1}{r}\frac{\delta}{\delta r}\left(cs\omega^2 r^2 - rD\frac{\delta c}{\delta r}\right) \tag{1.7}$$

Since this Lamm equation cannot be solved directly, fitting sets of solutions by non-linear least squares method was introduced as a valid procedure [137]. The result of curve fitting using the continuous distribution model $c(s)$ implemented in the software SEDFIT gives a distribution of sedimentation coefficients ($c(s)$ distributions) [143]. The datasets of SV experiments are rich in data, so floating different parameters provide further information, such as molecular mass and interaction parameters [137]. An example of a sedimentation profile is shown in Figure 1.11 including at least two species with visible differences in sedimentation velocity. The SV data show some characteristic features. The solution plateau with a constant signal is reached almost immediately at the first radial scan, as we observe an initial homogeneous particle distribution. This signal decreases with time due to the migration of particles into a larger volume of the sector-shaped solution column. As the particles sediment, the solvent plateau arises at the meniscus and increases radially with time. Between the two plateaus, the sedimentation boundary reports the migration of particles so that the midpoint tracks the particles that started from the meniscus. The shape of the sedimentation boundary shows broadening due to particle diffusion and depends on attractive and repulsive particle interactions. Since the bottom of the sector-shaped solution column constitutes an impermeable barrier, local accumulation of particles leads to a sharp increase in concentration, which results in pronounced back diffusion depending on the molar mass of the particles.

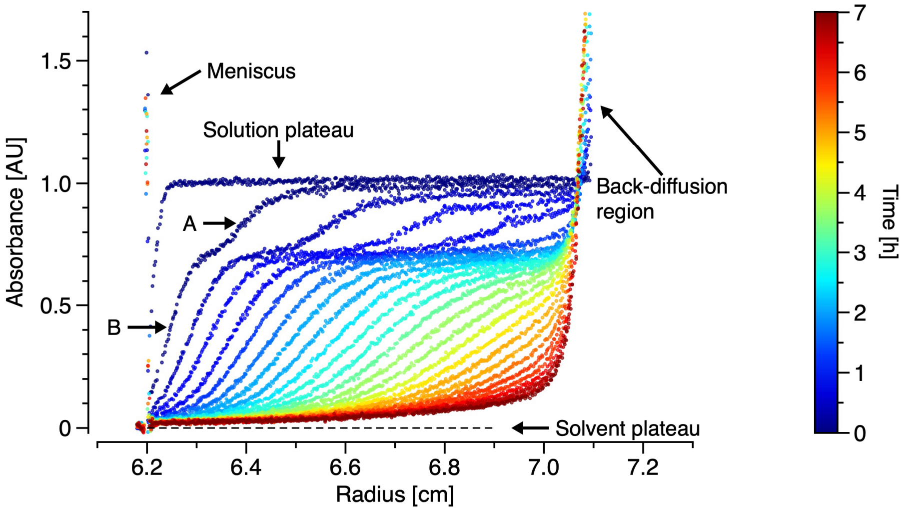

Figure 1.11: Sedimentation profile of an oligomer forming protein An example of an SV measurement showing the sedimentation profile of a protein solution. Typical SV data include a meniscus peak at the air-water interface, a solution plateau, a solvent plateau, and an accumulating concentration near the bottom, forming an area of pronounced back diffusion. Sedimentation boundaries between the solution and solvent plateau report on the migration of particles. Two clearly visible sedimentation boundaries A and B represent at least two species with different sedimentation velocities. The time point of each scan along the radius of the sector-shaped solution column is color-coded.

In contrast to SV, SE experiments aim to extend the back diffusion region to reach throughout the solution column. This is generally achieved by reduced rotor speed. After an appropriate long centrifugation time, an equilibrium situation without net transport is reached, so that kinetic considerations and hydrodynamic friction are irrelevant to the observed signal. The resulting exponential distribution along the radius of the solution column is governed by the molar mass of the particles so that this can be determined directly.

1.7. Circular dichroism spectroscopy

The number of high-resolution structures of proteins has increased immensely since advances in methods such as NMR and cryo-EM. Nevertheless, these methods do not allow for studying protein structure under native conditions, such as low concentrations or in solution. The investigation of a structure under conditions where proteins actually operate can be achieved by CD spectroscopy [144]. In principle, CD is the difference in the absorption of left and right circularly polarized light [145]. Electromagnetic radiation consists of two components, a magnetic field, and an electric field, which oscillate perpendicular to each other in the direction of propagation and describe the wave character of light. In addition, electromagnetic radiation has a particle

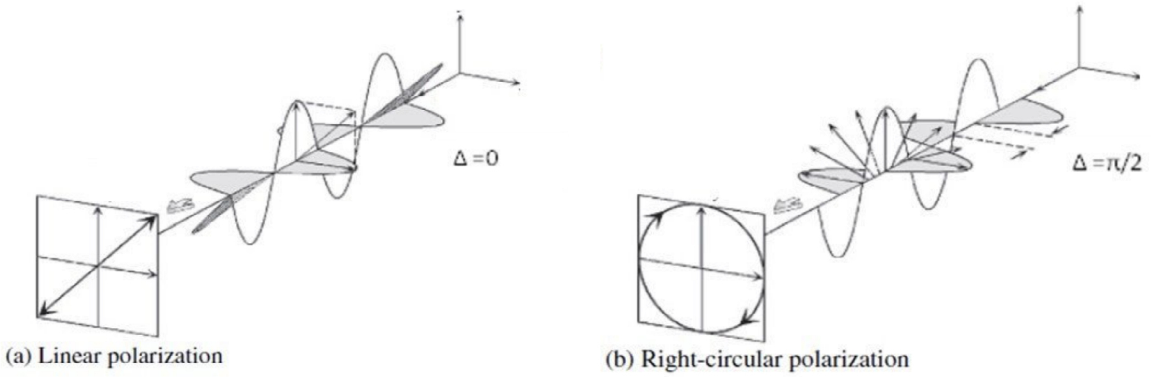

(a) Linear polarization

(b) Right-circular polarization

Figure 1.12: Polarization of light in CD spectroscopy A light wave can possess different polarization states depending on the orientation of the electric and magnetic field components. (A) For linearly polarized light, the phase difference between the electric and magnetic fields is 0. The result is an oscillation in a plane. (B) For circularly polarized light, the two phases oscillate with a 90°offset. The resulting polarization can have two directions, clockwise and counterclockwise or right and left. Adapted from Fujiwara, 2007 [146].

character, so that the absorption of light by molecules can be described by discrete units, namely photons. For natural light, all planes of propagation are equally probable for the oscillating fields. When the magnetic and electric fields of a plane wave oscillate in phase, their combination results in linear polarization (see Figure 1.12). A phase shift of 90°of both fields at the same amplitude results in circular polarization with two possible orientations, clockwise and counterclockwise or left and right rotation. When light with both orientations of circular polarization is transmitted through an optically active sample, a difference in absorption between the two orientations results in elliptically polarized light [144]. CD spectropolarimeters are instruments for measuring the difference in absorption between the two orientations of circularly polarized light and provide characteristic spectra, dichroism as a function of wavelength, which usually report the degree of ellipticity of the transmitted light.

A difference in absorption can be observed in optically active molecules, i.e. chiral molecules, which in proteins is due to the chiral nature of the carbon atoms in the amino acid chain. In proteins, the orientation of the polypeptide backbone in different secondary structure arrangements shows characteristic CD spectra [147]. Typical spectra range from 190 nm to 250 nm due to absorption of the peptide backbone and cover all characteristic bands of secondary structure elements. Two negative bands are observed at 220 nm and 208 nm along with a positive band at 193 nm for α-helical structure [148, 147]. Proteins with β-sheet structure show a typical negative band at 218 nm, as well as a positive band at 195 nm [149, 147]. Random coil structure is characterized by a negative band at 195 nm and a low positive signal above 210 nm [150, 147]. Since CD measures the combined secondary structure of a bulk solution, the recorded spectrum represents a summation of all conformations in a protein solution.

2

DIFFERENTIATION OF SUB-NUCLEUS SIZED OLIGOMERS AND NUCLEATION COMPETENT ASSEMBLIES OF THE Aβ PEPTIDE

2.1. Article information

Title of manuscript: Differentiation of sub-nucleus sized oligomers and nucleation competent assemblies of the Aβ peptide

Authors: Thomas Pauly[1,2], Tao Zhang[1,2,3], Rebecca Sternke-Hoffmann[1,4], Luitgard Nagel-Steger[1,2,*], and Dieter Willbold[1,2]

Journal: Biophysical Journal
Status: Under revision (September 2022)

[1] Institut für Physikalische Biologie, Heinrich-Heine-Universität Düsseldorf, 40225 Düsseldorf, Germany

[2] Institute of Biological Information Processing (IBI-7: Structural Biochemistry), Research Center Jülich, 52425 Jülich, Germany

[3] Present address: Fujian Key Laboratory of Translational Research in Cancer and Neurodegenerative Diseases, Institute for Translational Medicine, School of Basic Medical Sciences, Fujian Medical University, Fuzhou, Fujian 350122, China

[4] Present address: Department of Biology and Chemistry, OFLC/108, Paul Scherrer Institut, Forschungsstrasse 111, 5232 Villingen, Switzerland

[*] luitgard.nagel-steger@hhu.de

2.2. Declaration of article contributions

2.2.1 Experimental

AUC experiments, kinetics, and CD measurements were preformed by me. AFM imaging was performed in collaboration with Rebecca Sternke-Hoffmann.

2.2.2 Data analysis

Data analysis of AUC, kinetics, and CD data was performed by me. AFM images were analysed in collaboration with Rebecca Sternke-Hoffmann.

2.2.3 Manuscript preparation

All figures were prepared by me. AFM images were created in collaboration with Rebecca Sternke-Hoffmann. I wrote the complete manuscript in collaboration with Luitgard Nagel-Steger, Tao Zhang, and Dieter Willbold.

2.3. Abstract

A significant feature of Alzheimer's disease is the formation of amyloid deposits in the brain, consisting mainly of misfolded derivatives of proteolytic cleavage products of the amyloid precursor protein, Amyloid-β peptides (Aβ). While high-resolution structures already exist for both the monomer and the amyloid fibril of the Aβ peptide, the mechanism of amyloid formation itself still defies precise characterization. In this study, low and high molecular weight oligomers (LMWO and HMWO) were identified by sedimentation velocity analysis, and for the first time, the temporal evolution of oligomer size distributions was correlated with the kinetics of amyloid formation as determined by thioflavin T-binding studies. LMWOs of sub-nucleus size contain fewer than 7 monomer units and exist alongside a heterogeneous group of HMWOs with 20 to 160 monomer units that represent potential centers of nucleus formation due to high local monomer concentrations. These HMWOs already have slightly increased β-strand content and appear structurally similar regardless of size, as shown by examination with a range of fluorescent dyes. Once fibril nuclei are formed, the monomer concentration begins to decrease, followed by a decrease in oligomer concentration, starting with LMWOs, which are the least stable species. The observed behavior classifies the two LMWOs as off-pathway. In contrast, we consider HMWOs to be on-pathway, pre-fibrillar intermediates, representing structures in which nucleated conformational conversion is facilitated by high local concentrations. Aβ40 and Aβ42

M35^{ox} take much longer to form nuclei and enter the growth phase than Aβ42 under identical reaction conditions, presumably because both the size and the concentration of HMWOs formed are much smaller.

2.4. Significance

Understanding the molecular mechanisms of how pre-fibrillar intermediates convert into amyloid fibrils is critical for exploring therapeutic options to combat amyloid-related diseases. Sedimentation velocity experiments show the coexistence of at least three different types of oligomeric Aβ42 species. Small oligomers (LMWOs) disappear before larger oligomers (HMWOs) when the reaction enters the growth phase. HMWOs constitute potential nucleation sites by providing high local monomer concentrations facilitating nucleus formation. Lower formation and smaller size of HMWOs from Aβ 40 and Aβ 42 M35^{ox} have been shown to be associated with lower fibril formation compared to Aβ42.

2.5. Introduction

In their recent review about the Aβ oligomer hypothesis Cline *et al.* [151] reported that an increasing number of publications support the idea that toxic oligomeric species of the Aβ-peptide (AβO) are key players in Alzheimer's disease (AD). This switch in focus is already reflected in an increasing number of AβO-targeting therapeutics in the pipelines aiming for a breakthrough in AD therapy [152, 153]. Nevertheless, it is still not clear what type of oligomeric species among the multitude of described Aβ assemblies is a promising target with regard to its size and structure. According to a recent survey, Aβ oligomers correlate poorly with preclinical Alzheimer's neurodegeneration [154]. Therefore it is essential to collect as much information about the nature of these AβOs as possible. Not only their structure but also the kinetics of their formation as well as their function within the framework of amyloid formation have to be resolved [151]. In literature, a multitude of different oligomeric species of Aβ has been described regarding their size, structure, or function [155]. E.g., toxic effects are attributed to AβOs termed Aβ derived diffusible ligands (ADDLs) [156] or to a 60 kDa oligomer termed Aβ42 globulomer which had been detected in human brain [157]. Additionally, it is possible that oligomeric species with different toxic properties exist, which play different roles in the pathology of AD [151, 158]. While fibril structures could be successfully solved for Aβ [159] and other amyloidogenic proteins [160] with high resolution, i.e. by combining solid-state NMR and cryo-electron microscopy, the structure of smaller assemblies of the involved proteins still resists the detailed characterization in atomic resolution [161]. Analyzing the oligomeric species suffers from several obstacles like small quantities in relation to the total concentration of the protein, heterogeneous populations, and a very dynamic and transient nature, which need to be overcome. Here, we use the terms low molecular weight oligomers (LMWOs) and high molecular weight oligomers (HMWOs) to subdivide soluble Aβ oligomers according to their molecular mass. LMWOs by our definition are built out of less than seven monomeric units, while HMWOs include everything larger, e.g. dodecamers [162]. The LMWOs and HMWOs mentioned in this report are Aβ42 intermediate species, which appear after dissolving Aβ42 and disappear in favor of fibrillar structures at the end of the incubation time. They are a group of reproducibly detectable s-value species as evaluated by $c(s)$ distribution analysis [163]. The classified s-value species appear consistently independent of centrifugal speeds, for different protein pre-treatments and total protein concentrations. They can be detected over a wide range of incubation times, although their individual fractions vary with time. The majority of species can be found between 4 and 15 S. A small assembly with about 2.8 S, which is detectable at rather low amounts, has been characterized as penta- to hexamer of Aβ42 already [164]. Analytical ultracentrifugation with either absorbance or fluorescence detection in combination with ThT-based kinetic measurements was used to analyze the evolution of Aβ42 oligomer compositions over time. SV centrifugation allows for the determination of size and shape distributions of macromolecular solutions. It is an absolute, matrix-free solution-based method. In contrast to band centrifugation, the faster sedimenting species are not physically separated from the slower sedimenting components. This property of boundary centrifugation is very advantageous for the analysis of transient and dynamic assemblies, as macromolecular complexes with high dissociation rates are thus protected from dissociation during the measurement [165]. In addition, large fibrils or particles are quickly removed from solution due to their high sedimentation coefficient, so that processes with fast kinetics such as fibril elongation and secondary nucleation do not interfere with the measurement. Although these processes are suppressed during SV centrifugation, they naturally occur during the incubation periods of the samples prior to AUC measurement and thus contribute to the results. Monitoring of molecular concentration gradients formed along the radius during exposure to high centrifugal fields, e.g. $260{,}000\times g$ (60,000 rpm), was performed by either absorbance or fluorescence detection.

The use of the fluorescence detection system (FDS) in AUC enabled the study of Aβ aggregation at low concentrations with a covalently Alexa488 labeled Aβ42 monomer [164]. The disadvantage of this method is the covalent labeling of the monomer unit, which can lead to changes in the aggregation pathway. In contrast, the use of an extrinsic fluorescent dye added to the sample immediately prior to analysis would minimize the potential effects of the dye on aggregation. This approach has been referred to as biological on-line tracer sedimentation (BOLTS) [166].

The use of fluorescent dyes is an established method for the detection of amyloid either in a tissue or in a solution. The two best known dyes are Congo red and ThT11. Unfortunately, neither of these dyes is suitable for FDS of AUC, which offers only one excitation wavelength at 488 nm. Previous AUC measurements with Aβ42 incubated for 24 h and DCVJ [167, 168] as an extrinsic fluorescence probe have shown promising results with staining oligomeric species between 2 and 20 S. SO as a widely used protein stain can bind to amyloid fibrils [169, 170] as well. In this study we examined five different dyes which are suitable for the fluorescence detection system in AUC and promising candidates for the detection of oligomeric species: DCVJ, SO, hFTAA [171], SG and YOYO [172] (see Suppl. Figure 2.6 for the chemical structures and Table 2.1 for the spectral properties of these dyes).

2.6. Results

In our study, we successfully merged kinetic information from ThT measurements with the corresponding aggregate size distributions measured by SV experiments. The essential requirement was a strictly controlled dissolution and incubation protocol for the Aβ peptide, which guaranteed high reproducibility for the aggregation process. To gain more detailed information on the intermediate species several fluorescence dyes were tested for their suitability to stain Aβ42 LMWOs and HMWOs in SV experiments with fluorescence detection. Finally, we applied the advanced technique to variants of Aβ42, i.e. Aβ40 and Aβ42M35^{ox}.

2.6.1 Aβ42 ThT kinetics aligned with aggregate size distributions

ThT is a well-established fluorescent dye used as a marker for amyloid fibrils [173]. It can be utilized in different types of assays either to quantify the amount of amyloid formed over time in a sample or to elucidate mechanistic properties of the process; reviewed in [174]. The ThT kinetic assay performed in parallel to the SV analyses allows the linkage of aggregation stages with s-value distributions for the underlying Aβ42 assemblies. Intermediate species between monomer and amyloid fibril are mostly invisible in ThT kinetics assay probably due to the missing cross-β-sheet structure. SV analysis reports the s-value-distribution of Aβ42 assemblies during the aggregation process, independent of the presence of cross-β structure.

SV analysis was performed in triplicate to analyze the distribution of s-values representing different species of Aβ42 at different stages of aggregation. The sedimentation profiles shown in Figure 2.1 clearly demonstrate the high reproducibility of the aggregation process. The profiles reveal already without further analysis the existence of a faster moving boundary resembling oligomeric species. These oligomeric species were sedimented within ~90 min

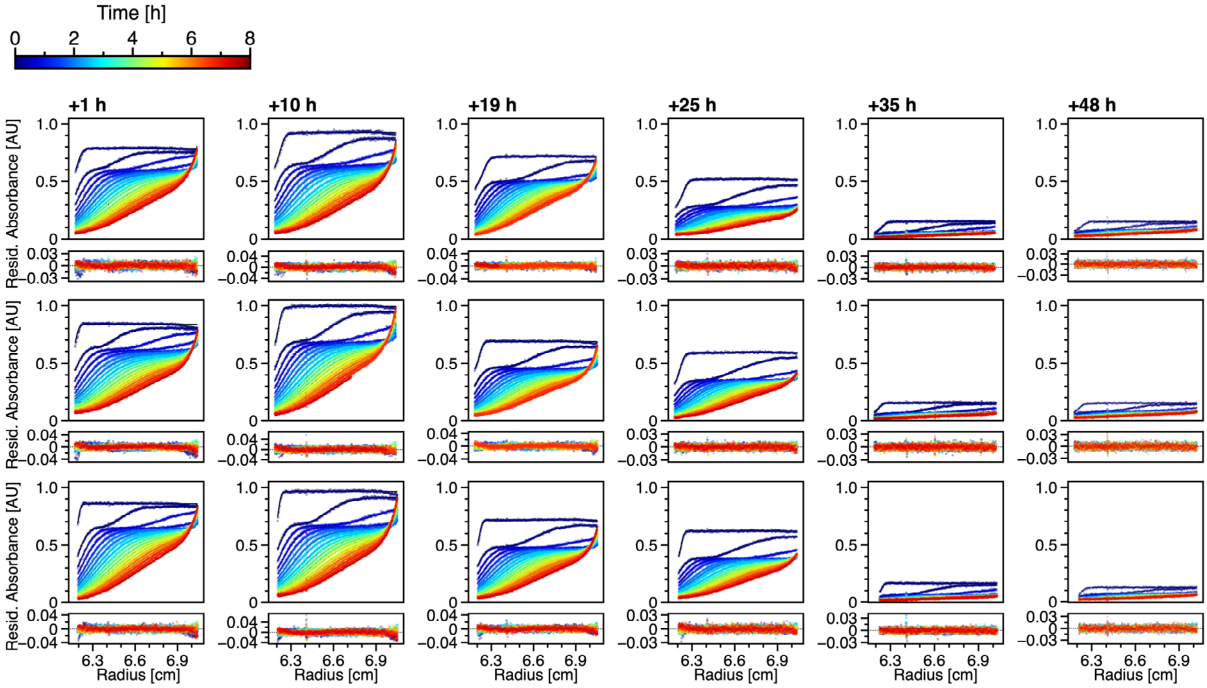

Figure 2.1: Sedimentation profiles of Aβ42 in triplicate after different incubation time Sedimentation profiles of 40 μM Aβ42 after different incubation times (1, 10, 19, 25, 35 and 48 h) at 20°C in triplicates from top to bottom. The raw data (colored dots) is shown together with fitted Lamm equations solutions (black lines) from the *c*(*s*) model implemented in Sedfit. For clarity, only every sixth scan is shown. Below each graph are the residuals depicted, i.e. the deviation of the fit from the measured data. Different colors indicate different time points of detection during sedimentation as shown in the legend on top. The detection wavelengths vary between different measurements.

during our experiments. These raw data were fitted to a model termed continuous distribution of sedimentation coefficients *c*(*s*) [176], which is based on solutions of the Lamm equation [177]. Integration of the obtained *c*(*s*) distributions for two *s*-value ranges, 0 S to 1 S representing monomers and 1 S to 20 S representing oligomers, yielded the corresponding fractions of monomers and oligomers over time (Figure 2.2A). The fraction of large aggregates was calculated for each experiment as a loss of signal during the acceleration of the centrifuge, the corresponding averaged fractions are included in Figure 2.2A. The ThT fluorescence was measured for each sample directly before SV analysis (Figure 2.2B). To confirm the structural conversion of Aβ42, we additionally measured the CD signals for each time point (Figure 2.2C). For Aβ42, it is known that the soluble form is mostly unstructured and amyloid formation is accompanied by increasing β-strand conformation. Since CD is a bulk method, the measured spectra represent weight averages for all molecular species in solution independent of size or ThT-positivity. The concomitant change in CD signal further supports the formation and growth of amyloid structure

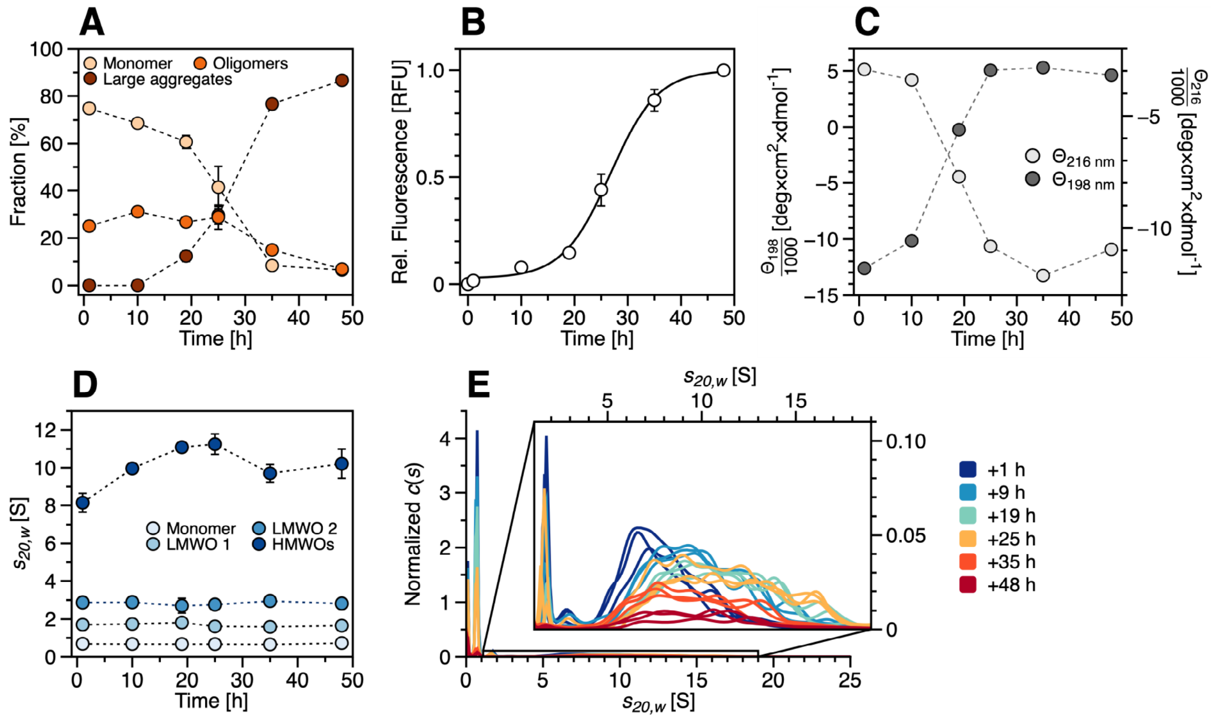

Figure 2.2: Kinetics of amyloid formation of Aβ42 using ThT, SV, and CD measurements Amyloid formation kinetics for 40 µM Aβ42 in 20 mM sodium phosphate buffer (pH 7.4) with 25 mM NaCl or NaF, respectively, were tracked for six incubation time points with different techniques. (A) Time-dependent fraction of different *s*-value species determined by SV analyses. Each data point represents the fraction of the specific *s*-value species of the total amount of Aβ42 at a certain time point of incubation. The integrated signal from *c*(*s*) distributions for a specific *s*-value range, transformed into percentage of total concentration, was used to calculate the fractions for monomers (0 S to 1 S), oligomers (1 S to 20 S), and large aggregates (>280 S) (from yellow to red). Data points represent mean values with standard deviations from triplicate measurements. Error bars may be hidden by dots. (B) ThT fluorescence measurements for triplicate samples over time representing amyloid fibril mass evolution; data (white dots) are fitted with equation 2.1 from [175] (black line). Error bars may be hidden by dots. (C) CD measurements over time. Mean residue ellipticity at 216 nm (light grey dots) and 198 nm (dark grey dots) with separate y-axes. (D) Weight averaged *s*-values from peak integration for monomer and three classes of oligomers over time determined in triplicate (from light to dark blue). Error bars may be hidden by dots. (E) *c*(*s*) distributions in triplicate for different incubation times. The magnification visualizes oligomeric species from 1 S to 19 S. The *c*(*s*) distributions were normalized to one, according to the area under the curve for the complete *s*-value range from 0 to maximum *s*-value and potential material loss, due to large aggregates sedimenting during acceleration was taken into account. Different colors indicate different incubation times.

during the incubation time. The small decrease of random coil structure within the first 9 h of incubation may indicate fold reshuffling processes taking place in and among oligomeric species.

The combination of results from SV analyses and ThT fluorescence kinetics in Figure 2.2A and B presents the evolution of species during the aggregation process. The time where half maximum of the final ThT signal is reached is about 26 h for our system, and the duration of the lag-phase is $\sim$18 h (calculated as the intercept of the time axis and the tangent from the midpoint of the curve [175]). The fraction of large aggregates was calculated based on the quantification of signal loss during acceleration due to aggregates, which are larger than approximately 208 S. It correlates well with the increase of ThT fluorescence and reaches a plateau at $\sim$87 % of the total sample after 48 h. This correlation identifies these aggregates as ThT-positive amyloid structure. A negative correlation is found between the monomer fraction and ThT fluorescence. The class of oligomeric species reaches a maximum of $\sim$31 % just before the entrance into the rapid growth phase after 10 h. The formation of oligomeric species appears to be fast as they could already be detected after 1 h incubation. Their fraction shows a small increase in number for the first 10 h and a rather constant number until 24 h. The results also indicate that at least part of the intermediate species contribute to the ThT fluorescence signal, as we observe some fluorescence signal at the first two time points (1 h and 20 h) before the entrance into the rapid growth phase. At 25 h a strong decrease of the monomer fraction becomes evident along with a sharp increase in the proportion of large aggregates while the oligomeric fraction remains mostly unchanged. Only after the rapid depletion of monomers from the solution, a decrease in the oligomeric fraction is observed. These results support the idea that most if not all of the detectable oligomers are at least at that time point off-pathway species because they dissolve upon the fast consumption of monomers by growth competent nucleus.

To visualize the amyloid fibrils at the end of the observed kinetic, images using atomic force microscopy (AFM) were taken from samples in the plateau of ThT signal after 48 h (supplement Figure 2.9). The AFM images show fibrillar structures with height and diameter in agreement with amyloid fibrils both as single structures as well as superstructures like bundles or meshwork of fibrils. Taken together the results from ThT fluorescence, CD, and AFM strongly support that the presented *in vitro* aggregation system models the amyloid fibril formation process.

2.6.2 SV analysis yields three distinct species of oligomers

Looking at the $c(s)$ distributions it is evident that the oligomeric species belong to at least three distinct classes covering the s-value range from 1 S to 20 S (Figure 2.2E). This s-value range translates into a molecular mass ranging of 10 kDa to 800 kDa based on a frictional coefficient ratio (shape factor, f/f_0) of 1.5. This shape factor was calculated by using a variant of the $c(s)$ model with prior knowledge, i.e. a bimodal f/f_0.The ratio f/f_0 is a parameter of SV analysis which is usually fitted globally for each data set with the drawback that it is dominated by the

s-value species with the highest fraction of signal. Since our $c(s)$ distributions present a baseline separation between the monomer peak ($\sim$0.67 S) and oligomers (starting from $\sim$1.7 S) for most samples it was possible to apply the $c(s)$ model with prior knowledge, i.e. a bimodal f/f_0. The use of this model enables separate determination of shape factors for the monomer fraction and oligomer fraction of a sample, enhancing the overall fitting quality and mass calculation. The group of oligomers is composed of at least three distinct populations. We assign two single peaks at $\sim$1.7 S and $\sim$2.8 S to two distinct LMWOs with masses corresponding to a tri-/tetramer and penta-/hexamer, respectively. The third population is assigned to a group of HMWOs represented as a broader distribution between 4 and 20 S, corresponding to 20 to 160 monomeric units. In Figure 2.2D the weight average s-values for monomer and the three groups of oligomers are shown as the result of the integration of the $c(s)$ distributions. The comparison shows a persistent s-value for monomer as well as the two LMWO species with little deviation during the aggregation process. In contrast to that, the broader distribution of HMWOs exhibits a steady increase of the weighted average s-value from 1 h to 19 h. This increase is observed to stagnate as soon as the system enters the rapid growth phase of amyloid fibrils. It should be noted that the signal for determination of the weighted average s-value for the last two time points is very small due to the high amount of large aggregates at this stage of aggregation. From this change in weight average s-value, we conclude an increase in mass for the heterogeneous group of HMWOs prior to nucleus formation. We could not find any evidence that the increase of the weighted average s-value for these species corresponds to a change in shape.

The system reaches the rapid growth phase after $\sim$18 h which is accompanied by a drastic consumption of monomers due to the formation of growth competent nuclei. The system at that stage is controlled by elongation and secondary nucleation which leads to amyloid fibril formation and as a consequence dissolution of off-pathway assemblies. During the phase of monomer consumption both LMWO species begin to disappear, confirming that these species are the least stable and definitely of sub-nucleus size. The fact that even during amyloid formation no considerable signal can be assigned to s-values between 20 S and 208 S (the detection limit at 60,000 rpm), indicates that nucleation takes place within the size of determined species, up to 20 S, and that their outgrowth is a fast process, leading to an accelerated growth into fast sedimenting amyloid structures that almost immediately leave the complex mixture of oligomeric species and monomers. This prevents the detection of measurable amounts of species above 20 S. This in turn means the nucleus formed under these conditions is extremely competent in monomer recruitment.

2.6.3 Non-covalent fluorescence staining of intermediate Aβ42 species

An assignment was established between aggregate species detected by SV experiments at certain time points during fibril formation and the corresponding ThT fluorescence signal. Large aggregates sedimenting during acceleration of the AUC are ThT-positive and at least part of the ThT fluorescence signal obtained during the lag-phase of amyloid fibril formation is caused by ThT-stainable oligomers. A similar non-zero signal during the lag phase had been observed for Aβ42 before and ascribed to off-pathway oligomers [178]. To further investigate the structural properties of oligomeric species formed before the amyloid fibrils, we tested a set of fluorescence dyes with a variety of different scaffolds and net charges for their capability in binding to oligomers during SV experiments. Although the SV analysis allows a qualitative as well as quantitative characterization of Aβ42 assemblies in solution, it suffers from the high fraction of monomeric species for most of the time points, which limits the precision for oligomer detection. Utilizing fluorescence probes increases the resolution of the species of interest since the chosen extrinsic dyes stain only Aβ42 oligomers but no monomers.

We decided to use an incubation time (6 h) with a sufficient amount of oligomers, but well before amyloid fibril formation to avoid the presence of competing binding sites for the fluorescence dyes. As the fluorescence detection system (FDS) of the AUC uses a 488 nm laser for excitation, the selection of fluorescence dyes is limited and ThT has to be excluded. With an extrinsic, non-covalently binding dye, which can be added shortly before SV analysis and is therefore absent during incubation, a possible impact on the aggregation behavior is minimized. Assuming that a suitable dye is presenting an increase in fluorescence emission upon binding to a specific molecular assembly, we filter the molecular mixture of different species for only the positive staining results. These stained species can be observed during their sedimentation process in the presence of fluorescence dyes. Unbound dyes can be expected not to sediment due to their low molecular mass. We believe that this method can provide more detailed information on the specificity of protein binding dyes for particular oligomeric species than aggregation kinetics or histological staining reactions, which lack information on oligomer size. Our selection of suitable dyes included SO, hFTAA, SG, DCVJ, and YOYO (Table 2.1).

Figure 2.3A-F show the overlays of the $c(s)$ distributions from absorbance detection (black) and fluorescence detection (color) for each dye. It illustrates that all fluorescence dyes have the capability to stain the group of HMWOs between 4 S and 20 S but are limited in binding to the smaller LMWOs. The weighted average s-value for all distributions is similar, except for YOYO (Table 2.2), indicating either no specific staining preferences of the fluorescence dyes or no difference in binding sites among the group of HMWOs. YOYO seems to stain

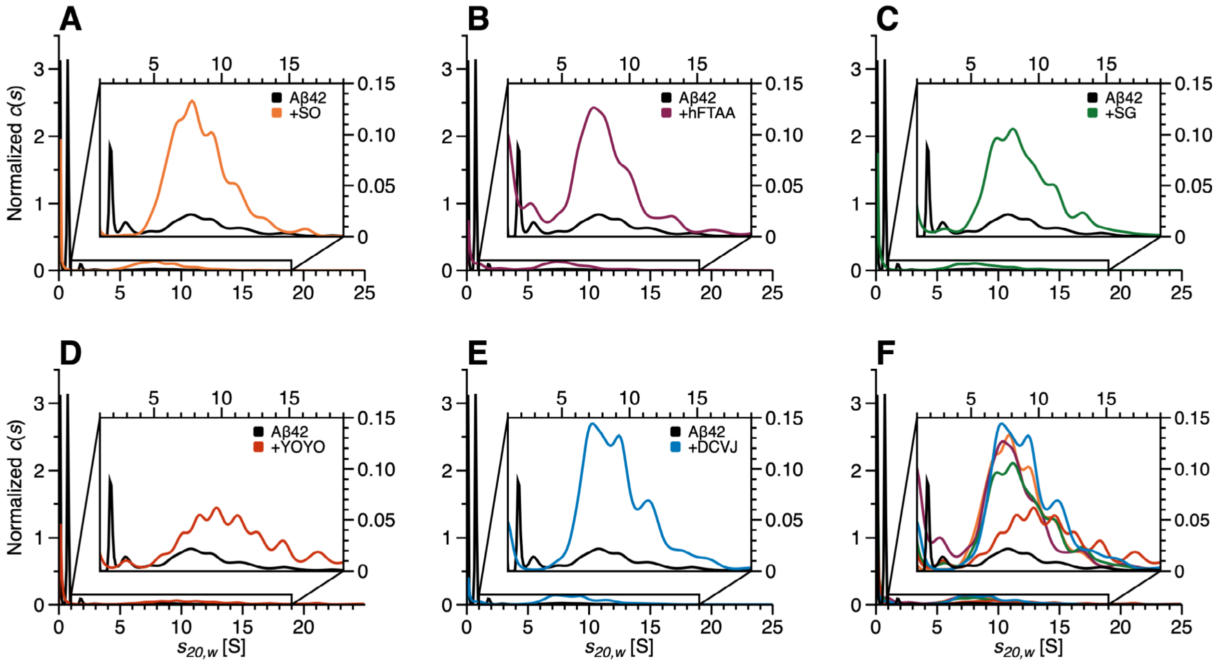

Figure 2.3: Staining Aβ42 oligomers in SV measurements A to E show single $c(s)$ distributions for 40 µM Aβ42 in absorbance (black) and in the presence of different fluorescence dyes and F shows the superposition of all curves. All samples were measured in 20 mM sodium phosphate buffer (pH 7.4) with 25 mM NaCl (2 % DMSO for samples with fluorescence dyes) at 20°C and 60,000 rpm. The incubation time before analysis was 6 h. Magnifications visualize oligomeric species from 1 S to 19 S. The $c(s)$ distributions were normalized to one, according to the area under the curve for the complete s-value range from 0 to maximum s-value.

---

preferentially larger s-value species compared to other dyes. This result could be attributed to an accelerating effect of YOYO on the aggregation process. The incubation of the Aβ42 peptide solution in the presence of the fluorescence dye is limited to the time required to establish the vacuum and equilibrate the temperature, before starting SV experiments (about 1 h). Longer incubation time in the presence of YOYO resulted in accelerated formation of large aggregates which were absent for other fluorescence dyes. A possible explanation could be the positive charge which is exclusive in the group of fluorescence dyes in the present study. Positive charges might compensate for the negative net charge of Aβ and thus reduce electrostatic repulsion.

Looking at the single distributions (Figure 2.3 A to E) overlaid with an absorbance measurement, it is evident that all fluorescence dyes report the smallest species at an s-value between 2 S and 3 S. This species was already identified as a penta-/hexameric LMWO in the time series of absorbance measurements at ~2.8 S (Figure 2.2E). No fluorescence dye reports a clear peak for the smallest, otherwise detectable oligomer, i.e. the tri-/tetrameric LMWO at ~1.7 S

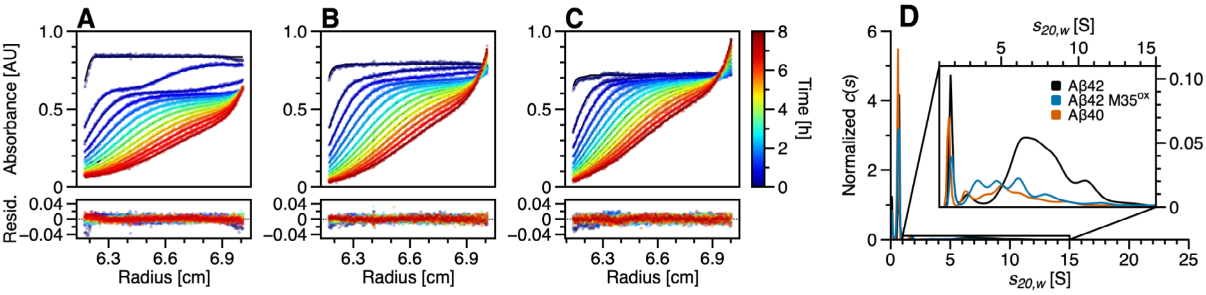

Figure 2.4: Comparison of oligomers formed by variants of the Aβ peptide Comparison of Aβ variants in SV analysis. Raw Data with fitted Lamm equation solutions are shown in A, B and C for 40 µM Aβ42, Aβ42 M35^{ox} and Aβ40, respectively in 20 mM sodium phosphate buffer (pH 7.4) with 25 mM NaCl measured at 20°C and 60,000 rpm. The resulting $c(s)$ distributions after 1 h incubation are shown in D. (Weighted average s-values for HMWOs can be found in Table 2.2.) The $c(s)$ distributions were normalized to one, according to the area under the curve for the complete s-value range from 0 to maximum s-value.

from absorbance measurements or the monomer at ~0.6 S. The s-value distributions show that all selected dyes generally enhance the analysis of intermediate species by ignoring the large monomer fraction of the peptide solution. The selected dyes differ in structure and overall charge, presenting different surfaces for the detection of structural differences among oligomeric species. We conclude that the high similarity of the reported s-value distributions for all fluorescence dyes support common structural features of oligomeric species. This is particularly interesting for the group of HMWOs, as the labeling with either SO, SG, hFTAA, or DCVJ shows no significant differences in terms of affinity for specific s-value species within this population.

2.6.4 Comparison of intermediates for different Aβ variants

After having determined the evolution of Aβ42 aggregate size distributions over time we wanted to know how the oligomer size distributions of closely related Aβ peptides behave. For comparison, we selected the slightly shorter Aβ40 and Aβ42 with the mono-oxidized methionine in position 35, Aβ42 M35^{ox}. For Aβ40, as well as for Aβ42 M35^{ox}, it is known that they aggregate less vigorously than Aβ42 [179, 37]. Figure 2.4 shows $c(s)$ distributions for the two variants in comparison to the Aβ42 peptide. Next to the monomeric peak at ~0.67 S for all variants, the smallest oligomer was detected at ~1.7 S consistent for all variants. Aβ40, as well as Aβ42 M35^{ox}, show a lower amount of HMWOs after the same incubation time at the same concentration and solvent conditions as Aβ42. Additionally, the weighted average s-value for the HMWOs is smaller, presented by the shift of $c(s)$ distribution towards smaller s-values.

The overall fraction of intermediate species is only 12.4 % and 9.6 % for Aβ42 M35^{ox} and Aβ40, respectively compared to 27.5 % for Aβ42. The formation of LMWOs, especially the tri/tetrameric species, is not affected by the difference between the variants and Aβ42. Since the amyloid formation of both variants was so slow under the chosen conditions, we had to refrain from analyzing further time points.

2.7. Discussion

Since in 2004 Klein *et al.* published that small Aβ assemblies instead of fibrils are the proximate neurotoxin in AD, numerous studies were undertaken to identify and characterize these small assemblies [180]. Especially under *in vitro* conditions, oligomeric assemblies are undeniable reaction intermediates present during the aggregation process of Aβ. They can be on-pathway to amyloid fibrils as elongation competent nuclei or much more often off-pathway assemblies. Any on-pathway assembly with a size equal to or larger than the nucleus would not be detectable because of its fast growth. In this study, the time course of Aβ42 oligomer formation was studied.

In parallel with ThT kinetics, the temporal evolution of the s-value distribution of oligomeric assemblies of the Aβ42 peptide was analyzed. SV experiments as a technique to study oligomeric species proved to be especially suited. Since the aggregation process seems to stagnate during analytical ultracentrifugation, it was possible to successfully fit the experimental SV data with a $c(s)$ model for non-interacting species [176] as supported by the low values of the root mean square deviation of ≤ 1 % of the total signal. The accuracy of the SV analysis was demonstrated by the threefold reproduction of results for independently prepared samples for different time points of the Aβ42 aggregation process. Since primary nucleation in this scenario has the highest energy barrier to the formation of Aβ amyloids, we expected that this process would also be largely absent during measurement.

In Figure 2.5 a schematic view of the aggregation process as derived from this study is shown. The aggregation mechanism starts on the left from a supersaturated monomer solution which forms a growth competent nucleus either by chance or *via* nucleation sites [181], e.g. within or on the surface of HMWOs. The final product on the right is the amyloid fibril structure.

The LMWOs of this study are sub-nucleus sized oligomers, i.e. small assemblies with sizes below the critical nucleus. They have s-values of $\sim$1.7 S and $\sim$2.8 S with hydrodynamic radii of 2 nm and 5 nm, respectively, and can be related to species already described in literature [179, 182, 164, 183, 184] ranging from trimers to hexamers of Aβ42. Their s-value is constant over the complete incubation period, but upon entry into the growth phase their amount is the first to decrease after the monomer concentration starts to drop (Figure 2.7).

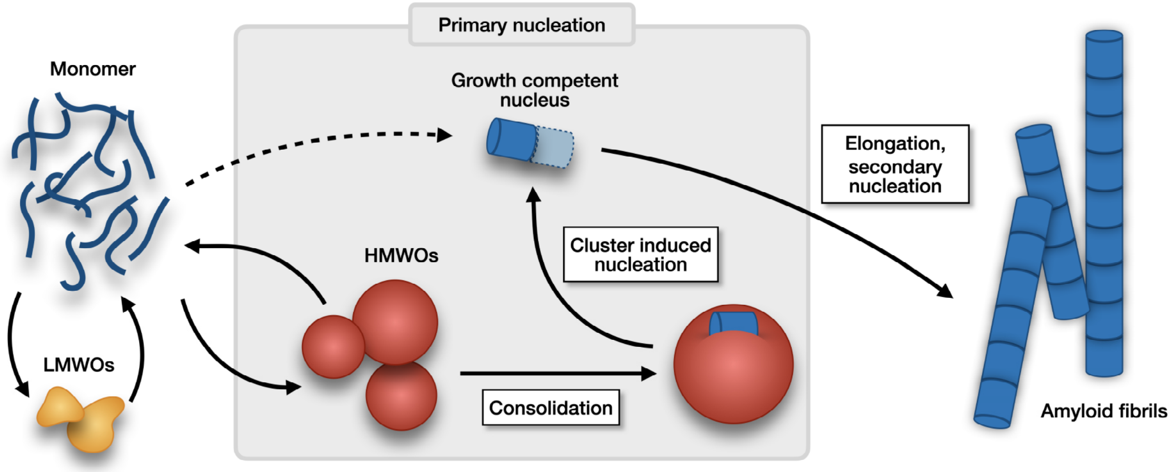

Figure 2.5: Aggregation mechanism of Aβ involving oligomeric intermediates Aggregation mechanism of Aβ42 in the presence of sub-nucleus sized LMWOs and nucleation mediating HMWOs. Monomers are in equilibrium with LMWOs (3 to 6 monomeric units) and HMWOs (20 to 160 monomeric units). Either consolidation of HMWOs or formation of an elongation competent LMWO leads to the formation of a nucleus competent in monomer recruitment which initiates amyloid formation. LMWOs and then HMWOs dissolve upon aggravated monomer consumption through fibril elongation and secondary nucleation.

Aside from LMWOs also HMWOs are present from the first time point onward. They are separated in $c(s)$ curves from the LMWOs by a minimum located between 3 and 4 S. Based on the shape factor $f/f_0 = 1.5$ and the weighted average s-value the molar mass and thus the number of monomeric units could be calculated for HMWOs. After 1 h of incubation the observed s-value distribution between 4 S and 20 S corresponds to about 35 to 47 monomeric units per assembly. Oligomers of a similar size (30 to 50 monomers) with a hydrodynamic radius of 7 nm had been characterized by small-angle neutron scattering [185]. The average number of monomer units of HMWOs doubles to 78 to 89 monomer units by the end of the lag phase. Their fraction decreases last when the system enters the rapid growth phase, where amyloid fibril elongation and secondary nucleation are the dominant processes. A possible explanation for the gradual growth is the energetic favor of larger assemblies due to a decrease in surface energy in analogy to a process known from micelle structures or protein clusters, termed Ostwald ripening. Similar observations were made with lysozyme protein clusters during incubation for the purpose of crystal formation [186, 187]. Furthermore, the increase in size stops as soon as crystallization starts, again resembling what we observe for Aβ42 aggregation. Alternatively, cluster coalescence could be the reason for the increase in size. Despite the high local Aβ concentration and the early presence of the β- strand structure [188], the conformational change or consolidation required to form a growth-competent nucleus still takes several hours. Nevertheless, the nucleation mediated by HMWOs is presumably more probable and outperforms the spontaneous primary nucleation free in solution (dashed line connecting monomers and nucleus) at protein concentrations above a critical value.

The identified sub-nucleus sized LMWOs exist at the same time as a heterogeneous population of HMWOs, which appear to foster nucleation by providing high local Aβ concentrations. HMWOs act as on-pathway species when they promote the formation of nuclei. However, after entering the growth phase, remaining HMWOs are dissolved in terms of off-pathway species as a result of monomer depletion. LMWOs are less stable and disappear before HMWOs (Figure 2.7). The role of HMWOs constituting potential nucleation sites was suggested in our recent review [181]. This hypothesis is further supported by the results, that Aβ40 as well as Aβ42 M35^{ox}, which have a much longer lag phase than Aβ42 under identical solvent and concentration conditions, form less and smaller HMWOs in solution than Aβ42, while the size and amount of sub-nucleus sized LMWOs are comparable. Further, this observation is in line with the findings for the Icelandic mutant (A2T) of Aβ42, which forms *in vitro* only 50 % or fewer oligomers of high molecular weight (>50 kDa corresponding to >11 monomeric units) compared to *wt* protein at the same concentration [189] and significantly reduces the risk for Alzheimer's dementia. The studied variants of the Aβ peptide possess lower hydrophobicity than Aβ42, thus pointing to the hydrophobic effect as a driving force for HMWO formation. Therefore, we conclude that cluster-induced nucleation contributes as another mechanism to amyloid formation in addition to primary and secondary nucleation [190]. This raised the question of whether there is a critical cluster concentration above which the concentration of free monomers remains constant while the total concentration of Aβ42 increases. A concentration series for Aβ42 from 5 to 40 µM peptide gave a linear dependence of free monomer to total Aβ concentration (Figure 2.8). This indicates that a potential critical cluster or oligomer concentration has to be higher than 40 µM.

Since the HMWOs species appeared to be not a single but multiple species within the determined *s*-value distributions the question arose, of whether the heterogeneity would manifest itself in deviating structural properties. Since a physical separation of the different types of HMWOs proved to be unfeasible, a method combining the fractionating properties of AUC and fluorescence staining was chosen. The finding of no differences in stainability is consistent with a uniform micelle or cluster-like structure of HMWOs regardless of size [181]. Monomers and the 1,7 S species could not be stained, probably because their small size does not provide binding sites for the dyes. The BOLT-type SV experiments clearly demonstrated that SO can effectively stain oligomeric species of Aβ42. This is in contrast to statements that SO as an amyloid dye does not stain oligomers [169, 170]. How much the resolution for oligomeric species in SV experiments is improved by the use of a fluorescent dye depends strongly on the quantum yield and the difference between bound and unbound states of the fluorescent dye.

In addition to monomer and fibril, we have identified several intermediate structures that play different roles in the process of amyloid formation and may serve as potential targets for future therapeutic approaches. Aβ42 HMWOs of similar size to those in our study were detected immunologically at physiological Aβ42 concentrations (1-20 nM), with a 48-mer being the prominent species [191]. In the same study, no comparable oligomerization was observed for Aβ40 in agreement with the lower concentrations of HMWOs determined for Aβ40 in our work. LMWOs are less stable than HMWOs and have a higher diffusivity. The toxic capacity of small diffusible species has already been presented [156]. Possibly, the amyloid formation process poses a rescue of the organism from the highly diffusible small oligomeric species. The neuronal damage will probably happen before amyloid deposits are formed due to such ADDLs. Therefore, LMWOs represent potential targets to address the elimination of diffusible species with potential neurotoxicity.

2.8. Material and methods

All samples were prepared and incubated in Protein LoBind tubes from Eppendorf (Hamburg, Germany).

2.8.1 Buffers and solutions

Solutions were prepared using ultrapure water from a Milli-Q filtration system (Merck Millipore, Darmstadt Germany). All experiments were performed in 20 mM sodium phosphate buffer at pH 7.4 including 25 mM sodium chloride. Samples including fluorescent dyes contained 2 % dimethyl sulfoxide (DMSO) of spectroscopic grade (Sigma-Aldrich) as a vehicle to improve dissolution. DMSO was excluded from experiments with absorbance detection.

2.8.2 Aβ peptide and fluorophores

Aβ aliquots were prepared by dissolving 1 mg peptide (Bachem, No. 4014447.1000) in 700 µl 1,1,1,3,3,3-hexafluoroisopropanol (HFIP) (Sigma-Aldrich, Germany) overnight at room temperature (RT) without agitation. Consequently, HFIP was removed in a vacuum concentrator. Dried peptide films were stored at -20°C until use. Any dissolution of such prepared Aβ42 aliquots started with the addition of less than 10 % final volume of 10 mM NaOH before adjusting final solvent conditions. The quality of the peptide was examined by sedimentation velocity analysis of peptide dissolved in 10 mM NaOH, revealing *geq* 95 % monomeric Aβ peptide

(This experiment was performed in titanium cells because of their higher chemical resistance.). The fluorescent dyes are listed together with the solvent used to prepare the stock solutions in Table 2.1.

2.8.3 Analytical ultracentrifugation

SV experiments were performed in an analytical ultracentrifuge (Proteome Lab XL-A, Beckman-Coulter, Brea, US) at 60,000 rpm, 20°C, and with a radial resolution of 0.002 cm in standard double sector cells (optical path length 1.2 cm) made of either aluminum (Beckman-Coulter, Brea, US) or titanium in case of extreme pH. At the beginning of each experiment, a wavelength scan at 3,000 rpm was recorded to determine the optimal detection wavelength and as a reference to quantify the amount of material sedimented during acceleration to 60,000 rpm. The rotor used was an An-60Ti (4-hole) rotor from Beckman. The stated times of incubation were those times that passed between Aβ sample preparation and the start of sedimentation. SV data analysis was performed by applying a continuous distribution Lamm-equation model, $c(s)$, as implemented in Sedfit (version 16p35) [176]. Regularization was performed with maximum entropy algorithm, which favors the distribution with the lowest number of parameters (minimal information) to fit the data. Additionally, Datagraph [192] was used for data presentation.

After incubation at RT samples were loaded into aluminum cells. The size distribution of Aβ42 was measured in triplicate with separate incubation for each time point, resulting in 21 independent aggregation processes, which were evaluated by SV analyses. If aggregation had taken place during incubation, we observed a loss of signal during acceleration of the centrifuge to final speed. This signal loss due to the sedimentation of large assemblies was accounted for in the final size distributions. The final $c(s)$ curves were transformed into standardized signal units representative of the sample concentration found when the final speed was achieved.

2.8.4 ThT kinetic measurement

For the ThT-based quantification of fibril mass, a 100 µl aliquot of the 40 µM Aβ42 sample for SV experiments was taken, and 1 µl ThT stock solution was added for a final concentration of 20 µM. Samples were measured in LoBind multi-well plates (Eppendorf, Hamburg, Germany) inside a microwell plate reader (Tecan, Männedorf, Switzerland). To prevent evaporation, plates were sealed. The ThT fluorescence was measured from the top with λ_{ex} = 445 nm and λ_{em} = 485 nm with a bandwidth of 9 nm each at 20°C without agitation.

2.8.5 CD spectroscopy

The secondary structure conversion of Aβ42 over time was characterized using circular dichroism (CD) spectroscopy. Aβ42 at 40 μM was prepared in 20 mM sodium phosphate, 25 mM sodium fluoride (pH 7.4). The exchange of chloride by fluoride increases the sensitivity of CD in the far UV region below 200 nm. Samples of 200 μl each were then loaded into a 1 mm quartz cuvette and were maintained at 20°C. CD spectra were recorded using a J-815 spectropolarimeter (Jasco, Tokyo, Japan) from 260 nm to 190 nm, with a step size of 0.5 nm and a bandwidth of 2 nm. The scanning speed was 100 nm/min. For each time point, 10 scans were accumulated and averaged for a spectrum of the sample. Calculated mean residue ellipticities at either 216 nm or 198 nm were plotted against the incubation time to visualize the conversion kinetics.

2.9. Supporting information

2.9.1 Supporting material and methods

The obtained ThT fluorescence data were fitted by a sigmoidal function that allows to obtain the lag time of amyloid fibrils formation [175]. The fitted parameters are the elongation rate constant (k), the half completion time ($t^{1/2}$), the lower fluorescence baseline (F_0), and the amplitude to reach the upper baseline (A).

$$F(t) = F_0 + \frac{A}{1 + \exp(-k(t - t^{1/2}))} \tag{2.1}$$

For AFM imaging, Aβ42 in 20 mM Sodium phosphate buffer with 25 mM sodium chloride was incubated for 48 h before dilution from 40 μM to 20 μM and preparation of AFM samples. MICA surfaces were incubated for 20 minutes with 10 μl peptide solution, followed by washing steps with water and dried with nitrogen. Images were obtained using a NanoScope V (Bruker) atomic force microscope equipped with a silicon cantilever ScanAsyst-Air with a tip radius of 2 nm to 12 nm. Images were processed with Gwyddion 2.56 for presentation.

Detailed information of fluorescent dyes used in this study are shown in Figure 2.6 and listed in Table 2.1.

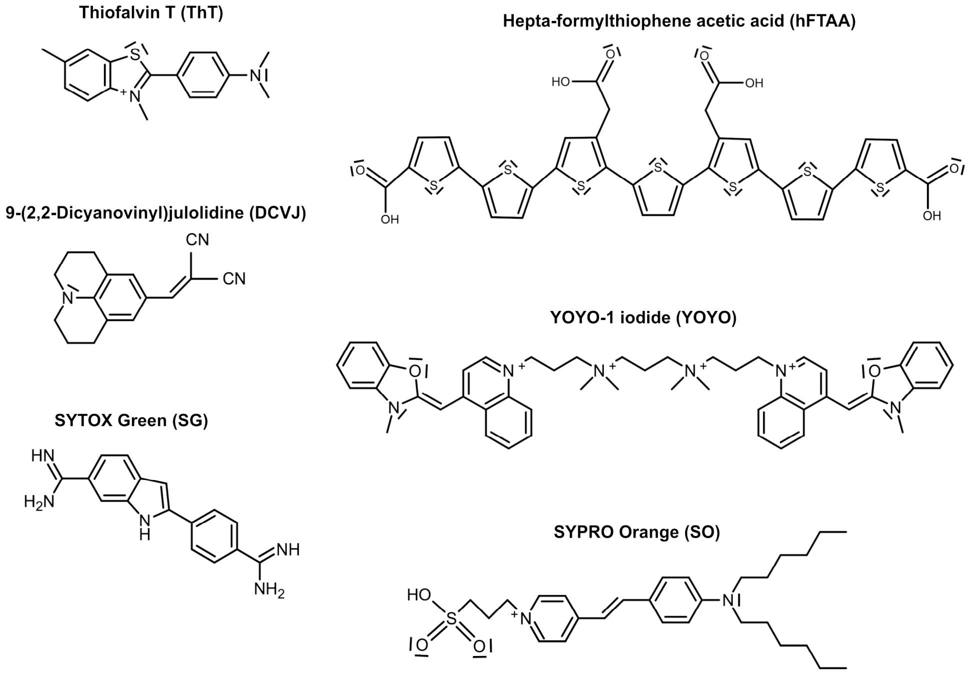

Figure 2.6: Structure of fluorescence dyes used for probing Aβ42 oligomers Molecular structures of fluorescent dyes used in this study.

Table 2.1: Fluorescence dyes used for probing Aβ42 oligomers. Fluorescence dyes with respective net charge and solvent used in this study

Dye	**Source**	**Solvent**	**Charge** [$\times 1.602 \times 10^{-19}$ C]
ThT	Sigma-Aldrich, Germany	Water	$+1$
DCVJ	Sigma-Aldrich, Germany	DMSO	neutral
SO	Sigma-Aldrich, Germany	DMSO	zwitterionic
hFTAA	Nilsson and Hammarström [171]	Water	-4
YOYO	ThermoFisher, Germany	DMSO	$+4$

2.9.2 Supporting results

The average size of oligomers is determined by weighted average s-value, shown in Table 2.2.

Table 2.2: Weighter average s-values of oligomers of Aβ peptide Weighted average s-value for oligomers from $c(s)$ distributions.

Sample	Detection type	average s-value [S]
		Oligomers from 4 to 20 S
Aβ42	Absorbance	9.16
Aβ42 + SO	Fluorescence	8.63
Aβ42 + hFTAA	Fluorescence	8.66
Aβ42 + SG	Fluorescence	9.03
Aβ42 + YOYO	Fluorescence	11.02
Aβ42 + DCVJ	Fluorescence	9.24
		Oligomers from 2 to 20 S
Aβ42	Absorbance	8.65
Aβ42 M35^{ox}	Absorbance	6.92
Aβ40	Absorbance	7.12

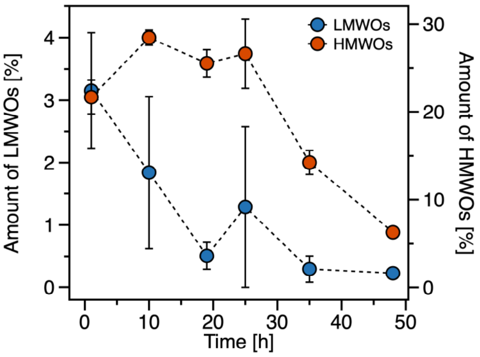

Figure 2.7: Kinetics of oligomers Amount of small oligomers and clusters of 40 µM Aβ42 for different incubation time points as the result of peak integration from 1.2 S to 4 S (blue dots) and 4 S to 20 S (red dots), respectively.

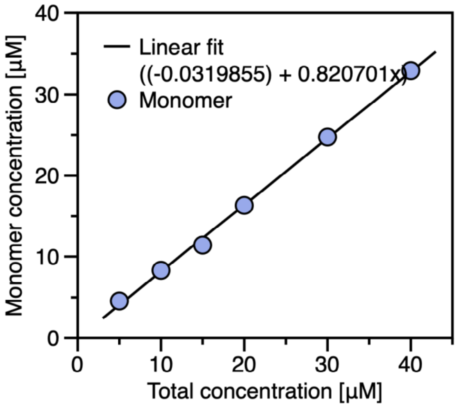

Figure 2.8: Aβ42 concentration series Integration of monomer peak from $c(s)$ distributions obtained for a concentration series of Aβ42 without pre-incubation in 20 mM NaPi with 25 mM NaCl (pH 7.4). The monomer concentration dependence from total peptide concentration can be described by a linear relation between 5 µM and 40 µM.

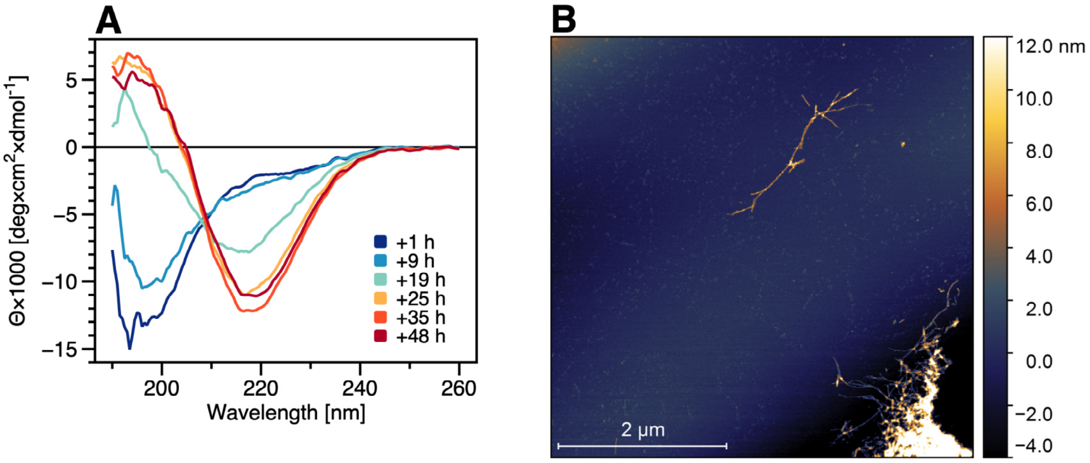

Figure 2.9: Structure of Aβ42 amyloid fibrils A shows CD spectra for 40 µM Aβ42 after different incubation times. B shows an AFM image of 20 µM Aβ42 after 48 h incubation. Samples were taken from kinetic experiments with 40 µM Aβ42 and diluted with 20 mM NaPi and 25 mM NaCl (pH 7.4).

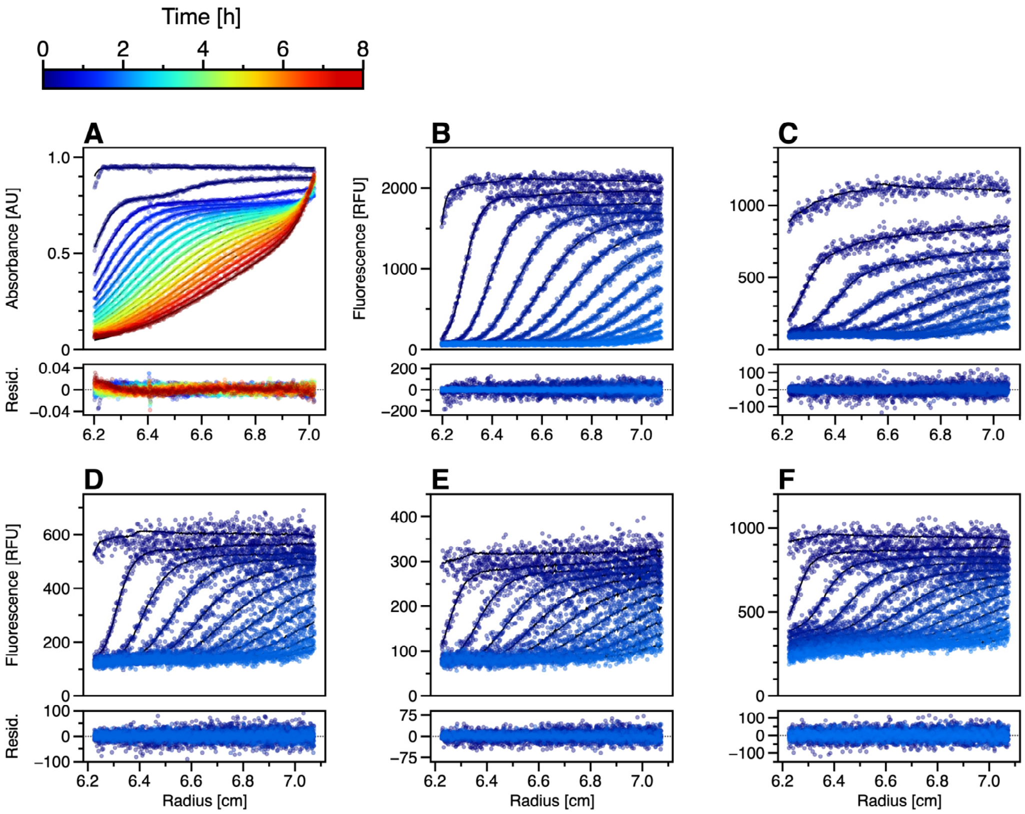

Figure 2.10: Fluorescence sedimentation profiles Sedimentation profiles of 40 µM Aβ42 after 6 h incubation measured with absorbance detection (A) and with fluorescence detection in the presence of different dyes: SO (B), YOYO (C), SYTOX (D), DCVJ (E) and hFTAA (F). The raw data is shown as points with fitted Lamm-equations solutions from the *c*(*s*) model implemented in Sedfit. For clarity, only every seventh scan is shown.

3

MET/VAL129 POLYMORPHISM OF THE FULL-LENGTH HUMAN PRION PROTEIN DICTATES DISTINCT PATHWAYS OF AMYLOID FORMATION

3.1. Article information

Title of manuscript: Met/Val129 polymorphism of the full-length human prion protein dictates distinct pathways of amyloid formation
Authors: Thomas Pauly[1,2,‡], Najoua Bolakhrif[1,2,‡], Jesko Kaiser[3], Luitgard Nagel-Steger[1,2], Lothar Gremer[1,2], Holger Gohlke[3,4,5,6], and Dieter Willbold[1,2,*]
Journal: Journal of Biological Chemistry
Status: Published (August 2022)

[1] Institut für Physikalische Biologie, Heinrich-Heine-Universität Düsseldorf, 40225 Düsseldorf, Germany
[2] Institute of Biological Information Processing (IBI-7: Structural Biochemistry), Research Center Jülich, 52425 Jülich, Germany
[3] Institute for Pharmaceutical and Medicinal Chemistry, Heinrich-Heine-Universität Düsseldorf, 40225 Düsseldorf, Germany
[4] Jülich Supercomputing Centre (JSC), Forschungszentrum Jülich GmbH, 52425 Jülich, Germany
[5] Institute of Bio- and Geosciences (IBG-4: Bioinformatics), Forschungszentrum Jülich GmbH, 52425 Jülich, Germany
[6] John von Neumann Institute for Computing (NIC), Forschungszentrum Jülich GmbH, 52425

Jülich, Germany
* d.willbold@fz-juelich.de
‡ Authors contributed equally

3.2. Declaration of article contributions

3.2.1 Experimental

AUC experiments, kinetics, CD measurements, and absorbance measurements were performed by me and Najoua Bolakhrif.

3.2.2 Data analysis

Data analysis of AUC experiments, kinetics, CD measurements, and absorbance measurements was performed by me and Najoua Bolakhrif.

3.2.3 Manuscript preparation

All figures were prepared by me and Najoua Bolakhrif. I wrote the complete manuscript in collaboration with Najoua Bolakhrif, Jesko Kaiser, Holger Gohlke, Luitgard Nagel-Steger, Lothar Gremer, and Dieter Willbold.

3.3. Abstract

Methionine/valine polymorphism at position 129 of the human prion protein, huPrP, is tightly associated with the pathogenic phenotype, disease progress, and age of onset of neurodegenerative diseases such as Creutzfeldt-Jakob disease or Fatal Familial Insomnia. This raises the question of whether and how the amino acid type at position 129 influences the structural properties of huPrP, affecting its folding, stability, and amyloid formation behavior. Detailed biophysical characterization of the 129M and 129V variant of recombinant full-length huPrP(23-230) by amyloid formation kinetics, circular dichroism spectroscopy, molecular dynamics simulations, and sedimentation velocity analysis reveal differences in their aggregation propensity and oligomer content, leading to deviating pathways for the conversion into amyloid at acidic pH. The 129M variant exhibits less secondary structure content before amyloid formation and higher resistance to thermal denaturation compared to the 129V variant, whereas the amyloid conformation of both variants shows similar thermal stability. Molecular dynamics simulations and rigidity analyses at the atomistic level identify intramolecular interactions responsible for the enhanced monomer

stability of the 129M variant, involving more frequent minimum distances between E196 and R156, forming a salt bridge. Removal of the N- terminal half of the 129M full-length variant diminishes its differences compared to the 129V full-length variant and highlights the relevance of the flexible N-terminus in huPrP.

3.4. Introduction

Transmissible spongiform encephalopathies are also known as prion diseases since they are based on the misfolding of the prion protein [193]. HuPrP is a membrane-bound glycoprotein, located mainly in nervous tissues, such as the brain and spinal cord. Two isoforms are known: the cellular form (huPrP^{C}) is non-pathogenic, rich in α-helices (42 %) and contains a single, small β-sheet (3 %) [194]. The other isoform, associated with the disease (huPrP^{Sc}), contains 34 % to 43 % β-sheets and 20 % to 30 % α-helices [194, 195]. Prions are defined as proteinaceous infectious particles [50], which in contrast to viruses lack any genetic information provided by nucleic acids. The structural conversion from huPrP^{C} into huPrP^{Sc} and aggregation into toxic oligomers and fibrils is governed by autocatalytic processes [42]. Recently published high-resolution structures of PrP amyloid fibrils by cyro-EM revealed a typical β-sheet structure [196, 58]. Several neurodegenerative diseases such as CJD, FFI, Gerstmann-Sträussler-Scheinker syndrome and Kuru are human prion diseases and associated with these amyloid structures. The well-known methionine/valine polymorphism at position 129 appears in the cellular conformation at the beginning of the first β-strand (Figure 1A). About 51 % of the human population are heterozygous at position 129, 12 % have a genotype of valine/valine, and the remaining 37 % a genotype of methionine/methionine [197]. This methionine/valine polymorphism is associated with the age of onset, the disease progress and which pathogenic phenotype is developed in patients [198, 199, 200, 201]. The polymorphism at position 129 raises the question of how it determines the pathogenic roles, especially with respect to the aggregation behavior during the conversion of huPrP^{C} into huPrP^{Sc}. In several studies properties of the amyloid fibril structure [202] and unfolded state [203, 204] of different prion protein variants had been investigated, revealing not only different amyloid fibril morphologies [205] within these variants and other mutations [206], but also further requirements for fibril formation such as a disulfide bond [204]. This work presents a detailed biophysical characterization of full-length huPrP(23-230) for both variants and a comparison with a shorter construct, lacking the unstructured N-terminal region, huPrP(121- 230) for the 129M variant. Understanding the impact of a single amino acid residue exchange on the propensity of huPrP to convert into the pathogenic amyloid structure in vitro will help to gain insights into the pathomechanisms of prion diseases. Since the recombinantly produced full-length huPrP(23-230) does not aggregate spontaneously at physiological pH within manageable time ranges, we established an in vitro conversion system at acidic pH with additional destabilization by guanidine hydrochloride (GdnHCl). Amyloid formation kinetics monitored by the fluorescence dye ThT was used to examine aggregation pathways. CD spectroscopy was used to determine the secondary structure content before and during the amyloid formation process as well as the thermal stability before and after amyloid formation. Additionally, molecular dynamics (MD) simulations and rigidity analyses were performed to investigate the stability of both variants in detail. SV analysis was performed to investigate the monomeric and oligomeric states before amyloid formation.

3.5. Results

Differences in amyloid formation kinetics of both variants monitored by ThT fluorescence are presented in Figure 3.1B. At pH 2.0 we used 0.5 M GdnHCl for an additional weak destabilization of 15 µM huPrP(23-230) to accelerate conversion into an amyloid structure (different conditions for huPrP and GdnHCl concentrations were tested, see Figure 3.5, 3.6, 3.7). Strikingly, both variants behave distinctly in the ThT kinetic assay. However, both variants have in common that neither amyloid formation nor an initial fluorescence plateau occurred in the controls without GdnHCl (Figure 3.5), indicating no conversion of huPrP(23-230) without destabilization within the observation time. The 129M variant shows a more complex amyloid formation behavior, resembling kinetics with multiple phases. The kinetics to reach the final plateau are retarded compared to the 129V variant and passing through two interim plateaus. The 129M variant shows clear initial ThT fluorescence identical to the triplicates. The first steep increase starts reproducibly at about 25 h. Differences are observed in the duration of the single growth phases, their number and heights of interim and final plateaus. The time point of the second increase is approximately 55 h. Overall, the reproducibility within the triplicates is low. In contrast, the 129V variant shows an immediate steep ThT fluorescence increase without any lag phase. The amyloid formation of the 129V variant exhibits a single-phase aggregation behavior. The reproducibility among the triplicates is high. Nevertheless, despite the obvious differences, both variants result in rather similar ThT fluorescence after 120 h. Measuring the concentration of the soluble fraction after 120 h revealed 72.5 % and 84.1 % of aggregated protein for the 129M and 129V variants, respectively (Figure 3.8).

CD spectra were measured to determine the secondary structure content of huPrP (Figure 3.1C). Here, 10 µM huPrP(23-230) without GdnHCl before amyloid formation at pH 2 was analyzed for both variants (Figure 3.1C, left). Since CD is a bulk method, the signal represents the weighted average in secondary structure content for the sample. Oligomeric species with

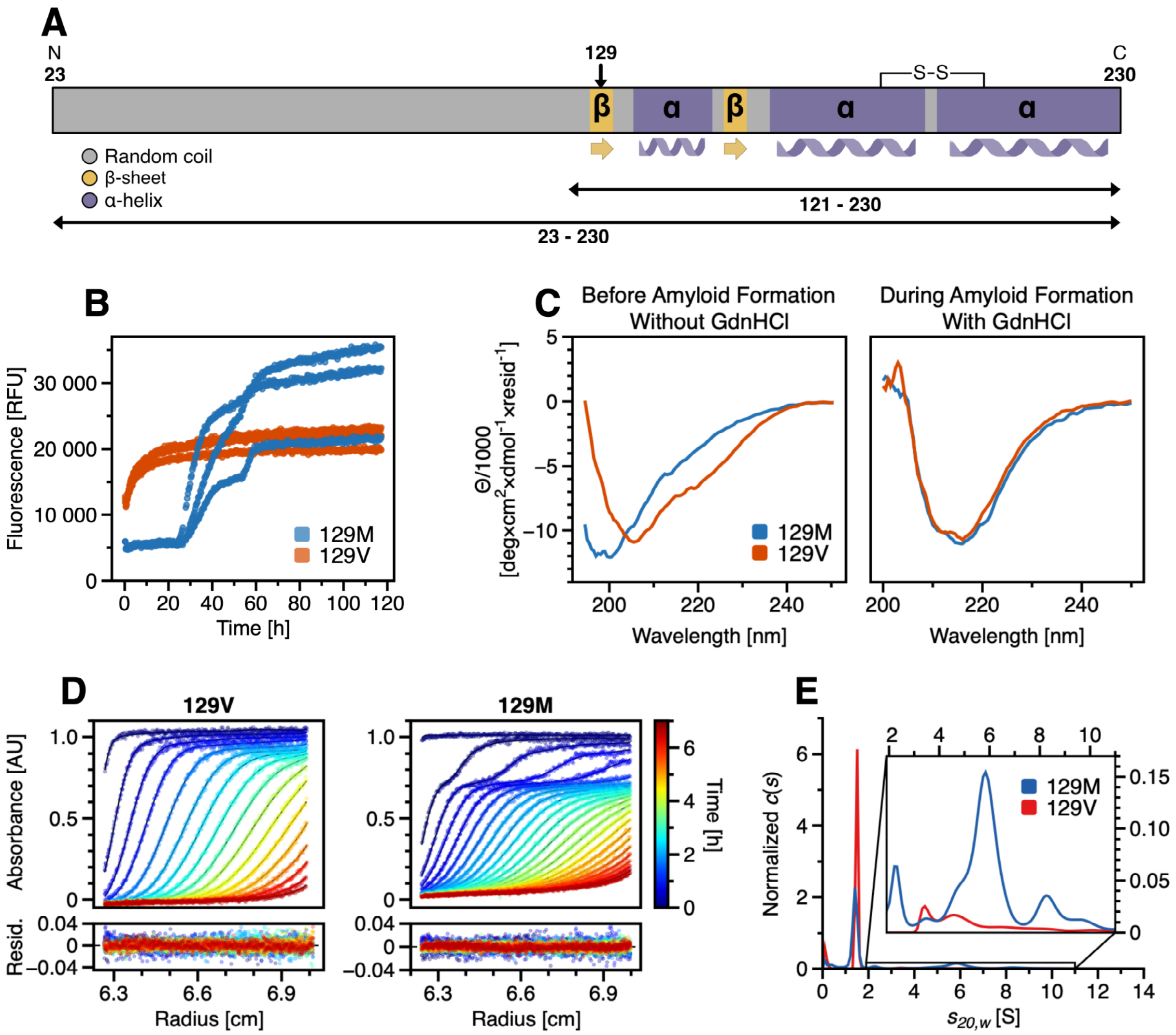

Figure 3.1: Aggregation behavior of full-length huPrP(23-230) (A) Scheme of full-length huPrP(23-230) secondary structure elements. huPrP(23-230) comprises the unstructured N-terminal half and structured C-terminal domain, containing a disulfide bond between C179 and C214; huPrP(121-230) lacks the unstructured N-terminal region. (B) Amyloid formation kinetics are monitored by ThT fluorescence for triplicates of the 129M variant (blue) and 129V variant (red). 15 M huPrP(23- 230) was incubated with 0.5 M GdnHCl for destabilization and initialization of amyloid formation. (C) Secondary structure are represented in CD spectra of 10 µM huPrP(23-230) without (left) and with 0.5 M GdnHCl after 5 h incubation (right) for both variants. The incubation conditions are identical to amyloid formation kinetics. (D) SV analysis of 7.5 µM of both variants without GdnHCl. Raw data from SV analysis with fitted Lamm-equation solutions from $c(s)$ model are color-coded for the duration of sedimentation. (E) The result of data fitting is an s-value distribution.

different monomer conformations might contribute to the measured spectra. For both variants we observed CD spectra with a shape resembling a mixture of mainly α-helical and random coil structure. The position of the first minimum differs; it is at about 200 nm for the 129M variant and about 207 nm for the 129V variant. Additionally, a more positive signal between about 207 nm and 240 nm is observed for the 129M variant, suggesting a somewhat higher content of random coil structure. The secondary structure content was also investigated at time points during the amyloid formation process in the presence of 0.5 M GdnHCl (Figure 3.1C, right, Figure 3.10). Five hours after the addition of GdnHCl, a horizontal shift of the minimum from 200 nm to approximately 218 nm is observed for both variants, indicating an increase in β-strand conformation. This shift barely changes for longer incubation time but a drop of the peak signal at 218 nm was observed together with a loss of the accompanying uv absorbance signal (Figure 3.10), so that one can assume a loss of soluble protein due to aggregation [207]. These results support the conversion into amyloid for both variants. Although the amyloid formation behavior of the 129M variant seems retarded and follows a more complex and time-consuming mechanism, the difference in amyloid formation behavior between both variants is not reflected in the secondary structure of converted forms.

SV analysis was performed to characterize the hydrodynamic properties of both variants at pH 2 and examine the molecular assemblies present before amyloid formation (Figure 3.1D and E). These conditions can be referred to as starting conditions before GdnHCl is added for destabilization and initialization of amyloid formation. Figure 3.1D shows raw data as sedimentation profiles with fitted Lamm-equation solutions. The resulting distribution of standardized sedimentation coefficients ($s^{20,w}$) presents differences in the degree of oligomerization between both variants (Figure 3.1E). Molar mass is calculated based on the globally determined frictional ratio (f/f_0), which is proportional to the hydrodynamic radius. At pH 2 f/f_0 was about 2.2 for both variants, indicating an elongated shape. The 129M variant shows a faster sedimenting oligomer boundary, representing 31.6 % of the total signal and corresponding to s-values between 2 S and 15 S (potentially dimers to 15-mers). The remaining 68.3 % of the sample can be assigned to the monomer state at 1.41 S. In contrast, most of the 129V variant is monomeric (93.1 %) at 1.49 S and only 6.8 % are oligomers between ~2 S and ~15 S. A closer examination of the oligomer distribution yields significant differences for the smallest detectable species. A distinct peak can be assigned at 2.3 S for the 129M variant with a molar mass corresponding to a dimer. The smallest oligomer of the 129V variant can be assigned to a peak at 3.5 S with a molar mass appropriate for a trimer. The peak at 3.5 S can also be found in the distribution of the 129M variant. The 129M variant is more susceptible to oligomerization than the 129V variant and forms dimers at pH 2 without GdnHCl. The addition of GdnHCl had no impact on the monomer sedimentation coefficient corrected for increased density and viscosity of both variants. This indicates a similar shape of the monomer both in the presence and absence of GdnHCl and, thus,

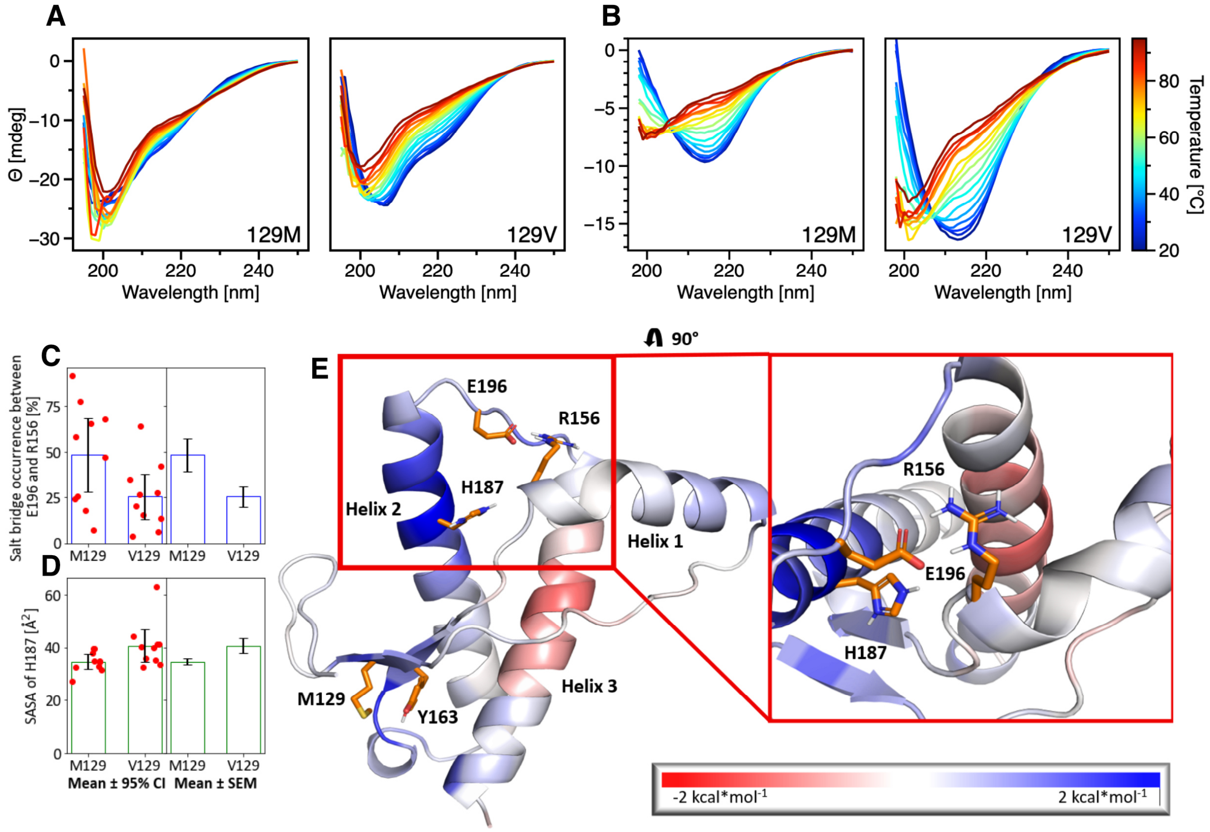

Figure 3.2: Stability of huPrP (A) Thermal denaturation over a temperature range from 20°C to 95°C before amyloid formation at pH 2 and (B) after amyloid formation at the end of kinetic experiments (after 120 h) of both variants of full-length huPrP(23-230). CD spectra of 10 µM of the 129M (A, left) and 129V (A, right) variant. CD spectra of end products from amyloid formation kinetics of 20 µM of the 129M (B, left) and 129V (B, right) variant. (C) Occurrence of salt bridge formation between E196 and R156 and (D) SASA values of H187 during MD simulations for both polymorphs. In (C) and (D), the mean 95 % CI and all data points (left), and the mean ± standard error of the mean (right) are shown; the two mean values differ significantly, respectively (see text). (E) Differences of the residue–wise structural stability as determined from rcij,neighbor maps from CNA mapped onto the non-amyloid conformation of huPrP(118- 224). Blue indicates that the respective area is more stable in the 129M variant.

only minor changes in the fold induced by GdnHCl facilitate amyloid formation. A similar effect was published before with urea as a denaturant [207].

To probe differences in thermal stability, CD spectra of 10 µM huPrP(23-230) for each variant were recorded over a temperature range from 20°C to 95°C (Figure 3.2A). The same stability test was performed for the amyloid conformation obtained after 120 h incubation (Figure 3.2B). Samples with amyloid conformation were taken from kinetic experiments. Before amyloid formation, the 129M variant shows at 20°C a spectrum that indicates higher random coil content than the 129V variant, and the spectrum only weakly changes with increasing temperature (Figure 3.2A, left). The CD spectrum before amyloid formation of the 129V variant at 20°C exhibits more initial secondary structure and changes clearly during temperature increase (Figure 3.2A, right). For both variants a rise of the CD signal at about 210 nm is observed during temperature increase, indicating an increase in random coil structure [147]. The CD spectra at 20°C of the amyloid conformation show a high content of β-sheet structure which is similar for both variants (Figure 3.2B). The amyloid structure of both variants exhibits clearly a structural change upon temperature increase. The final spectrum at 95°C resembles the secondary structure content of samples before amyloid formation, indicating reversibility of the amyloid structure for both variants at pH 2. Note that the signal of the amyloid conformation is higher for the 129V variant which hints at a larger amount of amyloid structures at the end of kinetic experiments, in agreement with the concentration left in the soluble fraction (see Figure 3.8). The lower impact of thermal denaturation on the 129M variant before amyloid formation compared to the 129V variant may explain the retarded conversion into amyloid structure observed in kinetic experiments. Despite the differences between both variants in amyloid formation kinetics, the final products present similar structure and thermal stabilities.

To investigate underlying reasons at the atomistic level for the different thermostability of the variants before amyloid formation, we performed ten replicas of 1 μs long all-atom molecular dynamics (MD) simulations for the protein fold at pH 2 of PrP(118-224) of both variants. Subsequently, we performed rigidity analyses using Constraint Network Analysis (CNA) [208] to compute the chemical potential energy averaged over the conformational ensemble, which correlates with the thermostability of proteins [208, 209]. Accordingly, the folded domain of the 129M variant is more stable (ECNA = –1003.3 kcal/mol) than the 129V variant (ECNA = -966.1 kcal/mol). To elucidate the molecular interactions that lead to this enhanced stability, we computed the differences in the neighbor stability maps (rcij,neighbor) generated by CNA [208]. rcij,neighbor indicates if a rigid contact between two residues is weaker or stronger. A contact is considered to be rigid when both residues belong to the same rigid cluster along the constraint dilution trajectory [208, 210] and, therefore, indicates the structural stability of the involved residue pair. M129 stabilizes the region located close to the substitution site. The longer side chain of methionine allows more apolar interactions with neighboring amino acids. Furthermore, methionine can form interactions with the aromatic side chain of Y163 (Figure 3.2E), further stabilizing the 129M variant [211]. M129 also has an allosteric stabilizing impact reaching over 20 Å to the C-terminal part of helix2 (Figure 3.2E). This region, especially H187, has been described to play a role in stabilizing the protein [212, 213]. Because of a pKa value of about 5, H187 is protonated at acidic but not at physiological pH [214]. The protonated form of H187

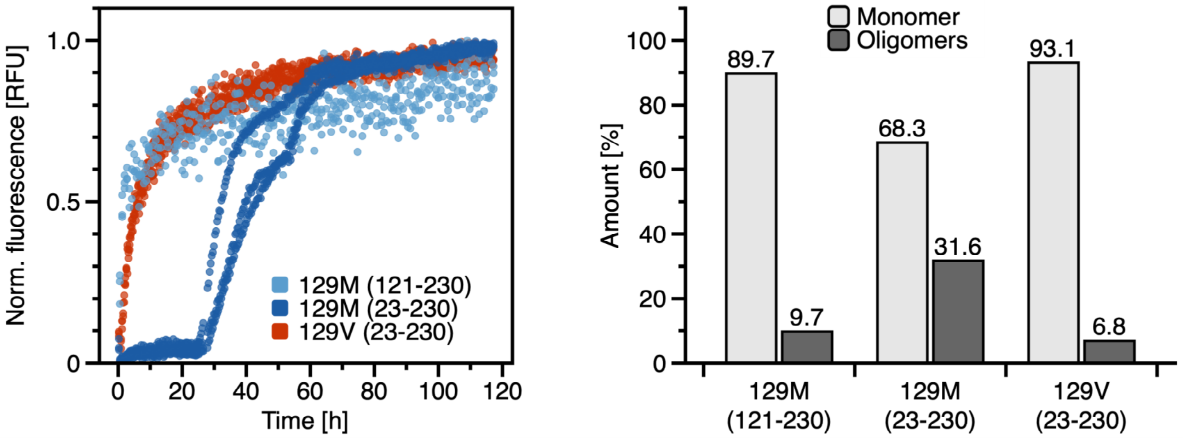

Figure 3.3: Relevance of the unstructured N-terminal region (A) Amyloid formation kinetics monitored by ThT fluorescence of the 129M variant huPrP(121-230) lacking the unstructured N-terminal region (light blue). Kinetics for full-length huPrP(23- 230) 129M variant (dark blue) and 129V variant (red) from Figure 3.1B is shown again for comparison. Kinetic data is normalized to 1 for the highest signal. 15 µM huPrP was incubated with 0.5 M GdnHCl for destabilization and initialization of amyloid formation. (B) Amount of monomer and oligomers of 129M and 129V variants huPrP(23-230) and the 129M variant huPrP(121-230). The amount is the result of integration of *c*(*s*)distributions from SV analysis of 7.5 µM huPrP without GdnHCl at pH 2 (Supporting Figure 3.9).

can disrupt the salt bridge between R156 and E196, which acts as an anchor between helix1 and helix2/helix3, by interacting with E196 [211]. Furthermore, the solvent-accessible surface area (SASA) of H187 has been reported to increase in partially unfolded structures because H187 initially forms a hydrophobic core located between helix2 and helix3 with the residues P158, F198 and M206; the protonation of H187 decreases the hydrophobicity and potentially leads to a destabilization of this hydrophobic core [213]. Thus, we analyzed the mean values of the percentage of salt bridge formation between E196 and R156 and the SASA of H187 during our MD simulations. The results show a significantly higher percentage of salt bridge formation for the 129M polymorph (48.2 ± 9.0 % , 95 % confidence interval (CI): 27.9 % - 68.5 %) in comparison to the 129V polymorph (26.0 ± 5.5 %, 95 % CI: 13.5 % - 38.5 %). The mean values for both polymorphs differ significantly (p = 0.02; unpaired t-test) (Figure 3.2C). Furthermore, the SASA of H187 is significantly decreased in the 129M polymorph (34.6 ± 1.2 Å^2 , 95 % CI: 31.8 Å^2 – 37.3 Å^2) compared to the 129V polymorph (40.7 ± 2.8 Å^2, 95 % CI 34.4 Å^2 – 47.0 Å^2) (p = 0.03; unpaired t-test) (Figure 3.2D), confirming the increased structural stability in this region for huPrP(118-224) (Figure 3.2E). The lower stability of the investigated 129V variant might favor amyloid formation by lowering energetic barriers considering the single amino acid exchange at position 129 [215].

Studies investigating the polymorphism at position 129 generally used a shorter construct of huPrP, lacking the unstructured N-terminal domain [73, 72]. To test the effect of the unstructured N-terminal domain on aggregation kinetics and oligomer formation, we compared a shorter construct of the 129M variant without the N-terminal half, huPrP(121-230), to our full-length proteins (Figure 3.3). The lack of the unstructured N-terminal domain of the 129M variant significantly alters the amyloid formation kinetics (Figure 3.3A). The shorter construct of the 129M variant does not present multiphasic, complex kinetics but shows an immediate onset of amyloid formation as already observed for the full-length 129V variant. SV experiments report a lower degree of oligomerization and a higher monomer content for huPrP(121-230) of the 129M variant compared to full-length huPrP(23-230) (Figure 3.3B and Supporting Figure 3.9). The monomer and oligomer content of the shorter 129M variant is similar to the full-length 129V variant, which agrees with the similarities found in amyloid formation kinetics. We conclude that the presence of the unstructured N-terminal region affects the structural properties of the protein, leading to significant changes in oligomerization and hence in amyloid formation kinetics.

3.6. Discussion

In summary, our study revealed clear differences in the pathway of amyloid formation at pH 2 of full-length huPrP(23-230) associated with the single Met/Val amino acid exchange at position 129, which provide insights into possible mechanisms underlying prion diseases. Additionally, we observed a significant impact of the unstructured, 98 amino acid long N-terminal region on the aggregation propensity of the 129M variant, superimposing the direct effect of the polymorphism at position 129. The deviating stability of both variants of huPrP(118-224) observed during MD simulations suggest a different unfolding behavior based on this polymorphism. We observed an initial ThT fluorescence plateau in kinetic measurements upon the addition of GdnHCl for the 129M variant. The early ThT signal supports an immediate formation of oligomers with partial binding sites for ThT, which was already reported for the 129M variant [216]. After the initial formation of aggregates, no further decrease of the soluble fraction was observed. As a consequence, the increase in ThT fluorescence leading to interim and final plateaus observed in the multi-phasic kinetics of the 129M variant originates from structural rearrangements of already existing larger oligomers. A stronger tendency for oligomerization of the 129M polymorphism was also observed in SV experiments without GdnHCl. The capability of larger oligomers to assemble into amyloid fibrils was previously shown for ovine PrP [217]. We conclude that the amyloid formation pathway for the 129M variant is different to the 129V variant and characterized by the presence of oligomeric intermediates undergoing further structural conversion. The increased population of non-native states but not yet fully amyloid structure for the 129M variant might explain differences in pathology associated with this polymorphism. Interestingly, the existence of a detectable amount of dimers was already reported to interfere with the conversion of huPrP^{C} into huPrP^{Sc} [218]. Observed s-values appropriate for dimers in SV experiments were exclusively found for the 129M variant, providing a further explanation for higher resistance to amyloid formation and more complex kinetics.

The differences in structure and global stability of huPrP^{C} as a consequence of the polymorphism at position 129 were already investigated in NMR studies [73]. It was reported that the polymorphism at position 129 in a shorter construct excluding the unstructured N-terminal domain, huPrP(90-230), neither impacts on structure nor stability. It should be noted that the polymorphism was investigated at pH 5.5 At this pH, H187 is not completely in a protonated state. It was further reported that the polymorphism might affect amyloid formation kinetics or the formation of intermediates on the pathway of conversion of huPrP^{C} into huPrP^{Sc}. The overall structure of the C-terminal globular domain of huPrP(125-228) is not affected by constructs of different lengths but a transient contact between the flexible, unstructured N-terminal region and the globular C-terminal domain was observed in NMR studies [55]. The length of the unstructured, N-terminal region affects helix2 (187-193) and helix3 (219-226) in the globular domain. Hence, the usage of full-length huPrP(23-230) leads to a more complete picture of the underlying structural rearrangements by including the complete, flexible N-terminus.

This study aimed to investigate the differences between the two variants with regard to their aggregation propensity and possible amyloid formation pathways. We concluded an oligomer-mediated pathway for the 129M variant but could only observe such behavior for the full-length variant. The described data result as a consequence of both described effects, the exchange of a single amino acid as well as the presence of the N-terminal half, however, the effect of the single amino acid exchange seems to be superimposed by the depletion of the 98 amino acid long N-terminal half. Our results emphasize the relevance of the considered full-length huPrP(23-230) construct to perceive different aggregation propensities.

3.7. Material and methods

All experiments were performed at pH 2 in 10 mM aqueous HCl.

3.7.1 Expression and purification of human prion protein

Both recombinant huPrP(23-230) variants 129M and 129V as well as the huPrP(121-230) 129M variant were expressed and purified as previously described [64]. The protein folding following this purification protocol and acidic pH was previously confirmed by NMR [64]. Final sample purity was confirmed by SDS-PAGE (Figure S1).

3.7.2 Amyloid formation kinetics

Amyloid formation kinetics of both huPrP(23-230) variants and huPrP(121-230) 129M variant were monitored by ThT fluorescence using a plate reader (BMG, Offenburg, Germany). ThT fluorescence was measured by excitation at 445 nm and detection at 485 nm. 15 µM and 20 µM huPrP with 0.5 M GdnHCl and 30 µM ThT were measured. The measurements were performed in triplicates in a 96-well plate (No. 3881, Corning) sealed with a plastic film at 37°C and continuous shaking at 300 rpm.

3.7.3 Circular dichroism spectroscopy

CD spectra of 10 M huPrP(23-230) for both variants were recorded in a Jasco J-815 (Jasco, Tokyo, Japan) spectropolarimeter at 20°C without GdnHCl and after 5 h in the presence of 0.5 M GdnHCl. Thermal stability was investigated over a temperature range from 20°C to 95°C. The thermal stability was investigated before amyloid formation of 10 µM huPrP(23-230). To investigate the thermal stability of the amyloid conformation, 100 µl were taken from amyloid formation kinetics of 20 µM huPrP(23-230) after 120 h and centrifuged at 15,000×g for 25 minutes and 20°C. The pelleted amyloid structures were dissolved in 100 µl 10 mM HCl (pH 2). A quartz glass cuvette with 1 mm path length was used. Spectra were measured at 50 nm/min with 2 nm bandwidth and 4 s digital integration time (D.I.T.). Spectral resolution was 1 nm and temperature resolution was 5°C. The temperature was increased with 2°C/min and 30 s waiting time before measurement. Ten accumulations were measured for each spectrum.

3.7.4 Analytical ultracentrifugation

Sedimentation velocity (SV) experiments were performed in an analytical ultracentrifuge Proteome Lab XL- A (Beckman-Coulter, Brea, US). Experiments included 7.5 µM huPrP. Samples were measured in standard double sector cells (Titanium) with an optical path length of 12 mm using an An-60Ti rotor. Temperature was set to 20°C. The speed was 60,000 rpm corresponding to about 260,000×g. Data analysis was performed using a continuous distribution Lamm equation model, $c(s)$, implemented in the software Sedfit (version 16p35) [219].

3.7.5 Molecular dynamics simulations

Structural information for PrP(118-224) 129M was taken from PDB entry 4N9O [220]. For the 129V polymorph, the amino acid at position 129 was mutated to valine using MOE, version 2019.01 [221]. We selected the energetically most favored rotamer and subsequently minimized the side chain; both polymorphs were protonated according to pH 2, and the N- and C termini were capped with NME and ACE, respectively, using MOE, version 2019.01 [221]. With a predicted pKa value of 2.09, E196 can be protonated or deprotonated at pH 2 [222]. As E196 forms a salt bridge with R156 in our starting structure, which stabilizes a negative charge at E196, it is likely that E196 is deprotonated in the starting structure. The polymorphs were then neutralized using Cl^- as counter ions and solvated in an octahedral box of OPC water [223] with a minimal water shell of 12 Å around the protein. The Amber package of MD simulation software [224] and the ff19SB force field [225] were used to perform MD simulations. For further details of our simulation methods, see supporting information and Figure 3.11.

3.7.6 Structural analyses

To ensure that the starting structures of both polymorphs do not influence the results, we removed the first 500 ns of MD simulations prior to the analyses. Every 5 ns, a frame was extracted from the trajectories using CPPTRAJ [226], and counter ions and water molecules were stripped. From the protein conformations, neighbor stability maps rcij,neighbour were calculated using CNA [208]. CNA is a software package that functions as front- and backend for the FIRST software and helps to analyze structural features critical for protein stability; neighbor stability maps are derived from all extracted trajectories along the simulation and contain information about the persistence of rigid contacts between pairs of residues [227, 208]. In order to exclude pairs of structurally non-neighboring residues, only interactions were considered in rcij,neighbour where at least one of the pairs of heavy atoms of the residue pair R(i,j) is separated by less than 5 Å. The chemical potential energy ECNA, a measure for thermostability, was calculated according to equation 3.1 as done previously [209].

$$E_{C,N,A} = \sum_{i}^{n} \sum_{j>i}^{n} rc_{ij,neighbor} \tag{3.1}$$

The distance between the carboxy oxygens of E196 and the side chain nitrogen atoms of R156 was calculated using the nativecontacts mindist command as implemented in CPPTRAJ [226]. We consider a salt bridge formed if the distance between respective charged heavy atoms is <4 Å [228]. The SASA of H187 was analyzed using the surf command as implemented in CPPTRAJ [226]. We calculated the one-sided t-test for both measurements with the null hypothesis that the values of the two stability-indicating measurements are in favor of the more stable 129M polymorph.

3.8. Supporting information

3.8.1 Supporting methods

Molecular dynamics simulations: Molecular dynamics simulations were performed using the ”Particle Mesh Ewald” method to consider long-range interactions; the SHAKE algorithm was applied to bonds involving hydrogen atoms [229]. The time step during thermalization and equilibration was set to 2 fs with a direct-space, non-bonded cutoff of 9.0 Å; the time step during the production runs was set to 4 fs as hydrogen mass repartitioning was used with a direct-space, non-bonded cutoff off 8.0 Å [230]. First, 102,500 steps of steepest descent and conjugate gradient minimization were performed; during 2,500, 50,000, and 50,000 steps positional harmonic restraints with force constants of 5 kcal×mol^{-1}×Å^{-2}, 1 kcal×mol^{-1}×Å^{-2}, and 0 kcal×mol^{-1}×Å^{-2}, respectively, were applied to the protein atoms. Then, 50 ps of NVT-MD (constant number of particles, volume, and temperature) were performed to heat the system to 100 K, followed by 250 ps of NPT-MD (constant number of particles, volume, and temperature) simulations to heat the system to 300 K and to adjust the density of the simulation box to a pressure of 1 atm. During these steps, a harmonic potential with a force constant of 1 kcal×mol^{-1}×Å^{-2} was applied to protein atoms. Thereafter, 300 ps of NVT-MD simulations were conducted. During the first 250 ps of this step, the harmonic restraints were gradually reduced to zero. Then, ten independent replica of MD simulation production runs of 1 µs length were performed for each polymorph. The starting temperature of each run was varied by a fraction of a Kelvin.

To ensure that the dihedral angle of the mutated side chain does not impact the outcome of the MD simulations, we analyzed the dihedral angle between the planes defined by N, CA, CB and CA, CB, CG1 during the MD simulations using CPPTRAJ [226] (Figure 3.11). As all favored dihedral angles are found in this analysis (180°, -60°, and 60°) and there are frequent exchanges between these states, indicating that the side-chain of V129 is in equilibrium, the starting conformation of valine at position 129 should not influence the results. To be noted, the MD simulations do not include the glycosylation of the protein, as all experiments were performed with unglycosylated huPrP.

Uv-absorbance measurement: Uv absorbance of soluble fraction was measured for both huPrP(23-230) variants during amyloid formation using the UV-1900i UV-VIS-Spectrophotometer (Shimadzu, Kyōto, Japan). 15 µM huPrP with 0.5 M GdnHCl were used. Samples were incubated in 1.5 ml Lobind Eppendorf tubes, at 37°C and continuous shaking at 300 rpm. After 1 h, 5 h, 19 h, 55 h, 96 h and 120 h, 100 µl was taken and centrifuged (30 minutes, 15,000×g, 25°C). The supernatant was used to measure the remaining monomer and small oligomer content. The measurement was performed in duplicates in a quartz glass cuvette with 1 mm path length.

3.8.2 Supporting results

Different protein concentration and GdnHCl concentrations reveal distinct amyloid kinetics Different conditions were investigated for the amyloid formation kinetics. Supporting Figure 3.5 shows a concentration series of different GdnHCl concentrations with 15 µM of huPrP(23-230) 129M variant. These results indicate that a certain amount of GdnHCl is needed for sufficient destabilization and initialization of amyloid formation. The amount should not be too high to enable seed formation. Additionally, a concentration series with relatively low concentrations of both variants was established with a constant ratio of GdnHCl (Supporting Figure 3.6). Supporting Figure 3.7 confirms the importance of a certain huPrP/GdnHCl ratio for the 129M variant, as the lowest protein concentration tested with the highest applied GdnHCl concentration shows a significantly delayed fluorescence increase. For the highest protein concentration, the amount of GdnHCl alters the fluorescence signal of the initial plateau as well as the time of increase and duration of the interim and final plateau.

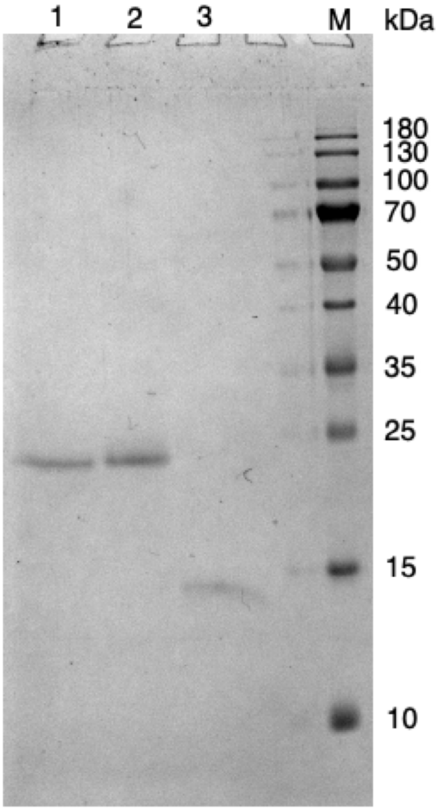

Figure 3.4: Final purity of huPrP constructs Coomassie stained 15 % Tris/Glycine SDS-PAGE of 3 µM huPrP. 1, huPrP(23-230) 129V; 2, huPrP(23-230) 129M; 3, huPrP(121-230) 129M; M, marker protein.

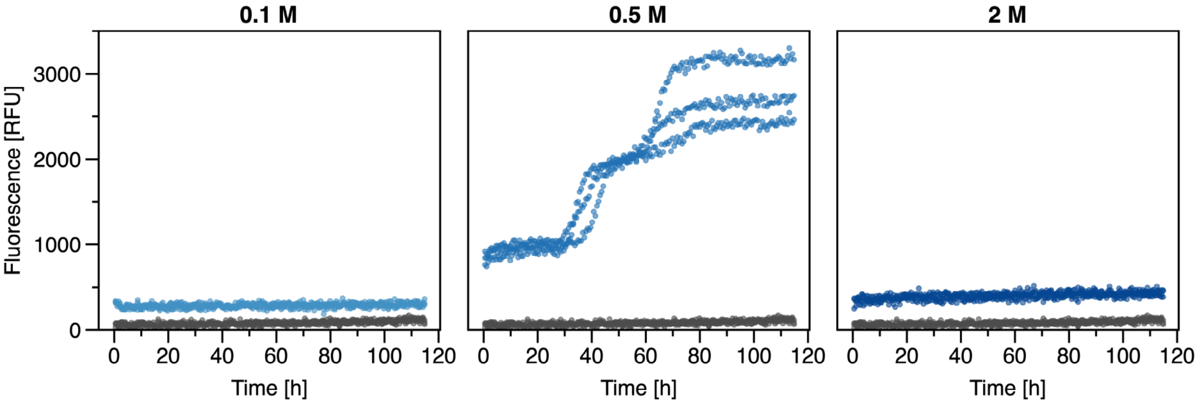

Figure 3.5: Destabilization of huPrP Amyloid formation kinetics monitored by ThT fluorescence of 15 µM huPrP(23-230) 129M variant in the presence of different GdnHCl concentrations at pH 2. huPrP(23-230) 129M without GdnHCl shows no amyloid formation (grey).

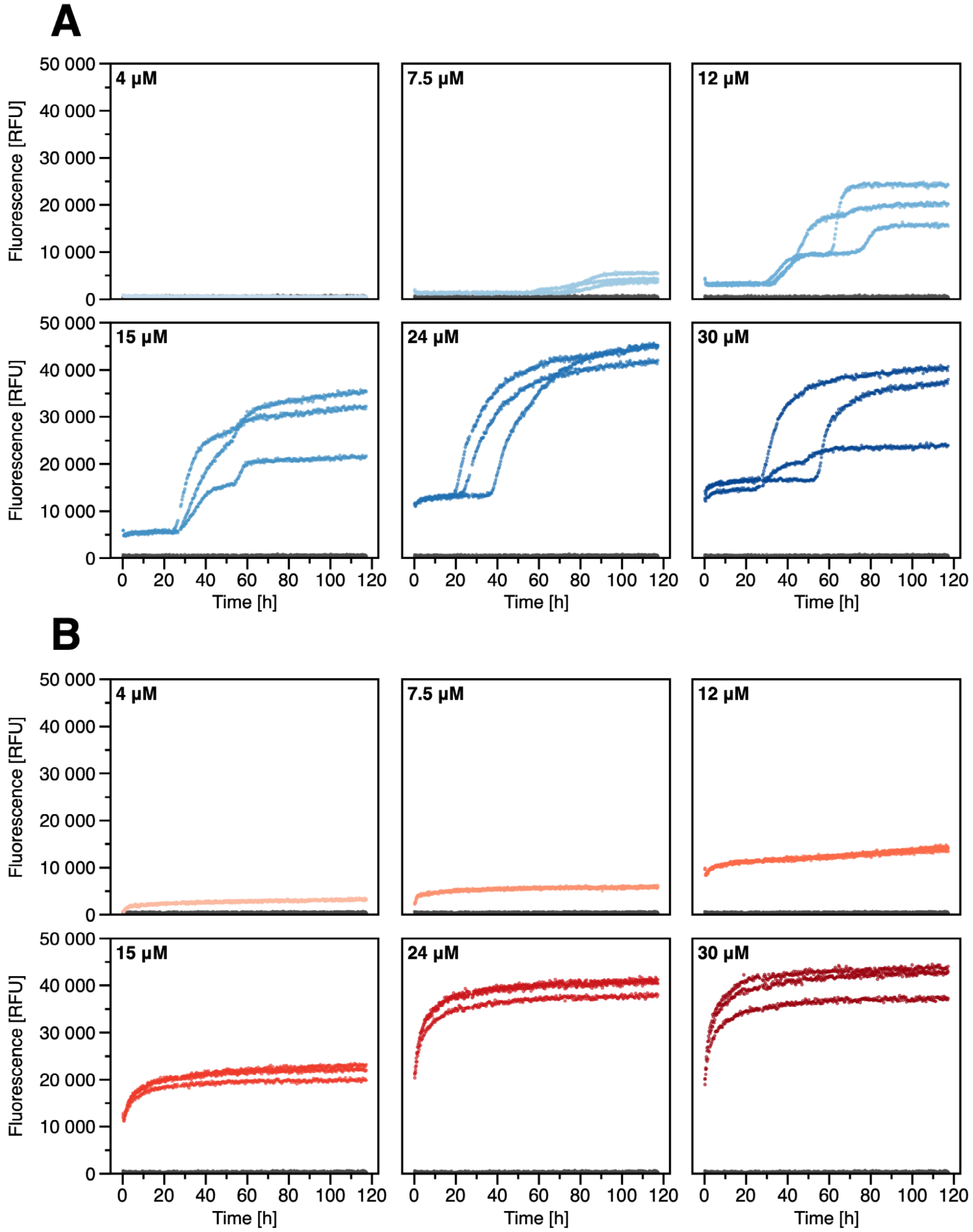

Figure 3.6: Concentration series of huPrP (A) Amyloid formation kinetics monitored by ThT fluorescence of different huPrP(23-230) concentrations for the 129M variant and (B) 129V variant at pH 2. The ratio between protein and GdnHCl is constant at 1 to 33,333. HuPrP(23-230) without GdnHCl shows no amyloid formation (grey).

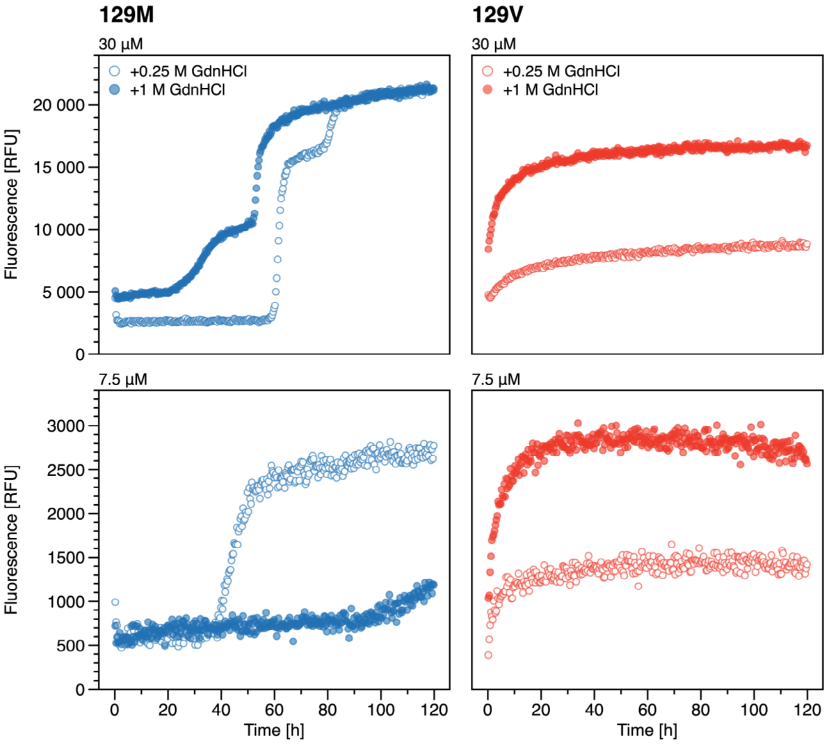

Figure 3.7: Comparison of different huPrP and GdnHCl concentrations Amyloid formation kinetics monitored by ThT fluorescence of 7.5 µand 30 µM huPrP(23-230) for both variants in the presence of 0.25 M and 1 M GdnHCl at pH 2.

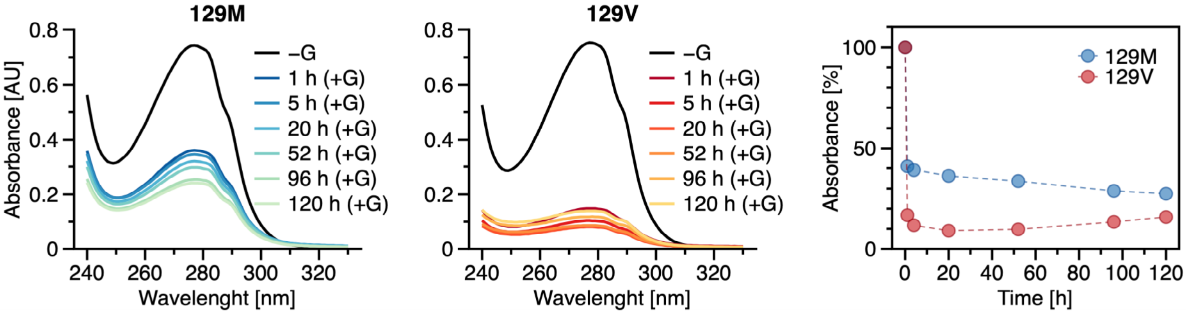

Figure 3.8: Soluble fraction during amyloid formation Absorbance spectra of 15 µM huPrP (23-230) 129M and 129V variant at pH 2. Spectra were measured before amyloid formation without GdnHCl and after 1 h, 5 h, 19 h, 55 h, 96 h and 120 h during amyloid formation in the presence of 0.5 M GdnHCl. Left and middle graphs show the absorbance plotted against the wavelengths (in nm) for the 129M and the 129V variant, respectively. Right graph represents the relative absorbance (in %) plotted against the time (in h).

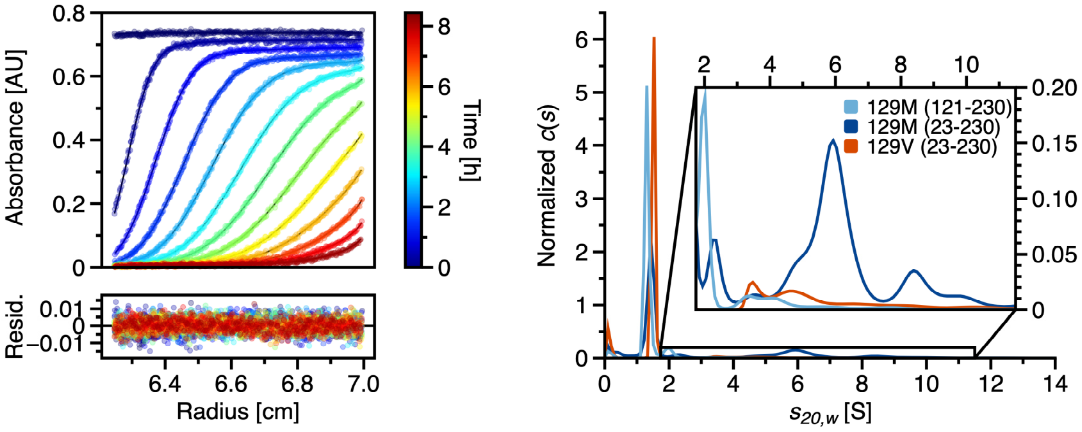

Figure 3.9: Impact of the unstructured N-terminal region on oligomerization (A) Comparison of results from SV analysis of 7.5 µM of the 129M variant huPrP(121-230) (light blue) and huPrP(23-230) (dark blue) and the 129V variant huPrP(23-230) (orange) at pH 2. Raw data of the 129M variant huPrP(121-230) with fitted Lamm-equation solutions from *c*(*s*) model are color-coded for the duration of sedimentation. (B) The result of data fitting is an *s*-value distribution. The distributions of huPrP(23-230) for both variants are shown for comparison.

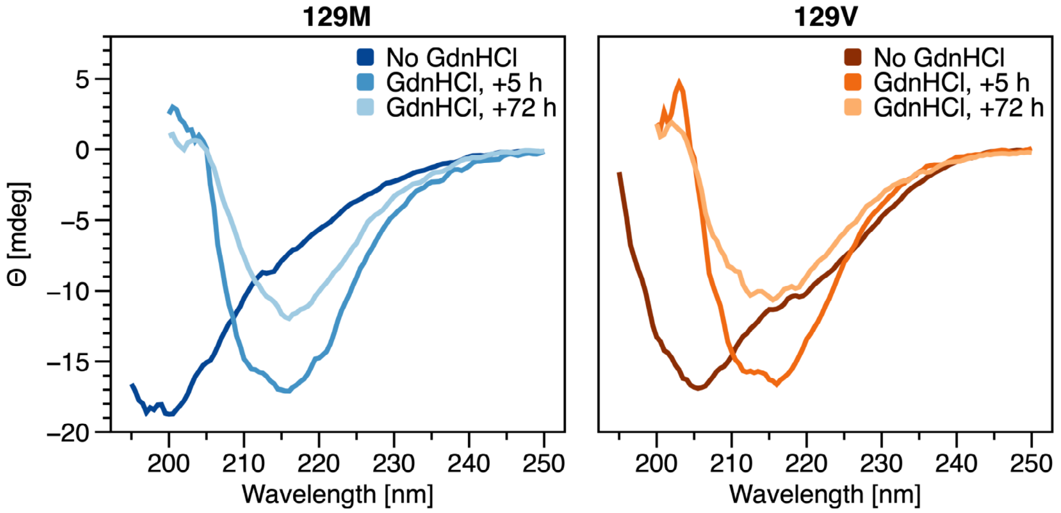

Figure 3.10: Secondary structure content before and during amyloid formation CD spectra of 10 µM huPrP(23-230) 129M and 129V variant at pH 2. Spectra were measured before amyloid formation without GdnHCl and after 5 and 72 h during amyloid formation in the presence of 0.5 M GdnHCl.

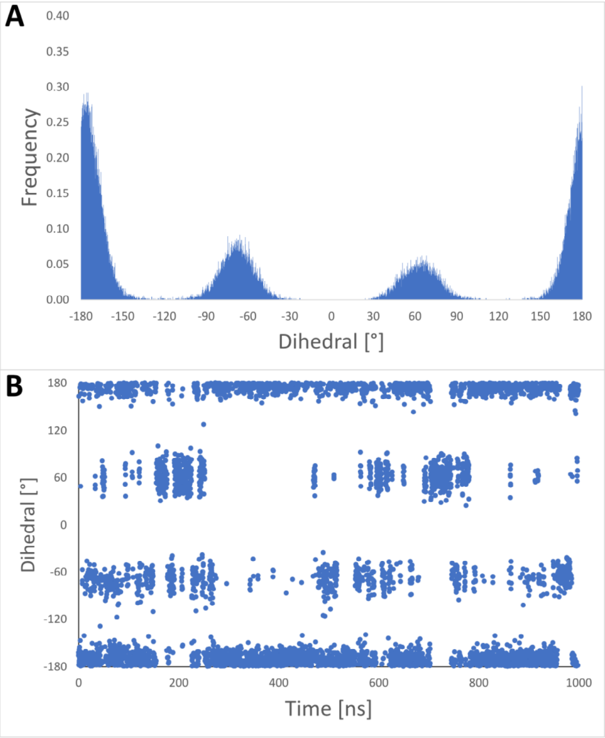

Figure 3.11: Dihedral angles (A) Frequency distribution of dihedral angles in all replicas and (B) appearance of the dihedral angle over time during one replica; the dihedral angle was determined between the planes spanned by N, CA, CB and CA, CB, CG1 during MD simulations.

4

CONCLUSION & DISCUSSION

The increasing interest in oligomeric assemblies of the peptide Aβ42 had driven earlier studies, identifying penta- to hexamers as the smallest detectable species in solution and as potential building blocks for larger assemblies [231]. Additionally, a distribution of larger oligomers in the range of approximately 4 S to 15 S had been reported, including prominent species with sizes of 12-mers and 18-mers [232]. The cytotoxic effect of oligomers within this size range had been demonstrated as well as the ability to bind to an oligomer eliminating D-enantiomeric peptide [233]. However, at that time, it remained unclear if and how these different oligomeric species contribute to the process of amyloid formation. Interaction of oligomers formed by the Aβ peptide and huPrP had already been studied [64], but details on the amyloid formation process of full-length huPrP were still elusive.

In this work, different oligomeric intermediates of the Aβ peptide were separated by SV experiments so that their kinetics could be investigated during the amyloid formation process. By complementing SV experiments with ThT kinetics, CD measurements, and AFM imaging, it was possible to characterize three different oligomeric species and to infer their contribution to amyloid formation. It was demonstrated that the rigor of SV experiments is sufficient to compare different oligomeric species of variants of the Aβ peptide in detail to support their contribution to amyloid formation as well as to utilize commonly used fluorescent dyes to probe oligomers.

SV experiments usually take several hours, so it was not obvious that this technique is appropriate to study an aggregating system. The analysis of sedimentation profiles requires the $c(s)$ model to yield a continuous distribution of sedimentation coefficients. This model relies on non-interacting particles or a slow reaction relative to the duration of sedimentation. The major concern for studying Aβ oligomers during the amyloid formation process therefore was a rapidly changing system in the time course of amyloid growth during sedimentation. The kinetic events leading to rapid amyloid growth are elongation of existing fibrils and secondary processes such as secondary nucleation on the surface of fibrils or fibril fragmentation, which creates new ends for further growth [99]. All of these processes, which lead to a dramatic increase in amyloid content, are based on the existence of amyloid fibrils. Applying a high centrifugal force ($\sim$260,000 $\times$g) promotes rapid sedimentation of large aggregates, so that fibrillar species already depleted from the solution before the centrifuge reached the final speed. Consequently, processes such as secondary nucleation and fragmentation that may interfere with the analysis of oligomeric intermediates, are largely absent during the measurement. It should be noted that all molecular events are expected to contribute to the aggregation process during incubation in between measurements. In fact, primary nucleation during SV measurement is still a possible event, but due to the high energy barrier, this is also expected to be largely absent and a rare event [42]. The complete duration of sedimentation was approximately 8 h, but the majority of oligomers are sedimented within the first 90 min. Oligomers are generally considered to be metastable assemblies that are in equilibrium with smaller species such as monomers. In SV experiments, the entire sedimentation process of oligomers takes place in the presence of such smaller species, maintaining the equilibrium situation.

Given the fact that oligomers are dynamic in nature and that spontaneous nucleation might initiate amyloid formation, the accuracy with which the oligomers could be detected at different stages of the amyloid formation process, was unexpected. The process of amyloid formation takes about 18 h to enter the rapid growth phase, i.e., the time required for the formation of a nucleus capable of growth to form amyloid fibrils. Experiments were performed in triplicate at six separate time points, corresponding to 18 independent aggregation processes that were observed. All of these measurements yielded consistent ThT fluorescence and fractions of different species based on SV experiments. This supports the existence of a reproducible amyloid formation pathway with a distinct mechanism of nucleation. We observe an immediate formation of oligomeric intermediates, including small species (LMWOs) and large species (HMWOs), already present at the first time point (1 h). The LMWOs include a species that was already described as a penta to hexamer [231] and a smaller potentially trimeric to tetrameric species. Small oligomers of similar size for Aβ42 were described before using gel electrophoresis [234, 235], but uncertainties about the existence of these species in solution were raised [236]. The diffusible nature of these small oligomers could cause extensive neurotoxicity in the brain. [235]. In this work, two LMWOs were isolated in solution by SV experiments, reporting on the existence of small, diffusible oligomers and their kinetics in a matrix-free approach. Since no amyloid growth is observed within the first 18 h, we infer that none of the early oligomers detected represents a species with the capability to recruit monomers and occupy a energetically favored state. During the lag phase of amyloid fibril formation, both LMWOs were determined with constant s-values and concentrations, indicating no considerable change in mass or shape. In contrast, the kinetics of HMWOs were observed with an increase in the weighted average s-value, which was accompanied by a slight increase in concentration. Such growth could be described as a consolidation process, which involves an increase in mass and potentially in shape. The increasing mass over time could be related to a phenomenon termed Ostwald ripening, which is known for crystals, sol particles, or emulsions [237, 238]. In protein solutions, it was already described that clusters increase in size, described by the laws of Ostwald ripening, which renders such clusters as nucleation sites for ordered solids [187]. The composition of a heterogeneous mixture changes as small particles dissociate and redeposit on larger particles. Since individual particles are less stable at the surface than within a larger assembly, the growth of these aggregates is a spontaneous, thermodynamically driven process. The interaction of monomers to form HMWOs could be primarily driven by hydrophobic interactions. This inference is supported by the lower hydrophobicity of Aβ40 and Aβ42 M35^{ox}, both of which were presented in this study with a lower amount of HMWOs. Aβ40 lacks two C-terminal hydrophobic amino acids. Oxidation of M35 converts an apolar amino acid to a polar one [239]. It is known that both, Aβ40 and Aβ42 M35^{ox}, exhibit delayed amyloid formation kinetics as well as reduced toxicity compared with Aβ42 [38, 36, 39]. Interestingly, all three variants of the Aβ peptide have LMWOs at similar s-values. From this comparison of Aβ variants we conclude that HMWOs are key intermediates for the amyloid formation process as their size and concentration correlates with the duration of amyloid formation. HMWOs present increased local monomer concentration and the process of consolidation facilitates inter-molecular interactions of monomeric units, lowering the energetic barrier for nucleus formation. Hence, in this study, we infer that the population of HMWOs is an on-pathway intermediate as it constitutes centers for the formation of a growth-competent nucleus. CD measurements showed a small decrease in random coil structure and an increase in the β-sheet fraction in the heterogeneous mixture during the lag phase of fibril formation. This suggests β-sheet structure within the oligomers, which is confirmed by a small positive ThT fluorescence signal during the first 18 h of kinetics. Nevertheless, the secondary structure of the early oligomeric intermediates apparently does not meet the requirements for amyloid fibril formation, i.e., a cross β-sheet conformation that is passed along other monomeric units. An aggregation mechanism involving intermediates as crucial components for nucleus formation resembles the two-step nucleation mechanism [98] observed for crystallization [97] and was described previously for Aβ[95]. The previous approach to quantify such oligomers of Aβ42 during the amyloid formation process involved centrifugation, chromatography and liquid scintillation counting of radio-labeled species or mass spectrometry. This study presents SV as an orthogonal technique separating and analyzing oligomer quantities as well as the kinetics of separated species during the amyloid formation process. The Aβ concentration in this study are above physiological level, but HMWOs of similar size were detected immunologically at physiological Aβ42 concentrations (1-20 nM), with a 48-mer being the prominent species [191]. In the same study, no comparable oligomerization was observed for Aβ40 in agreement with the lower concentrations of HMWOs determined for Aβ40 in this work. Whether the heterogeneity within the group of HMWOs is only due to size differences or is also related to differences in structure is not yet fully understood. We approached this question by using a series of fluorescent dyes with different scaffolds and charges in SV experiments to isolate signals from different species within the group of HMWOs. Similar to ThT, we expected differences in the specificity of the interaction between the different dyes and the different structure of the oligomers. All dyes showed a similar distribution of HMWOs, indicating no preferential interaction. Therefore, we concluded that the heterogeneous group of HMWOs represents binding sites for each dye tested, with a common structural feature responsible for the interaction.

In contrast to the Aβ peptide, huPrP is not an intrinsically disordered protein but consists of a globular C-terminal domain and an unstructured N-terminal region that spans almost half of the protein. Consequently, conversion of full-length huPrP to amyloid requires destabilization, which was achieved in this work by acidic pH and addition of the denaturant GdnHCl. In this work, we examined the amyloid formation behavior of two variants of the naturally occurring polymorphism at position 129 of full-length huPrP and described differences in oligomerization and amyloid formation kinetics, which presumably relate to different pathologies associated with this polymorphism.

It was demonstrated by SV experiments that the 129M variant is more prone to oligomerization and ThT kinetics revealed a multiphasic aggregation behavior. In contrast, we found the 129V variant with a lower tendency to form oligomers, accompanied with fast ThT kinetics, progressing directly into the final plateau. As no amyloid formation was observed at acidic pH without further destabilization by GdnHCl, we concluded that the conformation of huPrP remains relatively stable under these conditions. As monomeric protein is predominant for the 129V variant, addition of GdnHCl could mainly lead to a destabilized monomer conformation. We infer that amyloid formation for the 129V directly starts from a destabilized monomer as the growth-competent species. Considering the increased amount of oligomers for the 129M variant, GdnHCl could destabilize the monomer conformation as well as interact with several oligomeric species. The interaction mechanism of GdnHCl and proteins is still poorly understood. It is suggested that the interaction involves a two-stage mechanism of unfolding [240]. In a first step, GdnHCl can interact with the protein surface, displacing water molecules within the first solvation shell. In a second step, denaturant and water molecules can penetrate and solvate the hydrophobic protein core, leading to structural disruption. The first step of this interaction mechanism creates a dry globule-like intermediate with partial disruption of side-chain packing interactions, but without solvation of the hydrophobic core. It should be noted that a relatively small amount of only 0.5 M GdnHCl was used in this study to achieve partial unfolding without preventing amyloid formation. It remains unclear, how this amount of denaturant interacts with the monomeric and oligomeric fraction of the protein solution and whether a partially unfolded intermediate is built on the pathway of amyloid formation. Based on the stronger tendency to form oligomers and the interim plateaus of ThT kinetics, we infer that the 129M forms amyloid via oligomeric intermediates. The question remained as to whether the initially formed intermediates first dissociate again and monomer is then consumed upon amyloid growth, similar to the proposed mechanism for the 129V variant, or whether these intermediates undergo structural conversion, converting into the final amyloid structure. It was shown that initially formed aggregates upon addition of GdnHCl do not dissociate during the amyloid formation process. Consequently, we assume that the intermediate plateaus for the 129M variant are due to different states of oligomeric intermediates undergoing structural conversion which leads to increased ThT binding capacity and consumption of monomers. The increased tendency of the 129M variant to form β-sheet rich oligomers was already reported [216] as well as the capability of ovine PrP oligomers to assemble into amyloid [217]. A comparison of the differences in oligomer distributions between the two variants of huPrP in relation to amyloid formation behavior has been lacking.

It is known that the polymorphism 129 of huPrP relates to different pathologies. vCJD was only diagnosed in individuals homozygous for methionine at position 129 [197] and iatrogenic CJD was predominantly found in homozygotes for valine at position 129 [241, 242, 243]. Furthermore, this polymorphism affects the generation of strain-specific PrP^{Sc} conformers and thus supposedly the phenotype of human prion diseases [73]. The phenotypic impact of polymorphism at position 129 is seen in the inherited prion disease FFI, which requires another mutation (D178N) and the presence of the 129M variant, while the phenotype of CJD is developed in the presence of the 129V variant [244]. The most abundant type of prion disease in humans is sCJD and a majority of cases with homozygosity for polymorphism at position 129 was observed [245]. Even though no significant differences was found between the number of patients homozygous for 129M or 129V, homozygous 129V patients were on average five years younger. The differences observed in the aggregation behavior in this work could relate to differences found in the pathology of homozygous prion disease patients. So far, in literature no structural differences were observed between both variants of the polymorphism at position 129 in studies using shorter constructs of huPrP [73]. It was inferred that the effect of different variants is mediated through intermediates or the kinetics of the conversion of PrP into the disease related conformation. In this work, we present significant differences in the formation of oligomeric species and their impact on amyloid formation kinetics. Surprisingly, we could only determine such differences for studies on full-length huPrP. Experiments involving a shorter construct of the 129M variant, lacking the unstructured N-terminal region, exhibit amyloid formation kinetics without interim plateaus, but rather a direct increase into the final plateau, indistinguishable from full-length 129V kinetics. Consistently, SV experiments reveal a smaller amount and average size of oligomers for the shorter 129M variant, similar to the full-length 129V variant. From these results, we infer that the differences observed between the two huPrP variants become apparent only when the full-length protein is examined. It seems that the effect of the single amino acid exchange at position 129 is superimposed by the depletion of the 98 amino acid long N-terminal half. The presence of the unstructured N-terminal region leads to pronounced oligomerization of the 129M variant, whereas the full-length 129V variants, including the N-terminal region, lacks the majority of oligomers. It was suggested in NMR studies before that the flexible N-terminal tail could interact with the globular C-terminal domain and affect its folding [55]. We infer in this study that the N-terminal region affects oligomerization and amyloid formation by interaction with the C-terminal domain to an extend depending on the polymorphism at position 129. As huPrP *in vivo* contains two glycosylation sites and a glycolipid anchor for membrane attachment, further studies in near-physiological conditions, including post-translational modifications, are needed to better characterize the aggregation behavior of the protein variants.

In summary, different pathways of amyloid formation were investigated, focusing on the role of oligomer formation. Aβ peptides as IDPs spontaneously aggregate to form amyloid at physiological pH. A variety of oligomers are formed immediately and exhibit distinct kinetics during amyloid fibril formation. huPrP contains secondary structure elements in the C-terminal domain that need be destabilized to enable aggregation, leading to amyloid formation. Aggregation kinetics involve intermediate species for the full-length 129M variant, including larger oligomers that presumably undergo structural conversion to reach the final amyloid conformation. Although amyloid formation of huPrP needs to be initiated by the addition of GdnHCl, pronounced oligomerization of the full-length 129M variant is already present upon solubilization at acidic pH prior to amyloid formation. The role of oligomer formation differs between Aβ peptide and huPrP, as Aβ oligomers could be observed over a relatively long period of time during the aggregation process and different species could be isolated by SV experiments. During the lag time of amyloid fibril formation, oligomers are observed, and the potential contribution to nucleus formation could be investigated. For huPrP, the oligomeric intermediates are large compared to Aβ oligomers after addition of GdnHCl, resulting in increased ThT fluorescence that either progresses directly to the final plateau for the full-length 129V variant or rests at an initial and interim plateaus for the full-length 129M variant. A lag phase for amyloid formation similar to Aβ42 aggregation with low ThT signal could not be observed for huPrP because the rapidly formed oligomers are large and do not dissociate before amyloid formation kinetics proceed. In contrast, Aβ42 oligomers apparently dissociate as soon as a growth-competent species takes over the aggregation process by rapidly consuming monomers. However, these HMWOs still contribute to the mechanism of amyloid formation by lowering the energetic barrier for nucleus formation, thus constituting nucleation sites. Therefore, we classified HMWOs as on-pathway oligomeric intermediates. Intermediates of huPrP appear to be what is conventionally assumed as an on-pathway intermediate, which is a species that converts to the final amyloid structure.

These oligomers described in this study could be potential target of therapeutics to interfere with the amyloid formation process or eliminate potentially toxic species. The toxicity of distinct species, characterized in this study, need to be investigated. For future studies, AUC could be utilized to study oligomerization of other disease related proteins like α-Synuclein or Tau protein. The functional role of huPrP^C is of genereal interest and a number of possible interacting proteins have been suggested [246]. The interaction between huPrP^C and Aβ oligomers was reported as a promising target that mediates toxicity [64, 247, 62]. With respect to the described differences in aggregation behavior of the two variants of huPrP and the differences in oligomerization of variants of the Aβ peptide, interaction studies using SV experiments could yield further details to the interaction mechanism. Another promising aspect is the investigation of the highly protective 129V variant, which lacks investigation on oligomerization and amyloid formation behavior so far [72]. It was reported that the single amino acid exchange G127V confers resistance to prion disease in a homozygous mouse model [248].

5

LITERATURE

[1] Iadanza MG, Jackson MP, Hewitt EW, Ranson NA, Radford SE (2018) A new era for understanding amyloid structures and disease. Nature Reviews Molecular Cell Biology 19(12):755–773

[2] Virchow R (1855) Zur cellulose-frage. Archiv für pathologische Anatomie und Physiologie und für klinische Medicin 8(1):140–144

[3] Friedreich N, Kekulé A (1859) Zur amyloidfrage. Archiv für pathologische Anatomie und Physiologie und für klinische Medicin 16(1):50–65

[4] Benditt E, Eriksen N, Hermodson M, Ericsson L (1971) The major proteins of human and monkey amyloid substance: common properties including unusual n-terminal amino acid sequences. FEBS letters 19(2):169–173

[5] Glenner G, Ein D, Eanes E, Bladen H, Terry W, Page D (1971) Creation of" amyloid" fibrils from bence jones proteins in vitro. Science 174(4010):712–714

[6] Costa PP, Figueira AS, Bravo FR (1978) Amyloid fibril protein related to prealbumin in familial amyloidotic polyneuropathy. Proceedings of the National Academy of Sciences 75(9):4499–4503

[7] Morris KL, Serpell LC (2012) X-ray fibre diffraction studies of amyloid fibrils. In: Amyloid Proteins, Springer, pp 121–135

[8] Sawaya MR, Sambashivan S, Nelson R, Ivanova MI, Sievers SA, Apostol MI, Thompson MJ, Balbirnie M, Wiltzius JJ, McFarlane HT, et al. (2007) Atomic structures of amyloid cross-β spines reveal varied steric zippers. Nature 447(7143):453–457

[9] Colvin MT, Silvers R, Frohm B, Su Y, Linse S, Griffin RG (2015) High resolution structural characterization of aβ42 amyloid fibrils by magic angle spinning nmr. Journal of the American Chemical Society 137(23):7509–7518

[10] Fändrich M, Meinhardt J, Grigorieff N (2009) Structural polymorphism of alzheimer aβ and other amyloid fibrils. Prion 3(2):89–93

[11] Gremer L, Schölzel D, Schenk C, Reinartz E, Labahn J, Ravelli RB, Tusche M, Lopez-Iglesias C, Hoyer W, Heise H, et al. (2017) Fibril structure of amyloid-β (1–42) by cryo-electron microscopy. Science 358(6359):116–119

[12] Fitzpatrick AW, Debelouchina GT, Bayro MJ, Clare DK, Caporini MA, Bajaj VS, Jaroniec CP, Wang L, Ladizhansky V, Müller SA, et al. (2013) Atomic structure and hierarchical assembly of a cross-β amyloid fibril. Proceedings of the National Academy of Sciences 110(14):5468–5473

[13] Chiti F, Dobson CM, et al. (2006) Protein misfolding, functional amyloid, and human disease. Annual review of biochemistry 75(1):333–366

[14] Chapman MR, Robinson LS, Pinkner JS, Roth R, Heuser J, Hammar M, Normark S, Hultgren SJ (2002) Role of escherichia coli curli operons in directing amyloid fiber formation. Science 295(5556):851–855

[15] Fowler DM, Koulov AV, Alory-Jost C, Marks MS, Balch WE, Kelly JW (2006) Functional amyloid formation within mammalian tissue. PLoS biology 4(1):e6

[16] Lundmark K, Westermark GT, Olsén A, Westermark P (2005) Protein fibrils in nature can enhance amyloid protein a amyloidosis in mice: Cross-seeding as a disease mechanism. Proceedings of the National Academy of Sciences 102(17):6098–6102

[17] Legname G, Baskakov IV, Nguyen HOB, Riesner D, Cohen FE, DeArmond SJ, Prusiner SB (2004) Synthetic mammalian prions. Science 305(5684):673–676

[18] Nilsson MR (2004) Techniques to study amyloid fibril formation in vitro. Methods 34(1):151–160

[19] Serpell LC, Sunde M, Benson MD, Tennent GA, Pepys MB, Fraser PE (2000) The protofilament substructure of amyloid fibrils. Journal of molecular biology 300(5):1033–1039

[20] Moran SD, Zanni MT (2014) How to get insight into amyloid structure and formation from infrared spectroscopy. The journal of physical chemistry letters 5(11):1984–1993

[21] Harada T, Kuroda R (2011) Cd measurements of β-amyloid (1–40) and (1–42) in the condensed phase. Biopolymers 95(2):127–134

[22] Puchtler H, Sweat F, Levine M (1962) On the binding of congo red by amyloid. Journal of Histochemistry & Cytochemistry 10(3):355–364

[23] Khurana R, Uversky VN, Nielsen L, Fink AL (2001) Is congo red an amyloid-specific dye? Journal of Biological Chemistry 276(25):22715–22721

[24] Bousset L, Redeker V, Decottignies P, Dubois S, Le Maréchal P, Melki R (2004) Structural characterization of the fibrillar form of the yeast saccharomyces cerevisiae prion ure2p. Biochemistry 43(17):5022–5032

[25] Biancalana M, Koide S (2010) Molecular mechanism of thioflavin-t binding to amyloid fibrils. Biochimica et Biophysica Acta (BBA)-Proteins and Proteomics 1804(7):1405–1412

[26] Naiki H, Higuchi K, Hosokawa M, Takeda T (1989) Fluorometric determination of amyloid fibrils in vitro using the fluorescent dye, thioflavine t. Analytical biochemistry 177(2):244–249

[27] Levine III H (1993) Thioflavine t interaction with synthetic alzheimer's disease β-amyloid peptides: Detection of amyloid aggregation in solution. Protein Science 2(3):404–410

[28] Groenning M (2010) Binding mode of thioflavin t and other molecular probes in the context of amyloid fibrils—current status. Journal of chemical biology 3(1):1–18

[29] Patterson C (2018) World alzheimer report 2018. Alzheimer's Disease International

[30] Tejada-Vera B (2013) Mortality from Alzheimer's disease in the United States: data for 2000 and 2010. 116, US Department of Health and Human Services, Centers for Disease Control and …

[31] Alzheimer A (1906) Uber einen eigenartigen schweren er krankungsprozeb der hirnrinde. Neurologisches Centralblatt 23:1129–1136

[32] Sloane PD, Zimmerman S, Suchindran C, Reed P, Wang L, Boustani M, Sudha S (2002) The public health impact of alzheimer's disease, 2000–2050: potential implication of treatment advances. Annual review of public health 23(1):213–231

[33] Hebert LE, Scherr PA, Beckett LA, Albert MS, Pilgrim DM, Chown MJ, Funkenstein HH, Evans DA (1995) Age-specific incidence of alzheimer's disease in a community population. Jama 273(17):1354–1359

[34] Murphy MP, LeVine III H (2010) Alzheimer's disease and the amyloid-β peptide. Journal of Alzheimer's disease 19(1):311–323

[35] Selkoe DJ (2001) Alzheimer's disease: genes, proteins, and therapy. Physiological reviews

[36] Jarrett JT, Berger EP, Lansbury Jr PT (1993) The carboxy terminus of the. beta. amyloid protein is critical for the seeding of amyloid formation: Implications for the pathogenesis of alzheimer's disease. Biochemistry 32(18):4693–4697

[37] Friedemann M, Helk E, Tiiman A, Zovo K, Palumaa P, Tõugu V (2015) Effect of methionine-35 oxidation on the aggregation of amyloid-β peptide. Biochemistry and biophysics reports 3:94–99

[38] Johansson AS, Bergquist J, Volbracht C, Päiviö A, Leist M, Lannfelt L, Westlind-Danielsson A (2007) Attenuated amyloid-β aggregation and neurotoxicity owing to methionine oxidation. Neuroreport 18(6):559–563

[39] El-Agnaf OM, Mahil DS, Patel BP, Austen BM (2000) Oligomerization and toxicity of β-amyloid-42 implicated in alzheimer's disease. Biochemical and biophysical research communications 273(3):1003–1007

[40] Korsak M, Kozyreva T (2015) Beta amyloid hallmarks: from intrinsically disordered proteins to alzheimer's disease. Intrinsically Disordered Proteins Studied by NMR Spectroscopy pp 401–421

[41] Maity BK, Das AK, Dey S, Moorthi UK, Kaur A, Dey A, Surendran D, Pandit R, Kallianpur M, Chandra B, et al. (2019) Ordered and disordered segments of amyloid-β drive sequential steps of the toxic pathway. ACS Chemical Neuroscience 10(5):2498–2509

[42] Willbold D, Strodel B, Schröder GF, Hoyer W, Heise H (2021) Amyloid-type protein aggregation and prion-like properties of amyloids. Chemical Reviews 121(13):8285–8307, DOI 10.1021/acs.chemrev.1c00196

[43] Hamley IW (2012) The amyloid beta peptide: a chemist's perspective. role in alzheimer's and fibrillization. Chemical reviews 112(10):5147–5192

[44] Verma M, Vats A, Taneja V (2015) Toxic species in amyloid disorders: Oligomers or mature fibrils. Annals of Indian Academy of Neurology 18(2):138

[45] Milanesi L, Sheynis T, Xue WF, Orlova EV, Hellewell AL, Jelinek R, Hewitt EW, Radford SE, Saibil HR (2012) Direct three-dimensional visualization of membrane disruption by amyloid fibrils. Proceedings of the National Academy of Sciences 109(50):20455–20460

[46] Evangelisti E, Cascella R, Becatti M, Marrazza G, Dobson CM, Chiti F, Stefani M, Cecchi C (2016) Binding affinity of amyloid oligomers to cellular membranes is a generic indicator of cellular dysfunction in protein misfolding diseases. Scientific reports 6(1):1–14

[47] Mannini B, Mulvihill E, Sgromo C, Cascella R, Khodarahmi R, Ramazzotti M, Dobson CM, Cecchi C, Chiti F (2014) Toxicity of protein oligomers is rationalized by a function combining size and surface hydrophobicity. ACS chemical biology 9(10):2309–2317

[48] Vivoli Vega M, Cascella R, Chen SW, Fusco G, De Simone A, Dobson CM, Cecchi C, Chiti F (2019) The toxicity of misfolded protein oligomers is independent of their secondary structure. ACS Chemical Biology 14(7):1593–1600

[49] Serra-Batiste M, Ninot-Pedrosa M, Bayoumi M, Gairí M, Maglia G, Carulla N (2016) Aβ42 assembles into specific β-barrel pore-forming oligomers in membrane-mimicking environments. Proceedings of the National Academy of Sciences 113(39):10866–10871

[50] Prusiner SB (1982) Novel proteinaceous infectious particles cause scrapie. Science 216(4542):136–144

[51] Riesner D (2004) Transmissible spongiform encephalopathies: the prion theory-background and basic information. Contributions to microbiology 11:1–13

[52] Aguzzi A, Calella AM (2009) Prions: protein aggregation and infectious diseases. Physiological reviews 89(4):1105–1152

[53] Meyer-Luehmann M, Coomaraswamy J, Bolmont T, Kaeser S, Schaefer C, Kilger E, Neuenschwander A, Abramowski D, Frey P, Jaton AL, et al. (2006) Exogenous induction of cerebral ß-amyloidogenesis is governed by agent and host. Science 313(5794):1781–1784

[54] Stahl N, Borchelt DR, Hsiao K, Prusiner SB (1987) Scrapie prion protein contains a phosphatidylinositol glycolipid. Cell 51(2):229–240

[55] Zahn R, Liu A, Lührs T, Riek R, Schroetter Cv, García FL, Billeter M, Calzolai L, Wider G, Wüthrich K (2000) Nmr solution structure of the human prion protein. Proceedings of the National Academy of Sciences 97(1):145–150, DOI 10.1073/pnas.97.1.145

[56] Kim SJ, Rahbar R, Hegde RS (2001) Combinatorial control of prion protein biogenesis by the signal sequence and transmembrane domain. Journal of Biological Chemistry 276(28):26132–26140

[57] Altmeppen HC, Puig B, Dohler F, Thurm DK, Falker C, Krasemann S, Glatzel M (2012) Proteolytic processing of the prion protein in health and disease. American journal of neurodegenerative disease 1(1):15

[58] Wang LQ, Zhao K, Yuan HY, Wang Q, Guan Z, Tao J, Li XN, Sun Y, Yi CW, Chen J, Li D, Zhang D, Yin P, Liu C, Liang Y (2020) Cryo-em structure of an amyloid fibril formed by full-length human prion protein. Nature Structural & Molecular Biology 27(6):598–602, DOI 10.1038/s41594-020-0441-5

[59] Chen SG, Teplow DB, Parchi P, Teller JK, Gambetti P, Autilio-Gambetti L (1995) Truncated forms of the human prion protein in normal brain and in prion diseases. Journal of Biological Chemistry 270(32):19173–19180

[60] Vincent B, Paitel E, Saftig P, Frobert Y, Hartmann D, De Strooper B, Grassi J, Lopez-Perez E, Checler F (2001) The disintegrins adam10 and tace contribute to the constitutive and phorbol ester-regulated normal cleavage of the cellular prion protein. Journal of Biological Chemistry 276(41):37743–37746

[61] Béland M, Roucou X (2012) The prion protein unstructured n-terminal region is a broad-spectrum molecular sensor with diverse and contrasting potential functions. Journal of neurochemistry 120(6):853–868

[62] Laurén J, Gimbel DA, Nygaard HB, Gilbert JW, Strittmatter SM (2009) Cellular prion protein mediates impairment of synaptic plasticity by amyloid-β oligomers. Nature 457(7233):1128–1132

[63] Chen S, Yadav SP, Surewicz WK (2010) Interaction between human prion protein and amyloid-β (aβ) oligomers: role of n-terminal residues. Journal of Biological Chemistry 285(34):26377–26383

[64] Rösener NS, Gremer L, Reinartz E, König A, Brener O, Heise H, Hoyer W, Neudecker P, Willbold D (2018) A d-enantiomeric peptide interferes with heteroassociation of amyloid-β oligomers and prion protein. Journal of Biological Chemistry 293(41):15748–15764

[65] Mallucci G, Dickinson A, Linehan J, Klohn PC, Brandner S, Collinge J (2003) Depleting neuronal prp in prion infection prevents disease and reverses spongiosis. Science 302(5646):871–874

[66] Yadavalli R, Guttmann RP, Seward T, Centers AP, Williamson RA, Telling GC (2004) Calpain-dependent endoproteolytic cleavage of prpsc modulates scrapie prion propagation. Journal of Biological Chemistry 279(21):21948–21956

[67] McMahon HE, Mange A, Nishida N, Creminon C, Casanova D, Lehmann S (2001) Cleavage of the amino terminus of the prion protein by reactive oxygen species. Journal of Biological Chemistry 276(3):2286–2291

[68] Guillot-Sestier MV, Sunyach C, Druon C, Scarzello S, Checler F (2009) The α-secretase-derived n-terminal product of cellular prion, n1, displays neuroprotective function in vitro and in vivo. Journal of Biological Chemistry 284(51):35973–35986

[69] Sunyach C, Cisse MA, da Costa CA, Vincent B, Checler F (2007) The c-terminal products of cellular prion protein processing, c1 and c2, exert distinct influence on p53-dependent staurosporine-induced caspase-3 activation. Journal of Biological Chemistry 282(3):1956–1963

[70] Prusiner SB, McKinley MP, Bowman KA, Bolton DC, Bendheim PE, Groth DF, Glenner GG (1983) Scrapie prions aggregate to form amyloid-like birefringent rods. Cell 35(2):349–358

[71] Wadsworth JD, Joiner S, Linehan JM, Desbruslais M, Fox K, Cooper S, Cronier S, Asante EA, Mead S, Brandner S, et al. (2008) Kuru prions and sporadic creutzfeldt–jakob disease prions have equivalent transmission properties in transgenic and wild-type mice. Proceedings of the National Academy of Sciences 105(10):3885–3890

[72] Hosszu LL, Conners R, Sangar D, Batchelor M, Sawyer EB, Fisher S, Cliff MJ, Hounslow AM, McAuley K, Leo Brady R, et al. (2020) Structural effects of the highly protective v127 polymorphism on human prion protein. Communications biology 3(1):1–12

[73] Hosszu LL, Jackson GS, Trevitt CR, Jones S, Batchelor M, Bhelt D, Prodromidou K, Clarke AR, Waltho JP, Collinge J (2004) The residue 129 polymorphism in human prion protein does not confer susceptibility to creutzfeldt-jakob disease by altering the structure or global stability of prpc. Journal of Biological Chemistry 279(27):28515–28521

[74] Cobb NJ, Surewicz WK (2009) Prion diseases and their biochemical mechanisms. Biochemistry 48(12):2574–2585

[75] Brown P, Cathala F, Raubertas R, Gajdusek D, Castaigne P (1987) The epidemiology of creutzfeldt-jakob disease: conclusion of a 15-year investigation in france and review of the world literature. Neurology 37(6):895–895

[76] Malmgren R (1979) The epidemiology of creufzfeldt-jakob disase. Slow transmissible diseases of the nervous system 1:93–112

[77] Perrett S, Ma J, Wang F (2014) Prion disease and the ‘protein-only hypothesis’. Essays in biochemistry 56:181–191

[78] Jarrett JT, Lansbury Jr PT (1993) Seeding “one-dimensional crystallization” of amyloid: a pathogenic mechanism in alzheimer’s disease and scrapie? Cell 73(6):1055–1058

[79] Almeida ZL, Brito RMM (2020) Structure and aggregation mechanisms in amyloids. Molecules 25(5):1195, DOI 10.3390/molecules25051195

[80] Chothia C, Janin J (1975) Principles of protein–protein recognition. Nature 256(5520):705–708

[81] Linse S (2019) Mechanism of amyloid protein aggregation and the role of inhibitors. Pure and Applied Chemistry 91(2):211–229

[82] O’Nuallain B, Shivaprasad S, Kheterpal I, Wetzel R (2005) Thermodynamics of aβ (1- 40) amyloid fibril elongation. Biochemistry 44(38):12709–12718

[83] Arosio P, Knowles TPJ, Linse S (2015) On the lag phase in amyloid fibril formation. Physical Chemistry Chemical Physics 17(12):7606–7618, DOI 10.1039/c4cp05563b

[84] Cohen SI, Vendruscolo M, Dobson CM, Knowles TP (2012) From macroscopic measurements to microscopic mechanisms of protein aggregation. Journal of molecular biology 421(2-3):160–171

[85] Dear AJ, Meisl G, Šarić A, Michaels TC, Kjaergaard M, Linse S, Knowles TP (2020) Identification of on-and off-pathway oligomers in amyloid fibril formation. Chemical Science 11(24):6236–6247

[86] Winner B, Jappelli R, Maji SK, Desplats PA, Boyer L, Aigner S, Hetzer C, Loher T, Vilar M, Campioni S, et al. (2011) In vivo demonstration that α-synuclein oligomers are toxic. Proceedings of the National Academy of Sciences 108(10):4194–4199

[87] Sengupta U, Nilson AN, Kayed R (2016) The role of amyloid-β oligomers in toxicity, propagation, and immunotherapy. EBioMedicine 6:42–49

[88] Guerrero-Muñoz MJ, Castillo-Carranza DL, Krishnamurthy S, Paulucci-Holthauzen AA, Sengupta U, Lasagna-Reeves CA, Ahmad Y, Jackson GR, Kayed R (2014) Amyloid-β oligomers as a template for secondary amyloidosis in alzheimer's disease. Neurobiology of disease 71:14–23

[89] Cleary JP, Walsh DM, Hofmeister JJ, Shankar GM, Kuskowski MA, Selkoe DJ, Ashe KH (2005) Natural oligomers of the amyloid-β protein specifically disrupt cognitive function. Nature neuroscience 8(1):79–84

[90] Conway KA, Lee SJ, Rochet JC, Ding TT, Williamson RE, Lansbury Jr PT (2000) Acceleration of oligomerization, not fibrillization, is a shared property of both α-synuclein mutations linked to early-onset parkinson's disease: implications for pathogenesis and therapy. Proceedings of the National Academy of Sciences 97(2):571–576

[91] Lin CY, Gurlo T, Kayed R, Butler AE, Haataja L, Glabe CG, Butler PC (2007) Toxic human islet amyloid polypeptide (h-iapp) oligomers are intracellular, and vaccination to induce anti-toxic oligomer antibodies does not prevent h-iapp–induced β-cell apoptosis in h-iapp transgenic mice. Diabetes 56(5):1324–1332

[92] Ehrnhoefer DE, Bieschke J, Boeddrich A, Herbst M, Masino L, Lurz R, Engemann S, Pastore A, Wanker EE (2008) Egcg redirects amyloidogenic polypeptides into unstructured, off-pathway oligomers. Nature structural & molecular biology 15(6):558–566

[93] Baskakov IV, Legname G, Baldwin MA, Prusiner SB, Cohen FE (2002) Pathway complexity of prion protein assembly into amyloid. Journal of Biological Chemistry 277(24):21140–21148

[94] Bemporad F, Chiti F (2012) Protein misfolded oligomers: experimental approaches, mechanism of formation, and structure-toxicity relationships. Chemistry & biology 19(3):315–327

[95] Michaels TC, Šarić A, Curk S, Bernfur K, Arosio P, Meisl G, Dear AJ, Cohen SI, Dobson CM, Vendruscolo M, et al. (2020) Dynamics of oligomer populations formed during the aggregation of alzheimer's aβ42 peptide. Nature chemistry 12(5):445–451

[96] Sang JC, Lee JE, Dear AJ, De S, Meisl G, Thackray AM, Bujdoso R, Knowles TP, Klenerman D (2019) Direct observation of prion protein oligomer formation reveals an aggregation mechanism with multiple conformationally distinct species. Chemical science 10(17):4588–4597

[97] Vekilov PG (2010) The two-step mechanism of nucleation of crystals in solution. Nanoscale 2(11):2346–2357

[98] Šarić A, Chebaro YC, Knowles TP, Frenkel D (2014) Crucial role of nonspecific interactions in amyloid nucleation. Proceedings of the National Academy of Sciences 111(50):17869–17874

[99] Cohen SI, Linse S, Luheshi LM, Hellstrand E, White DA, Rajah L, Otzen DE, Vendruscolo M, Dobson CM, Knowles TP (2013) Proliferation of amyloid-β42 aggregates occurs through a secondary nucleation mechanism. Proceedings of the National Academy of Sciences 110(24):9758–9763

[100] Cohen SI, Vendruscolo M, Welland ME, Dobson CM, Terentjev EM, Knowles TP (2011) Nucleated polymerization with secondary pathways. i. time evolution of the principal moments. The Journal of chemical physics 135(6):08B615

[101] Bishop MF, Ferrone FA (1984) Kinetics of nucleation-controlled polymerization. a perturbation treatment for use with a secondary pathway. Biophysical Journal 46(5):631–644

[102] Eva Ž (2002) Amyloid-fibril formation: Proposed mechanisms and relevance to conformational disease. European Journal of Biochemistry 269(14):3362–3371

[103] Uversky VN, Fink AL (2004) Conformational constraints for amyloid fibrillation: the importance of being unfolded. Biochimica et Biophysica Acta (BBA)-Proteins and Proteomics 1698(2):131–153

[104] Englander SW, Kallenbach NR (1983) Hydrogen exchange and structural dynamics of proteins and nucleic acids. Quarterly reviews of biophysics 16(4):521–655

[105] Nielsen L, Frokjaer S, Brange J, Uversky VN, Fink AL (2001) Probing the mechanism of insulin fibril formation with insulin mutants. Biochemistry 40(28):8397–8409

[106] Zhang T, Loschwitz J, Strodel B, Nagel-Steger L, Willbold D (2019) Interference with amyloid-β nucleation by transient ligand interaction. Molecules 24(11):2129

[107] Auclair JR, Boggio KJ, Petsko GA, Ringe D, Agar JN (2010) Strategies for stabilizing superoxide dismutase (sod1), the protein destabilized in the most common form of familial amyotrophic lateral sclerosis. Proceedings of the National Academy of Sciences 107(50):21394–21399

[108] Ray SS, Nowak RJ, Brown Jr RH, Lansbury Jr PT (2005) Small-molecule-mediated stabilization of familial amyotrophic lateral sclerosis-linked superoxide dismutase mutants against unfolding and aggregation. Proceedings of the National Academy of Sciences 102(10):3639–3644

[109] Sacchettini JC, Kelly JW (2002) Therapeutic strategies for human amyloid diseases. Nature Reviews Drug Discovery 1(4):267–275

[110] Howie AJ, Brewer DB (2009) Optical properties of amyloid stained by congo red: history and mechanisms. Micron 40(3):285–301

[111] Frieg B, Gremer L, Heise H, Willbold D, Gohlke H (2020) Binding modes of thioflavin t and congo red to the fibril structure of amyloid-β (1–42). Chemical communications 56(55):7589–7592

[112] Stsiapura VI, Maskevich AA, Kuzmitsky VA, Turoverov KK, Kuznetsova IM (2007) Computational study of thioflavin t torsional relaxation in the excited state. The Journal of Physical Chemistry A 111(22):4829–4835

[113] Wu C, Wang Z, Lei H, Duan Y, Bowers MT, Shea JE (2008) The binding of thioflavin t and its neutral analog bta-1 to protofibrils of the alzheimer's disease aβ16–22 peptide probed by molecular dynamics simulations. Journal of molecular biology 384(3):718–729

[114] Biancalana M, Makabe K, Koide A, Koide S (2009) Molecular mechanism of thioflavin-t binding to the surface of β-rich peptide self-assemblies. Journal of molecular biology 385(4):1052–1063

[115] Xue C, Lin TY, Chang D, Guo Z (2017) Thioflavin t as an amyloid dye: fibril quantification, optimal concentration and effect on aggregation. Royal Society open science 4(1):160696

[116] Harel M, Sonoda LK, Silman I, Sussman JL, Rosenberry TL (2008) Crystal structure of thioflavin t bound to the peripheral site of torpedo californica acetylcholinesterase reveals how thioflavin t acts as a sensitive fluorescent reporter of ligand binding to the acylation site. Journal of the American Chemical Society 130(25):7856–7861

[117] Maezawa I, Hong HS, Liu R, Wu CY, Cheng RH, Kung MP, Kung HF, Lam KS, Oddo S, LaFerla FM, et al. (2008) Congo red and thioflavin-t analogs detect aβ oligomers. Journal of neurochemistry 104(2):457–468

[118] Aliyan A, Cook NP, Martí AA (2019) Interrogating amyloid aggregates using fluorescent probes. Chemical reviews 119(23):11819–11856

[119] Lindgren M, Sörgjerd K, Hammarström P (2005) Detection and characterization of aggregates, prefibrillar amyloidogenic oligomers, and protofibrils using fluorescence spectroscopy. Biophysical journal 88(6):4200–4212

[120] Wong AG, Raleigh DP (2016) The dye sypro orange binds to amylin amyloid fibrils but not pre-fibrillar intermediates. Protein Science 25(10):1834–1840

[121] Klingstedt T, Åslund A, Simon RA, Johansson LB, Mason JJ, Nyström S, Hammarström P, Nilsson KPR (2011) Synthesis of a library of oligothiophenes and their utilization as fluorescent ligands for spectral assignment of protein aggregates. Organic & biomolecular chemistry 9(24):8356–8370

[122] Zhang J, Sandberg A, Konsmo A, Wu X, Nyström S, Nilsson KPR, Konradsson P, LeVine III H, Lindgren M, Hammarström P (2018) Detection and imaging of aβ1-42 and tau fibrils by redesigned fluorescent x-34 analogues. Chemistry–A European Journal 24(28):7210–7216

[123] Lindberg DJ, Esbjörner EK (2016) Detection of amyloid-β fibrils using the dna-intercalating dye yoyo-1: Binding mode and fibril formation kinetics. Biochemical and biophysical research communications 469(2):313–318

[124] W Bertoncini C, Soledad Celej M (2011) Small molecule fluorescent probes for the detection of amyloid self-assembly in vitro and in vivo. Current Protein and Peptide Science 12(3):206–220

[125] Nagarajan S, Lapidus LJ (2017) Fluorescent probe dcvj shows high sensitivity for characterization of amyloid β-peptide early in the lag phase. ChemBioChem 18(22):2205–2211

[126] Oshinbolu S, Shah R, Finka G, Molloy M, Uden M, Bracewell DG (2018) Evaluation of fluorescent dyes to measure protein aggregation within mammalian cell culture supernatants. Journal of Chemical Technology & Biotechnology 93(3):909–917

[127] Breydo L, Kurouski D, Rasool S, Milton S, Wu JW, Uversky VN, Lednev IK, Glabe CG (2016) Structural differences between amyloid beta oligomers. Biochemical and biophysical research communications 477(4):700–705

[128] Nilsson KPR, Herland A, Hammarström P, Inganäs O (2005) Conjugated polyelectrolytes: conformation-sensitive optical probes for detection of amyloid fibril formation. Biochemistry 44(10):3718–3724

[129] Nilsson KPR, Hammarström P, Ahlgren F, Herland A, Schnell EA, Lindgren M, Westermark GT, Inganäs O (2006) Conjugated polyelectrolytes—conformation-sensitive optical probes for staining and characterization of amyloid deposits. ChemBioChem 7(7):1096–1104

[130] Nilsson KPR, Åslund A, Berg I, Nyström S, Konradsson P, Herland A, Inganäs O, Stabo-Eeg F, Lindgren M, Westermark GT, et al. (2007) Imaging distinct conformational states of amyloid-β fibrils in alzheimer's disease using novel luminescent probes. ACS chemical biology 2(8):553–560

[131] Åslund A, Sigurdson CJ, Klingstedt T, Grathwohl S, Bolmont T, Dickstein DL, Glimsdal E, Prokop S, Lindgren M, Konradsson P, et al. (2009) Novel pentameric thiophene derivatives for in vitro and in vivo optical imaging of a plethora of protein aggregates in cerebral amyloidoses. ACS chemical biology 4(8):673–684

[132] Civitelli L, Sandin L, Nelson E, Khattak SI, Brorsson AC, Kågedal K (2016) The luminescent oligothiophene p-ftaa converts toxic aβ1–42 species into nontoxic amyloid fibers with altered properties. Journal of Biological Chemistry 291(17):9233–9243

[133] König C, Skånberg R, Hotz I, Ynnerman A, Norman P, Linares M (2018) Binding sites for luminescent amyloid biomarkers from non-biased molecular dynamics simulations. Chemical Communications 54(24):3030–3033

[134] Klunk WE, Debnath ML, Pettegrew JW (1994) Development of small molecule probes for the beta-amyloid protein of alzheimer's disease. Neurobiology of aging 15(6):691–698

[135] Carlsson C, Larsson A, Jonsson M, Albinsson B, Norden B (1994) Optical and photophysical properties of the oxazole yellow dna probes yo and yoyo. The Journal of Physical Chemistry 98(40):10313–10321

[136] Schuck P (2016) Sedimentation velocity analytical ultracentrifugation: discrete species and size-distributions of macromolecules and particles. CRC Press

[137] Schuck P, Zhao H, Brautigam CA, Ghirlando R (2016) Basic principles of analytical ultracentrifugation, vol 2015. CRC Press Boca Raton

[138] MacGregor IK, Anderson AL, Laue TM (2004) Fluorescence detection for the xli analytical ultracentrifuge. Biophysical chemistry 108(1-3):165–185

[139] Edwards GB, Muthurajan UM, Bowerman S, Luger K (2020) Analytical ultracentrifugation (auc): An overview of the application of fluorescence and absorbance auc to the study of biological macromolecules. Current protocols in molecular biology 133(1):e131

[140] Ralston GB (1993) Introduction to analytical ultracentrifugation, vol 1. Beckman California:

[141] Svedberg T (1934) Molecular weight analysis in centrifugal fields. Science 79(2050):327–332

[142] Lamm O (1929) Die differentialgleichung der ultrazentrifugierung. Almqvist & Wiksell

[143] Schuck P (2000) Size-distribution analysis of macromolecules by sedimentation velocity ultracentrifugation and lamm equation modeling. Biophysical journal 78(3):1606–19, DOI 10.1016/S0006-3495(00)76713-0, URL `http://www.ncbi.nlm.nih.gov/pubmed/10692345`

[144] Kelly SM, Jess TJ, Price NC (2005) How to study proteins by circular dichroism. Biochimica et Biophysica Acta (BBA)-Proteins and Proteomics 1751(2):119–139

[145] Rodger A, Nordén B, et al. (1997) Circular dichroism and linear dichroism, vol 1. Oxford University Press, USA

[146] Fujiwara H (2007) Spectroscopic ellipsometry: principles and applications. John Wiley & Sons

[147] Greenfield NJ (2006) Using circular dichroism spectra to estimate protein secondary structure. Nature protocols 1(6):2876–2890

[148] Holzwarth G, Doty P (1965) The ultraviolet circular dichroism of polypeptides1. Journal of the American Chemical Society 87(2):218–228

[149] Greenfield NJ, Fasman GD (1969) Computed circular dichroism spectra for the evaluation of protein conformation. Biochemistry 8(10):4108–4116

[150] Venyaminov SY, Baikalov I, Shen ZM, Wu CSC, Yang J (1993) Circular dichroic analysis of denatured proteins: inclusion of denatured proteins in the reference set. Analytical biochemistry 214(1):17–24

[151] Cline EN, Bicca MA, Viola KL, Klein WL (2018) The amyloid-beta oligomer hypothesis: Beginning of the third decade. J Alzheimers Dis 64(s1):S567–S610, DOI 10.3233/JAD-179941, URL `https://www.ncbi.nlm.nih.gov/pubmed/29843241`

[152] van Groen T, Schemmert S, Brener O, Gremer L, Ziehm T, Tusche M, Nagel-Steger L, Kadish I, Schartmann E, Elfgen A, et al. (2017) The aβ oligomer eliminating d-enantiomeric peptide rd2 improves cognition without changing plaque pathology. Scientific reports 7(1):1–12

[153] Schemmert S, Schartmann E, Zafiu C, Kass B, Hartwig S, Lehr S, Bannach O, Langen KJ, Shah NJ, Kutzsche J, et al. (2019) Aβ oligomer elimination restores cognition in transgenic alzheimer's mice with full-blown pathology. Molecular neurobiology 56(3):2211–2223

[154] Sanders OD, Rajagopal L, Rajagopal JA (2022) The oxidatively damaged dna and amyloid-β oligomer hypothesis of alzheimer's disease. Free Radical Biology and Medicine 179:403–412

[155] Nagel-Steger L, Owen MC, Strodel B (2016) An account of amyloid oligomers: Facts and figures obtained from experiments and simulations. Chembiochem 17(8):657–676

[156] Wen J, Fang F, Guo SH, Zhang Y, Peng XL, Sun WM, Wei XR, He JS, Hung T (2018) Amyloid β-derived diffusible ligands (addls) induce abnormal autophagy associated with aβ aggregation degree. Journal of Molecular Neuroscience 64:162–174

[157] Barghorn S, Nimmrich V, Striebinger A, Krantz C, Keller P, Janson B, Bahr M, Schmidt M, Bitner RS, Harlan J, et al. (2005) Globular amyloid β-peptide1- 42 oligomer- a homogenous and stable neuropathological protein in alzheimer's disease. Journal of neurochemistry 95(3):834–847

[158] Benilova I, Karran E, De Strooper B (2012) The toxic abeta oligomer and alzheimer's disease: an emperor in need of clothes. Nat Neurosci 15(3):349–57, DOI 10.1038/nn.3028, URL `https://www.ncbi.nlm.nih.gov/pubmed/22286176`

[159] Gremer L, Scholzel D, Schenk C, Reinartz E, Labahn J, Ravelli RBG, Tusche M, Lopez-Iglesias C, Hoyer W, Heise H, Willbold D, Schroder GF (2017) Fibril structure of amyloid-beta(1-42) by cryo-electron microscopy. Science 358(6359):116–119, DOI 10.1126/science.aao2825, URL `https://www.ncbi.nlm.nih.gov/pubmed/28882996`

[160] Fitzpatrick AW, Saibil HR (2019) Cryo-em of amyloid fibrils and cellular aggregates. Curr Opin Struct Biol 58:34–42, DOI 10.1016/j.sbi.2019.05.003, URL `https://www.ncbi.nlm.nih.gov/pubmed/31200186`

[161] König AS, Rösener NS, Gremer L, Tusche M, Flender D, Reinartz E, Hoyer W, Neudecker P, Willbold D, Heise H (2021) Structural details of amyloid β oligomers in complex with human prion protein as revealed by solid-state mas nmr spectroscopy. Journal of Biological Chemistry 296

[162] Jana MK, Cappai R, Pham CL, Ciccotosto GD (2016) Membrane-bound tetramer and trimer aβ oligomeric species correlate with toxicity towards cultured neurons. Journal of neurochemistry 136(3):594–608

[163] Wolff M, Unuchek D, Zhang B, Gordeliy V, Willbold D, Nagel-Steger L (2015) Amyloid β oligomeric species present in the lag phase of amyloid formation. PloS one 10(5):e0127865

[164] Wolff M, Zhang-Haagen B, Decker C, Barz B, Schneider M, Biehl R, Radulescu A, Strodel B, Willbold D, Nagel-Steger L (2017) Abeta42 pentamers/hexamers are the smallest detectable oligomers in solution. Sci Rep 7(1):2493, DOI 10.1038/s41598-017-02370-3, URL `https://www.ncbi.nlm.nih.gov/pubmed/28559586`

[165] Dam J, Velikovsky CA, Mariuzza RA, Urbanke C, Schuck P (2005) Sedimentation velocity analysis of heterogeneous protein-protein interactions: Lamm equation modeling and sedimentation coefficient distributions c (s). Biophysical journal 89(1):619–634

[166] Kroe RR, Laue TM (2009) Nuts and bolts: applications of fluorescence-detected sedimentation. Analytical biochemistry 390(1):1–13

[167] Nagarajan S, Lapidus LJ (2017) Fluorescent probe dcvj shows high sensitivity for characterization of amyloid beta-peptide early in the lag phase. Chembiochem 18(22):2205–2211, DOI 10.1002/cbic.201700387, URL `https://www.ncbi.nlm.nih.gov/pubmed/28892583`

[168] Mok YF, Ryan TM, Yang S, Hatters DM, Howlett GJ, Griffin MD (2011) Sedimentation velocity analysis of amyloid oligomers and fibrils using fluorescence detection. Methods 54(1):67–75, DOI 10.1016/j.ymeth.2010.10.004, URL `https://www.ncbi.nlm.nih.gov/pubmed/21055469`

[169] Mora AK, Nath S (2020) Sypro orange–a new gold standard amyloid probe. Journal of Materials Chemistry B 8(35):7894–7898

[170] Wong AG, Raleigh DP (2016) The dye sypro orange binds to amylin amyloid fibrils but not pre-fibrillar intermediates. Protein Science 25(10):1834–1840

[171] Klingstedt T, Åslund A, Simon RA, Johansson LB, Mason JJ, Nyström S, Hammarström P, Nilsson KPR (2011) Synthesis of a library of oligothiophenes and their utilization as fluorescent ligands for spectral assignment of protein aggregates. Organic & biomolecular chemistry 9(24):8356–8370

[172] Lindberg DJ, Esbjorner EK (2016) Detection of amyloid-beta fibrils using the dna-intercalating dye yoyo-1: Binding mode and fibril formation kinetics. Biochem Biophys Res Commun 469(2):313–8, DOI 10.1016/j.bbrc.2015.11.051, URL `https://www.ncbi.nlm.nih.gov/pubmed/26612254`

[173] Biancalana M, Shohei K (2010) Molecular mechanism of thioflavin-t binding to amyloid fibrils. Biochimica et biophysica acta 1804(7):1405–12, DOI 10.1016/j.bbapap.2010.04.001, URL `https://www.ncbi.nlm.nih.gov/pmc/articles/PMC2880406/`

[174] Sabate R, Estelrich J (2005) Evidence of the existence of micelles in the fibrillogenesis of beta-amyloid peptide. The journal of physical chemistry B 109(21):11027–32, DOI 10.1021/jp050716m, URL `http://www.ncbi.nlm.nih.gov/pubmed/16852343`

[175] Hellstrand E, Boland B, Walsh DM, Linse S (2010) Amyloid β-protein aggregation produces highly reproducible kinetic data and occurs by a two-phase process. ACS chemical neuroscience 1(1):13–18

[176] Schuck P (2000) Size-distribution analysis of macromolecules by sedimentation velocity ultracentrifugation and lamm equation modeling. Biophysical journal 78(3):1606–19, DOI 10.1016/S0006-3495(00)76713-0, URL `http://www.ncbi.nlm.nih.gov/pubmed/10692345`

[177] Lamm O (1929) Die differentialgleichung der ultrazentrifugierung. Ark Mat Astr Fys 21B(2):1–4

[178] Hasecke F, Miti T, Perez C, Barton J, Schölzel D, Gremer L, Grüning CS, Matthews G, Meisl G, Knowles TP, Willbold D, Neudecker P, Heise H, Ullah G, Hoyer W, Muschol M (2018) Origin of metastable oligomers and their effects on amyloid fibril self-assembly. Chem Sci 9(27):5937–5948

[179] Nirmalraj PN, List J, Battacharya S, Howe G, Xu L, Thompson D, Mayer M (2020) Complete aggregation pathway of amyloid β (1-40) and (1-42) resolved on an atomically clean interface. Science advances 6(15):eaaz6014

[180] Klein W, Stine Jr W, Teplow D (2004) Small assemblies of unmodified amyloid β-protein are the proximate neurotoxin in alzheimer's disease. Neurobiology of aging 25(5):569–580

[181] Willbold D, Strodel B, Schröder GF, Hoyer W, Heise H (2021) Amyloid-type protein aggregation and prion-like properties of amyloids. Chemical Reviews 121(13):8285–8307, DOI 10.1021/acs.chemrev.1c00196, URL `https://doi.org/10.1021/acs.chemrev.1c00196`, pMID: 34137605, `https://doi.org/10.1021/acs.chemrev.1c00196`

[182] Wolff M, Unuchek D, Zhang B, Gordeliy V, Willbold D, Nagel-Steger L (2015) Amyloid beta oligomeric species present in the lag phase of amyloid formation. PLoS One 10(5):e0127865, DOI 10.1371/journal.pone.0127865, URL `https://www.ncbi.nlm.nih.gov/pubmed/26024352`

[183] Bitan G, Kirkitadze MD, Lomakin A, Vollers SS, Benedek GB, Teplow DB (2003) Amyloid β-protein (aβ) assembly: Aβ40 and aβ42 oligomerize through distinct pathways. Proceedings of the National Academy of Sciences 100(1):330–335

[184] Bernstein SL, Dupuis NF, Lazo ND, Wyttenbach T, Condron MM, Bitan G, Teplow DB, Shea JE, Ruotolo BT, Robinson CV, et al. (2009) Amyloid-β protein oligomerization and the impor-

tance of tetramers and dodecamers in the aetiology of alzheimer's disease. Nature chemistry 1(4):326–331

[185] Yong W, Lomakin A, Kirkitadze MD, Teplow DB, Chen SH, Benedek GB (2002) Structure determination of micelle-like intermediates in amyloid β-protein fibril assembly by using small angle neutron scattering. Proceedings of the National Academy of Sciences 99(1):150–154

[186] Streets AM, Quake SR (2010) Ostwald ripening of clusters during protein crystallization. Phys Rev Lett 104:178102, DOI 10.1103/PhysRevLett.104.178102, URL `https://link.aps.org/doi/10.1103/PhysRevLett.104.178102`

[187] Li Y, Lubchenko V, Vorontsova MA, Filobelo L, Vekilov PG (2012) Ostwald-like ripening of the anomalous mesoscopic clusters in protein solutions. The Journal of Physical Chemistry B 116(35):10657–10664, DOI 10.1021/jp303316s, URL `https://doi.org/10.1021/jp303316s`, pMID: 22889282, `https://doi.org/10.1021/jp303316s`

[188] Brener O, Dunkelmann T, Gremer L, Van Groen T, Mirecka EA, Kadish I, Willuweit A, Kutzsche J, Jürgens D, Rudolph S, et al. (2015) Qiad assay for quantitating a compound's efficacy in elimination of toxic aβ oligomers. Scientific reports 5(1):1–13

[189] Limegrover CS, LeVine III H, Izzo NJ, Yurko R, Mozzoni K, Rehak C, Sadlek K, Safferstein H, Catalano SM (2021) Alzheimer's protection effect of a673t mutation may be driven by lower aβ oligomer binding affinity. Journal of Neurochemistry 157(4):1316–1330

[190] Cohen SI, Linse S, Luheshi LM, Hellstrand E, White DA, Rajah L, Otzen DE, Vendruscolo M, Dobson CM, Knowles TP (2013) Proliferation of amyloid-β42 aggregates occurs through a secondary nucleation mechanism. Proceedings of the National Academy of Sciences 110(24):9758–9763

[191] LeVine III H (2004) Alzheimer's β-peptide oligomer formation at physiologic concentrations. Analytical Biochemistry 335(1):81–90

[192] Adalsteinsson D, Schultz P (2020) The DataGraph Manual. Visual Data Tools, 4th edn

[193] Prusiner SB, McKinley MP, Groth DF, Bowman KA, Mock NI, Cochran SP, Masiarz FR (1981) Scrapie agent contains a hydrophobic protein. Proceedings of the National Academy of Sciences 78(11):6675–6679

[194] Pan KM, Baldwin M, Nguyen J, Gasset M, Serban A, Groth D, Mehlhorn I, Huang Z, Fletterick RJ, Cohen FE (1993) Conversion of alpha-helices into beta-sheets features in the formation of the scrapie prion proteins. Proceedings of the National Academy of Sciences 90(23):10962–10966

[195] Safar J, Roller PP, Gajdusek DC, Gibbs Jr CJ (1993) Thermal stability and conformational transitions of scrapie amyloid (prion) protein correlate with infectivity. Protein Science 2(12):2206–2216

[196] Kraus A, Hoyt F, Schwartz CL, Hansen B, Artikis E, Hughson AG, Raymond GJ, Race B, Baron GS, Caughey B (2021) High-resolution structure and strain comparison of infectious mammalian prions. Molecular Cell 81(21):4540–4551

[197] Collinge J, Palmer MS, Dryden A (1991) Genetic predisposition to iatrogenic creutzfeldt-jakob disease. The Lancet 337(8755):1441–1442

[198] Palmer MS, Dryden AJ, Hughes JT, Collinge J (1991) Homozygous prion protein genotype predisposes to sporadic creutzfeldt–jakob disease. Nature 352(6333):340–342

[199] Baker H, Poulter M, Crow T, Frith C, Lofthouse R, Ridley R, Collinge J (1991) Aminoacid polymorphism in human prion protein and age at death in inherited prion disease. The Lancet 337(8752):1286, DOI https://doi.org/10.1016/0140-6736(91)92953-Y, URL `https://www.sciencedirect.com/science/article/pii/014067369192953Y`, originally published as Volume 1, Issue 8752

[200] Baiardi S, Rossi M, Mammana A, Appleby BS, Barria MA, Calì I, Gambetti P, Gelpi E, Giese A, Ghetti B, et al. (2021) Phenotypic diversity of genetic creutzfeldt–jakob disease: A histo-molecular-based classification. Acta neuropathologica 142(4):707–728

[201] Brown K, Mastrianni JA (2010) The prion diseases. Journal of geriatric psychiatry and neurology 23(4):277–298

[202] Barducci A, Chelli R, Procacci P, Schettino V, Gervasio FL, Parrinello M (2006) Metadynamics simulation of prion protein: β-structure stability and the early stages of misfolding. Journal of the American Chemical Society 128(8):2705–2710

[203] Hosszu LL, Wells MA, Jackson GS, Jones S, Batchelor M, Clarke AR, Craven CJ, Waltho JP, Collinge J (2005) Definable equilibrium states in the folding of human prion protein. Biochemistry 44(50):16649–16657

[204] Gerum C, Silvers R, Wirmer-Bartoschek J, Schwalbe H (2009) Unfolded-state structure and dynamics influence the fibril formation of human prion protein. Angewandte Chemie 121(50):9616–9620

[205] Ziaunys M, Sneideris T, Smirnovas V (2020) Formation of distinct prion protein amyloid fibrils under identical experimental conditions. Scientific reports 10(1):1–7

[206] Torrent J, Martin D, Noinville S, Yin Y, Doumic M, Moudjou M, Beringue V, Rezaei H (2019) Pressure reveals unique conformational features in prion protein fibril diversity. Scientific reports 9(1):1–11

[207] Hosszu LL, Trevitt CR, Jones S, Batchelor M, Scott DJ, Jackson GS, Collinge J, Waltho JP, Clarke AR (2009) Conformational properties of β-prp. Journal of Biological Chemistry 284(33):21981–21990

[208] Pfleger C, Rathi PC, Klein DL, Radestock S, Gohlke H (2013) Constraint network analysis (cna): a python software package for efficiently linking biomacromolecular structure, flexibility,(thermo-) stability, and function

[209] Rathi PC, Jaeger KE, Gohlke H (2015) Structural rigidity and protein thermostability in variants of lipase a from bacillus subtilis. PloS one 10(7):e0130289

[210] Hermans SM, Pfleger C, Nutschel C, Hanke CA, Gohlke H (2017) Rigidity theory for biomolecules: concepts, software, and applications. Wiley Interdisciplinary Reviews: Computational Molecular Science 7(4):e1311

[211] Valley CC, Cembran A, Perlmutter JD, Lewis AK, Labello NP, Gao J, Sachs JN (2012) The methionine-aromatic motif plays a unique role in stabilizing protein structure. Journal of Biological Chemistry 287(42):34979–34991

[212] Lee J, Chang I (2019) Structural insight into conformational change in prion protein by breakage of electrostatic network around h187 due to its protonation. Scientific reports 9(1):1–11

[213] Zhou S, Shi D, Liu X, Yao X, Da LT, Liu H (2019) ph-induced misfolding mechanism of prion protein: Insights from microsecond-accelerated molecular dynamics simulations. ACS chemical neuroscience 10(6):2718–2729

[214] Malevanets A, Chong PA, Hansen DF, Rizk P, Sun Y, Lin H, Muhandiram R, Chakrabartty A, Kay LE, Forman-Kay JD, et al. (2017) Interplay of buried histidine protonation and protein stability in prion misfolding. Scientific reports 7(1):1–14

[215] Baldwin AJ, Knowles TP, Tartaglia GG, Fitzpatrick AW, Devlin GL, Shammas SL, Waudby CA, Mossuto MF, Meehan S, Gras SL, et al. (2011) Metastability of native proteins and the phenomenon of amyloid formation. Journal of the American Chemical Society 133(36):14160–14163

[216] Tahiri-Alaoui A, Gill AC, Disterer P, James W (2004) Methionine 129 variant of human prion protein oligomerizes more rapidly than the valine 129 variant: implications for disease susceptibility to creutzfeldt-jakob disease. Journal of Biological Chemistry 279(30):31390–31397

[217] Eghiaian F, Daubenfeld T, Quenet Y, van Audenhaege M, Bouin AP, van der Rest G, Grosclaude J, Rezaei H (2007) Diversity in prion protein oligomerization pathways results from domain expansion as revealed by hydrogen/deuterium exchange and disulfide linkage. Proceedings of the National Academy of Sciences 104(18):7414–7419

[218] Engelke AD, Gonsberg A, Thapa S, Jung S, Ulbrich S, Seidel R, Basu S, Multhaup G, Baier M, Engelhard M, et al. (2018) Dimerization of the cellular prion protein inhibits propagation of scrapie prions. Journal of Biological Chemistry 293(21):8020–8031

[219] Schuck P, Perugini MA, Gonzales NR, Howlett GJ, Schubert D (2002) Size-distribution analysis of proteins by analytical ultracentrifugation: strategies and application to model systems. Biophysical journal 82(2):1096–1111

[220] Abskharon RN, Giachin G, Wohlkonig A, Soror SH, Pardon E, Legname G, Steyaert J (2014) Probing the n-terminal β-sheet conversion in the crystal structure of the human prion protein bound to a nanobody. Journal of the American Chemical Society 136(3):937–944

[221] Chemical Computing Group U (2021) Molecular operating environment (moe)

[222] Honda RP, Yamaguchi Ki, Kuwata K (2014) Acid-induced molten globule state of a prion protein. Journal of Biological Chemistry 289(44):30355–30363

[223] Izadi S, Anandakrishnan R, Onufriev AV (2014) Building water models: a different approach. The journal of physical chemistry letters 5(21):3863–3871

[224] Case DA, Cheatham III TE, Darden T, Gohlke H, Luo R, Merz Jr KM, Onufriev A, Simmerling C, Wang B, Woods RJ (2005) The amber biomolecular simulation programs. Journal of computational chemistry 26(16):1668–1688

[225] Tian C, Kasavajhala K, Belfon KA, Raguette L, Huang H, Migues AN, Bickel J, Wang Y, Pincay J, Wu Q, et al. (2019) ff19sb: Amino-acid-specific protein backbone parameters trained against quantum mechanics energy surfaces in solution. Journal of chemical theory and computation 16(1):528–552

[226] Roe DR, Cheatham III TE (2013) Ptraj and cpptraj: software for processing and analysis of molecular dynamics trajectory data. Journal of chemical theory and computation 9(7):3084–3095

[227] Jacobs DJ, Rader AJ, Kuhn LA, Thorpe MF (2001) Protein flexibility predictions using graph theory. Proteins: Structure, Function, and Bioinformatics 44(2):150–165

[228] Barlow DJ, Thornton J (1983) Ion-pairs in proteins. Journal of molecular biology 168(4):867–885

[229] Ryckaert JP, Ciccotti G, Berendsen HJ (1977) Numerical integration of the cartesian equations of motion of a system with constraints: molecular dynamics of n-alkanes. Journal of computational physics 23(3):327–341

[230] Hopkins CW, Le Grand S, Walker RC, Roitberg AE (2015) Long-time-step molecular dynamics through hydrogen mass repartitioning. Journal of chemical theory and computation 11(4):1864–1874

[231] Wolff M, Zhang-Haagen B, Decker C, Barz B, Schneider M, Biehl R, Radulescu A, Strodel B, Willbold D, Nagel-Steger L (2017) Aβ42 pentamers/hexamers are the smallest detectable oligomers in solution. Scientific reports 7(1):1–13

[232] Wolff M, Unuchek D, Zhang B, Gordeliy V, Willbold D, Nagel-Steger L (2015) Amyloid β oligomeric species present in the lag phase of amyloid formation. PloS one 10(5):e0127865

[233] Brener O, Dunkelmann T, Gremer L, Van Groen T, Mirecka EA, Kadish I, Willuweit A, Kutzsche J, Jürgens D, Rudolph S, et al. (2015) Qiad assay for quantitating a compound's efficacy in elimination of toxic aβ oligomers. Scientific reports 5(1):1–13

[234] Chen YR, Glabe CG (2006) Distinct early folding and aggregation properties of alzheimer amyloid-β peptides aβ40 and aβ42: stable trimer or tetramer formation by aβ42. Journal of Biological Chemistry 281(34):24414–24422

[235] Lambert MP, Barlow AK, Chromy BA, Edwards C, Freed R, Liosatos M, Morgan TE, Rozovsky I, Trommer B, Viola KL, Wals P, Zhang C, Finch CE, Krafft GA, Klein WL (1998) Diffusible, nonfibrillar ligands derived from abeta1-42 are potent central nervous system neurotoxins. Proceedings of the National Academy of Sciences of the United States of America 95(11):6448–53, URL `http://www.ncbi.nlm.nih.gov/pubmed/9600986`

[236] Bitan G, Fradinger EA, Spring SM, Teplow DB (2005) Neurotoxic protein oligomers—what you see is not always what you get. Amyloid 12(2):88–95

[237] Ostwald W (1896) Lehrbuch der allgemeinen chemie, vol. 2, part 1. engelmann, leipzig, germany

[238] Ostwald W (1897) Studien über die bildung und umwandlung fester körper. Zeitschrift für physikalische Chemie 22(1):289–330

[239] Aledo JC (2019) Methionine in proteins: The cinderella of the proteinogenic amino acids. Protein Science 28(10):1785–1796

[240] Jha SK, Marqusee S (2014) Kinetic evidence for a two-stage mechanism of protein denaturation by guanidinium chloride. Proceedings of the National Academy of Sciences 111(13):4856–4861

[241] Hill AF, Desbruslais M, Joiner S, Sidle KC, Gowland I, Collinge J, Doey LJ, Lantos P (1997) The same prion strain causes vcjd and bse. Nature 389(6650):448–450

[242] Hill A, Butterworth R, Joiner S, Jackson G, Rossor M, Thomas D, Frosh A, Tolley N, Bell J, Spencer M, et al. (1999) Investigation of variant creutzfeldt-jakob disease and other human prion diseases with tonsil biopsy samples. The Lancet 353(9148):183–189

[243] Collinge J, Beck J, Campbell T, Estibeiro K, Will RG (1996) Prion protein gene analysis in new variant cases of creutzfeldt-jakob disease. The Lancet 348(9019):56

[244] Goldfarb LG, Petersen RB, Tabaton M, Brown P, LeBlanc AC, Montagna P, Cortelli P, Julien J, Vital C, Pendelbury WW, et al. (1992) Fatal familial insomnia and familial creutzfeldt-jakob disease: disease phenotype determined by a dna polymorphism. Science 258(5083):806–808

[245] Schulz-Schaeffer W, Giese A, Windl O, Kretzschmar H (1996) Polymorphism at codon 129 of the prion protein gene determines cerebellar pathology in creutzfeldt-jakob disease. Clinical neuropathology 15(6):353–357

[246] Westergard L, Christensen HM, Harris DA (2007) The cellular prion protein (prpc): its physiological function and role in disease. Biochimica et Biophysica Acta (BBA)-Molecular Basis of Disease 1772(6):629–644

[247] König AS, Rösener NS, Gremer L, Tusche M, Flender D, Reinartz E, Hoyer W, Neudecker P, Willbold D, Heise H (2021) Structural details of amyloid β oligomers in complex with human prion protein as revealed by solid-state mas nmr spectroscopy. Journal of Biological Chemistry 296

[248] Asante EA, Smidak M, Grimshaw A, Houghton R, Tomlinson A, Jeelani A, Jakubcova T, Hamdan S, Richard-Londt A, Linehan JM, et al. (2015) A naturally occurring variant of the human prion protein completely prevents prion disease. Nature 522(7557):478–481